

The Research of Five-Bar Robot for Pressurized Autosampling for Enhanced Oil Recovery Research

by

© Shengqi Jian

A thesis submitted to the School of Graduate Studies for the partial
fulfillment of the requirements for the degree of Master of Engineering

SUPERVISORS:

Dr. Lesley James, Dr. Luc Rolland

Faculty of Engineering and Applied Science
Memorial University of Newfoundland

St. John's, Newfoundland, Canada
October 26th 2016

ABSTRACT

Robots have been widely used in industry and are becoming popular in people's daily lives. It makes production more efficient and everyday life more convenient. In this research, a robotic auto-sampler is designed, developed and tested to sample and collect two-phase fluids from a core flooding.

First of all, this thesis introduces the history of parallel robot industry the state of the art. Then, based on the problem statement, the most reasonable concept is chosen as the Five-Bar parallel robot. Theoretical simulations are made including kinematic analysis to calculate its mechanical dimension and dynamic analysis to calculate the actuator torque. As a result of that, the theoretical dimensions can be obtained and actuators can be chosen. In the design and control phase, the entire integrated system is presented in detail.

This thesis researches the design process of an auto-sampler based on a five-bar robot. From the proposed problem to the robot fabrication and programming, the entire system is designed, analyzed, built and tested.

ACKNOWLEDGEMENTS

I would like to express my sincere thanks to my supervisor Dr. Lesley James and my co-supervisor Dr. Luc Rolland for their guidance and continuous encouragement throughout my research.

I am also grateful to the Hibernia Management & Development Company (HMDC) for providing the financial support to this project.

I would like to thank Cheng Yin, Md Hassan Faghih and Shervin Ayazi who are always willing to help and give suggestions to my research. I was delighted to work with them in the Enhanced Oil Recovery Lab during my study.

I would like to thank Dr. Geoff Rideout, Dr. Leonard Lye, Dr. Michael Hinchey and Dr. George Mann for the instruction of four courses over the past two years.

I would also like to thank my parents and Tianqi Jin for their support and encouragement with their heart.

.

Table of Contents

1. Introduction.....	1
1.1. Introduction to Robotics.....	1
1.2. The History of Serial Robots.....	4
1.3. Serial Robots.....	5
1.3.1. Two DOFs Serial Robots	5
1.3.2. Three DOFs Serial Robots	6
1.3.3. Six DOFs Serial Robots	8
1.4. Advantages of Parallel Robots	9
1.5. The History of Parallel Robots	10
1.6. Parallel Robot Types and Applications	14
1.6.1. Two DOFs Parallel Robots.....	14
1.6.2. Three DOFs Parallel Robots	17
1.6.3. Six DOFs Parallel Robots	22
1.7. Auto-Samplers	25
1.7.1. Rotating Auto-Samplers.....	26
1.7.2. Planar Auto-Samplers	26
1.8. Research Objectives	27
1.9. Contribution from the Thesis.....	28
1.10. Organization of the Thesis	30
2. Overall Robot Design.....	32
2.1. Design Constraints	32
2.2. Conceptual Design	34
2.2.1. Methodology	34
2.2.2. Results.....	36
2.3. Peripheral Design.....	40
2.3.1. Methodology	41
2.3.2. Result	42
2.4. Risk Analysis for Auto-Sampler.....	44
2.4.1. Methodology	45

2.4.2. Results	46
2.5. Final Design and Discussion.....	47
3. Kinematics Analysis.....	48
3.1. Introduction	48
3.2. Literature Review	49
3.3. Kinematics Modelling Methodology	51
3.3.1. The Inverse Kinematics Model	51
3.3.2. The Forward Kinematics Model	55
3.3.3. Robot Working Modes	59
3.4. Differential Kinematics Modelling Methodology	60
3.4.1. The Forward Differential Kinematics Model.....	62
3.4.2. The Inverse Differential Kinematics Model	64
3.4.3. Singularities	66
3.5. Kinematics Optimization Methodology	71
3.5.1. Workspace Calculation Algorithm	71
3.5.2. Area Ratio Calculation Technique	73
3.6. Results	74
4. Dynamic Analysis.....	80
4.1. Introduction.....	80
4.2. Literature Review	81
4.3. Bond Graph Modeling.....	83
4.3.1. Bond Graph Modelling of the Actuators.....	87
4.3.2. Bond Graph Modelling of Robot Arms	89
4.3.3. Bond Graph Modelling of Parasitic Element.....	96
4.3.4. Bond Graph Modelling of the Complete Robot.....	97
4.3.5. Bond Graph Modelling of the Control System	99
4.4. Lagrangian Modeling	101
4.5. Bond Graph and Lagrangian Results Comparison	106
4.6. Bond Graph Simulation Results	109
5. Hardware Design	118
5.1. Mechanical Design	118

5.1.1. Linear Apparatus Design.....	119
5.1.2. End-Effector Design	121
5.1.3. Motors	123
5.1.4. Manipulator Design	124
5.1.5. Piercing Force Test.....	128
5.1.6. Safety Cage Design.....	133
5.2. Electronic Hardware and Circuits	134
5.2.1. DC Power Supply	135
5.2.2. Robot Controller Power Supply.....	136
5.2.3. Power Separation and Conversion Circuits	137
6. Control System	141
6.1. Control System Overview.....	141
6.2. Instrumentation.....	144
6.2.1. Robot Controller	144
6.2.2. DC Motor Driver.....	148
6.2.3. Proximity Sensor.....	151
6.2.4. Door Switch	152
6.2.5. Light Tower.....	153
6.2.6. Encoder	154
6.2.7. Solenoid Valve	156
6.3. Operating Process and Control Units	157
6.3.1. Operating Process	157
6.3.2. Labview Control GUI	160
6.4. Control Strategies	163
6.4.1. Servo Level Control Strategy.....	164
6.4.2. Task-Level Control.....	166
6.4.3. Path Planning:	167
7. Autosampler Commissioning Tests	169
7.1. Methodology	169
7.2. Operational Test.....	170
7.3. Negative Test.....	171
7.4. Fluid Test.....	172

8. Conclusion and Future Work	173
8.1. Conclusion	173
8.2. Future Work	175
9. BIBLIOGRAPHY	176
10. APPENDIX	182
10.1. Jacobian Matrix Solutions	182
10.2. Linear Actuator LM-P5H Specifications	194
10.3. Drawing of Linear Apparatus	195
10.4. Drawing of Linear Apparatus	196
10.5. Drawing of Proximal Arm	197
10.6. Drawing of Distal Arm One	198
10.7. Drawing of Distal Arm One	199
10.8. DMCC Schematic.....	200
10.9. Positive Test Script and Test Results	201
10.10. Negative Test Script and Test Results.....	203
10.11. Supplementary Test Script and Test Results	211

List of Figures

Figure 1-1	Degree of Freedom [35].....	2
Figure 1-2	Serial Manipulator	3
Figure 1-3	Parallel Manipulator.....	3
Figure 1-4	Programmable Article Transfer (Devol, 1961)	4
Figure 1-5	Epson EZ Modules 2-Axis Robot [18]	6
Figure 1-6	KUKA KR 10 SCARA R850 [20]	7
Figure 1-7	Parts Mounting by SCARA [21]	7
Figure 1-8	Unimate 500 PUMA [22].....	8
Figure 1-9	PUMA 500 [23].....	9
Figure 1-10	Parallel Amusement Device (from Gwinnett, 1931 [2]).....	11
Figure 1-11	Spray Painting Machine (Pollard, 1940 [3])	12
Figure 1-12	Position-controlling apparatus (Pollard, 1942 [4])	13
Figure 1-13	Assembly Robot [25]	15
Figure 1-14	MITSUBISHI RP-5ADH [12]	16
Figure 1-15	DexTAR Robot [12].....	16
Figure 1-16	5R PKM [15].....	17
Figure 1-17	Delta Robot [7]	18
Figure 1-18	IRB 360 FlexPicker (ABB Ltd.)	19
Figure 1-19	Tricept T605 (PKM Tricept S.L.)	20
Figure 1-20	The Agile Eye (3-DOF)	21
Figure 1-21	Motion Simulator [10]	22
Figure 1-22	C-17 Training Simulator	23
Figure 1-23	Full Mission Ship's Bridge Simulator.....	24
Figure 1-24	M-850 Medical Robot.....	24
Figure 1-25	Automatic analyzing apparatus [13]	25
Figure 1-26	Agilent 6850 Automatic Liquid Sampler.....	26
Figure 1-27	Lamda Omnicoll	27
Figure 2-1	Side View of Needle and Test Tube	33
Figure 2-2	Auto-Sampler within Process Flow Diagram	41
Figure 2-3	Comparison of Two Kinds of Tubes	42
Figure 2-4	Plastic Lid for Test Tube	43
Figure 2-5	Small Racks for Small Test Tubes	44
Figure 3-1	Sketch of Five-Bar Robot for Vector Method.....	52
Figure 3-2	Working Modes of Five-Bar Robot	59
Figure 3-3	Serial Singular Configurations.....	68

Figure 3-4	<i>B1P</i> or <i>B2P</i> Fully Folded	69
Figure 3-5	<i>B1P</i> or <i>B2P</i> Fully Extended	70
Figure 3-6	Workspace Algorithm	72
Figure 3-7	Workspace Optimization	75
Figure 3-8	Workspace of Minus-Minus Mode	76
Figure 3-9	Workspace of Plus-Plus Mode	77
Figure 3-10	Workspace of Plus-Minus Mode	78
Figure 3-11	Workspace of Minus-Plus Mode	78
Figure 3-12	Five-Bar Auto-Sampler Workspace	79
Figure 4-1	Bond Graph Causality [41]	85
Figure 4-2	Bond Graph Model of DC Motor [46]	88
Figure 4-3	Rigid Arm	90
Figure 4-4	Five-Bar Sketch	91
Figure 4-5	Bond Graph Model of Arm One <i>A1B1</i> and Arm Two <i>A2B2</i>	93
Figure 4-6	Bond Graph Model of Arm Three <i>B1C</i> and Arm Four <i>B2C</i>	95
Figure 4-7	Bond Graph Model of Isolator	96
Figure 4-8	Integrated Bond Graph of a Five-Bar Parallel Robot	98
Figure 4-9	PID Controller Process Diagram	99
Figure 4-10	Series PID Controller	101
Figure 4-11	Validation Trajectory	107
Figure 4-12	Trajectory Position Comparison	107
Figure 4-13	Angles and Angular Velocities Comparison	108
Figure 4-14	Torques Comparison	108
Figure 4-15	Angles and Positions Controlled Results	111
Figure 4-16	Motors Torque and Angular Velocity	113
Figure 4-17	Toques Applied on Arms	115
Figure 4-18	3D Animation Moving Process	116
Figure 5-1	SINOKOKO P5H-24-150 Linear Actuator	120
Figure 5-2	Linear Apparatus	121
Figure 5-3	End-Effector Design	123
Figure 5-4	Parallel Machine Design	125
Figure 5-5	Static Analysis of Arm	128
Figure 5-6	Static Analysis of Shaft	128
Figure 5-7	Instron 5585H	129
Figure 5-8	Injection and Extraction Experiment	130
Figure 5-9	Relocate Experiment Object	131
Figure 5-10	Injection and Extraction of Needles into Test Tube	132
Figure 5-11	Experiment Result	133

Figure 5-12	Safety Cage	134
Figure 5-13	SWS300A-24 Power Supply.....	136
Figure 5-14	Adafruit Switching AC/DC Power Adapter	137
Figure 5-15	Power Separation Circuit	138
Figure 5-16	Voltage Conversion Circuit.....	139
Figure 5-17	Power Extension Board.....	139
Figure 5-18	Circuit Schematic.....	140
Figure 6-1	Lab Control Center	141
Figure 6-2	Control System Structure.....	143
Figure 6-3	BeagleBone Black Structure Block Diagram [59].....	148
Figure 6-4	Dual Motor Control CAPE	150
Figure 6-5	Autonics PR12-2DN	152
Figure 6-6	Hinge Lever DPDT Limit Switch	152
Figure 6-7	Light Tower.....	154
Figure 6-8	HEDM 5500 Output Waveform [54]	155
Figure 6-9	Parker 2-Way Normally Open Solenoid Valve	156
Figure 6-10	Operating Process Diagram	159
Figure 6-11	Labview Control GUI	160
Figure 6-12	Labview Control GUI Logic Diagram.....	161
Figure 6-13	FTDI TTL-232R-3V3 Serial Cable [60].....	162
Figure 6-14	Five-Bar Auto-Sampler System	162
Figure 6-16	Multi-Level Control Structure	163
Figure 6-17	Trajectory Plan for All Test Tubes	168
Figure 7-1	Sketch of Piercing Holes on Septum	170

List of Tables

Table 2-1	Research Value Comparison	37
Table 2-2	Actuator Comparison	38
Table 2-3	Payload Comparison	39
Table 2-4	Cost Comparison.....	39
Table 2-5	Concept Selection Results.....	40
Table 2-6	Dimensions of Different Test Tubes	42
Table 2-7	FMEA Sheet for Auto-Sampler.....	46
Table 4-1	Effort and Flow in Different Energy Domain [41]	84
Table 4-2	Basic Components in Bond Graph.....	85
Table 4-3	DC Motor Parameters	88
Table 4-4	Principle Moment of Inertia for Each Arm	110
Table 4-5	Angles and Positions Controlled Results	112
Table 4-6	Motors Maximum Net Torque and Angular Velocity	114
Table 4-7	Maximum Net Torques Applied on Arms	116
Table 5-1	6802 Double Sealed by NSK Ball Bearing Specifications	127
Table 6-1	Robot Controllers Comparison	146
Table 6-2	PID ZN Parameters (Same on Two Controllers).....	165

Chapter 1

1. Introduction

1.1. Introduction to Robotics

A robot is a comprehensive system. It is integrated with electrical and mechanical machines controlled by a computer. It should be automated and programmable based on different requirements. They are artificial agents used to replace human resources doing practical tasks. Robotics is a new interdisciplinary branch of Mechanical Engineering, Electrical Engineering and Computer Science. Based on the definition from International Organization for Standardization 8373:2012 (ISO 8373:2012) [1], a robot is an "actuated mechanism programmable in two or more axes with a degree of autonomy, moving within its environment, to perform intended tasks." (Autonomy: ability to perform intended tasks based on current state and sensing, without human intervention.)

A rigid body in space can move in various ways, in translation or rotary motion, as shown in Figure 1-1. The rigid body can do translation in T_1 , T_2 and T_3 directions along ox , oy , and oz . It respectively can also rotate as R_1 , R_2 and R_3 about ox , oy and oz . These motions are called its degrees of freedom (DOF). There are a maximum of six degrees of freedom.

In robotics, the degree of freedom is the independent capability of every robot component to move related to the fixed base coordinate, excluding capability of any end-effector. The end-effector is the end of the manipulator to interact with the environment and it is connected to one arm. Generally, in order to let the end-effector reach any point and orientation in the space, the robot needs six degrees of freedom (DOFs). The DOFs is decided by the structure of the robot.

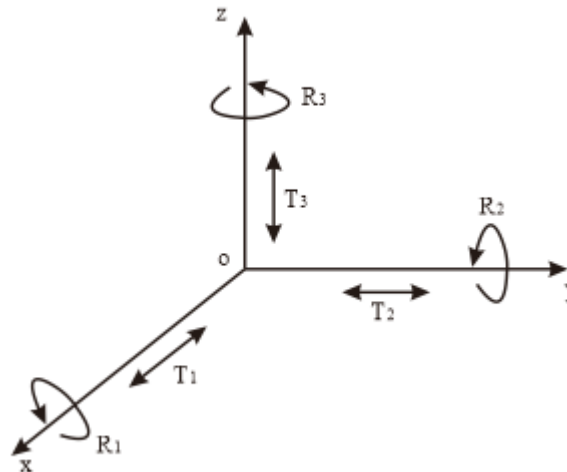


Figure 1-1 Degree of Freedom [35]

A serial manipulator consists of a succession of rigid bodies, each of them being linked to its predecessor and its successor by a one DOF joint. It can be a translation joint or a rotary joint. The end-effector, which is the end of the manipulator to interact with the environment, is connected to one arm. This mechanism is classical because it is similar to

the human arm and the idea of how the object is handled by the human arm is easy to transform into reality. Early robot designs mainly focused on serial manipulator research.

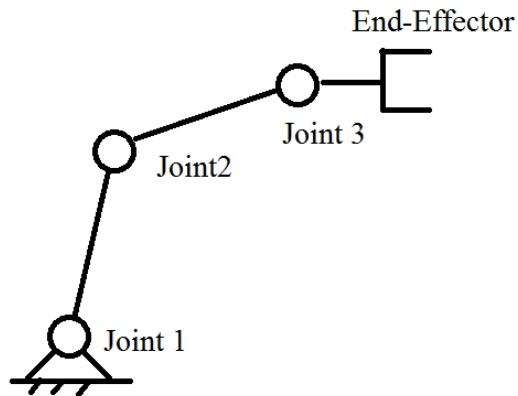


Figure 1-2 Serial Manipulator

Parallel manipulators, as shown in Figure 1-3, consist of multiple serial manipulators. End-effectors of all serial branches are connected at the coincident point or platform. Parallel manipulators use multiple arms to handle the object.

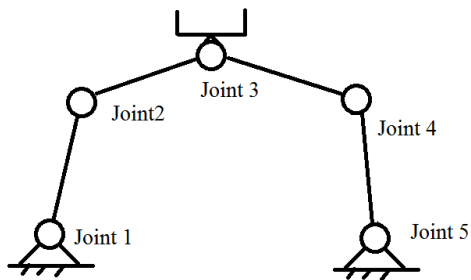


Figure 1-3 Parallel Manipulator

1.2. The History of Serial Robots

The serial robot is the most classical robot and it is the earliest robot applied in manufacturing industry, logistics industry, ocean engineering and space exploration engineering.

In 1954, the American inventor Devol invented the first electrical programmable industrial robot, shown in Figure 1-4, with the robot patent published in 1961. In 1962, American Unimation Company developed the first robot and it was used in a General Motors factory. It was used to lift hot pieces of metal from a die casting machine and stack them. In order to raise the manufacturing efficiency of the assembly line, Chrysler, Ford and Fiat purchased the first generation Unimation robots and installed them in their factories as well.

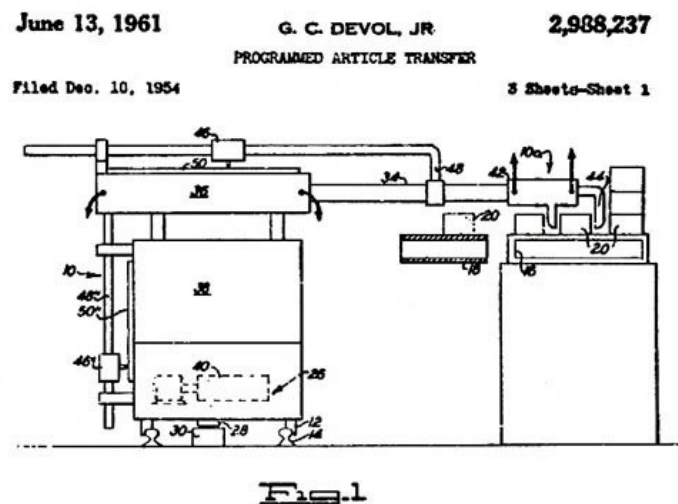


Figure 1-4 Programmable Article Transfer (Devol, 1961)

1.3. Serial Robots

Along with the development of Computer Science, more advanced serial robots were developed and applied in industrial production. In this section, three types of widely applied serial robots are introduced based on increasing DOFs.

1.3.1. Two DOFs Serial Robots

The Cartesian Coordinate Robots are industrial robots whose two principal axes of control are linear. The two sliding joints are controlled to move back and forth. The axes are coincident with the Cartesian reference frame, where the x and y axes are orthogonal to each other. The three prismatic joints move to deliver a linear motion along the axes [16]. Therefore, Cartesian Coordinate Robot has three translation degrees of freedom.

Chesley and Jelatis introduced the Cartesian device concept in 1967 [17]. It has two tracks along Cartesian coordinates. The original design is driven by rotary motors, wheels, and belts, power screws, or rack and pinion operated by a rotary motor. But most of the time, they require guiding rails or tracks. Now it is usually driven by linear actuators along the heavy tracks. As an example, Epson EZ Modules 2-Axis robot is shown in Figure 1-5.



Figure 1-5 Epson EZ Modules 2-Axis Robot [18]

The Cartesian Coordinate Robot is usually applied as a printing machine. The simplest application is used in drawing machines where a pen is installed as the end-effector. Plotting works can be finished within its workspace.

1.3.2. Three DOFs Serial Robots

Selective Compliant Assembly Robot Arm (SCARA) robots have two revolute joints that are parallel, allowing the robot to move in a horizontal plane [19]. It is a two-axis serial robot and it is widely produced by robot producers. It is a classical and traditional robot solution for the electronics assembling industry or food packing factories.

The SCARA robot was inspired by Hamada industrial robot design [24]. A SCARA robot made by KUKA is shown in Figure 1-6.



Figure 1-6 KUKA KR 10 SCARA R850 [20]

SCARA robot has three DOFs and it is widely used in low-intensity industry requiring picking and placing tasks, such as electronics manufacturing, and medication packaging. Shown in Figure 1-7, SCARA is installed on the robot frame along the assembly line. It picks a single part from the parts feeder then places the part to the point with certain orientation on the product surface.

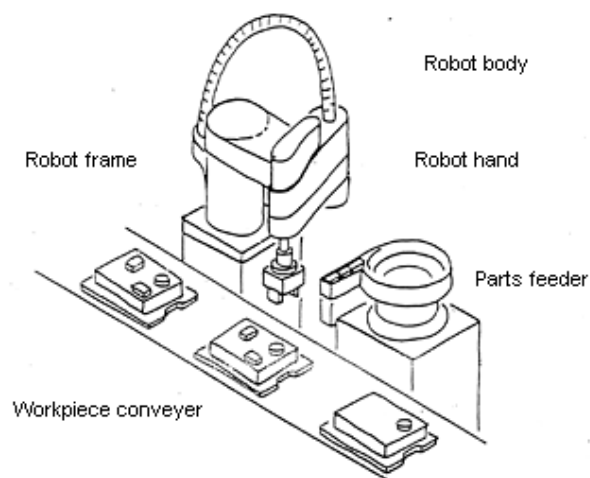


Figure 1-7 Parts Mounting by SCARA [21]

1.3.3. Six DOFs Serial Robots

Programmable Universal Machine for Assembly (PUMA) is a typical serial robot with six DOFs. After the development of the first serial robot, Unimation Company produced PUMA in 1978, shown in Figure 1-8. It is the first six-axis universal industrial robot. Until today, PUMA robot is still working on the assembly line in factories around the world.



Figure 1-8 Unimate 500 PUMA [22]

As shown in Figure 1-9, PUMA robot is composed of six revolute joints and two rigid arms. Compared to the three DOFs SCARA, PUMA has six DOFs. This attribute makes PUMA popular because three extra revolution DOFs allow PUMA to finish a variety of complicated tasks.

Each member of the robot arm is connected to another member at a joint. Through each joint passes one or more axes around, which the members of the arm rotate. PUMA robots are applied in parts assembling, auto body painting, welding and machining tools.

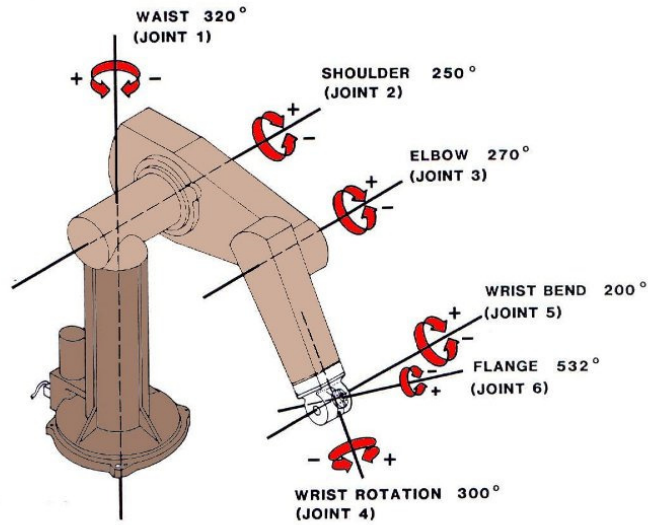


Figure 1-9 PUMA 500 [23]

1.4. Advantages of Parallel Robots

Based on the mechanical structure of the serial robot, only one chain of successive arms is connected to the ground base and the end-effector. Each arm on this chain has to support the total weight of all arms following itself and the weight of the load at the end-effector. Therefore, they are both applied on the arm and cause a large flexure torque. The flexure deformation is not detected by the robot's internal sensor [39].

The motion of the previous arm will be passed to the following arm, as well as the error,

because of the mechanical structure of the serial robot. If a small measurement error happens in the first or second arm, the error can be amplified until the last arm causing positioning error of the end-effector. Therefore, serial robots are not suitable for tasks requiring handling of heavy load and good positioning accuracy.

However, the problems existing in serial robot design can be solved by parallel robots, due to their different mechanical structure compared to the serial robots.

The end-effector of parallel robots is installed at the coincident point or plane of several chains of successive arms linked to the ground base. Each chain will only support the fractional weight of the load and each arm will support even less. Compared to the same size of the serial robot, this characteristic gives parallel robots a natural advantage of doing tasks like handling heavy loads and accurately positioning object

1.5. The History of Parallel Robots

The parallel mechanism can be defined as a kinematic closed loop mechanism, which contains one fixed platform and one floating platform connected by at least two independent kinematic chains. The mechanism covers at least two degrees of freedom (DOFs) and is actuated in parallel. The parallel mechanism was first introduced by Gwinnett in 1931 [2]. In his patent, he raised a cinema amusement device, which is a spherical parallel mechanism shown in Figure 1-10.

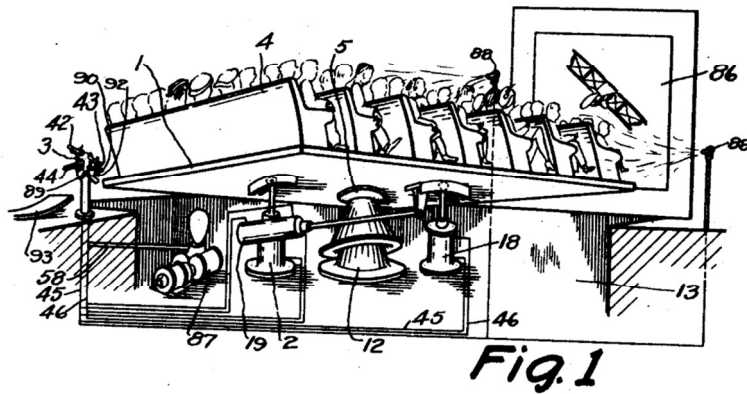


Figure 1-10 Parallel Amusement Device (from Gwinnett, 1931 [2])

In 1940, Pollard proposed a patent for a spray painting machine [3]. His design, shown in Figure 1-11, contains not only the mechanical manipulator but also an electrical position-controlling device. This system is actuated by multiple motors and points the spray gun to the car surface. This Five-Bar parallel manipulator became the first parallel mechanism in the world with an integrated control system. Parallel manipulators including Five-Bar parallel mechanism started attracting attention from academic researchers and industrial companies.

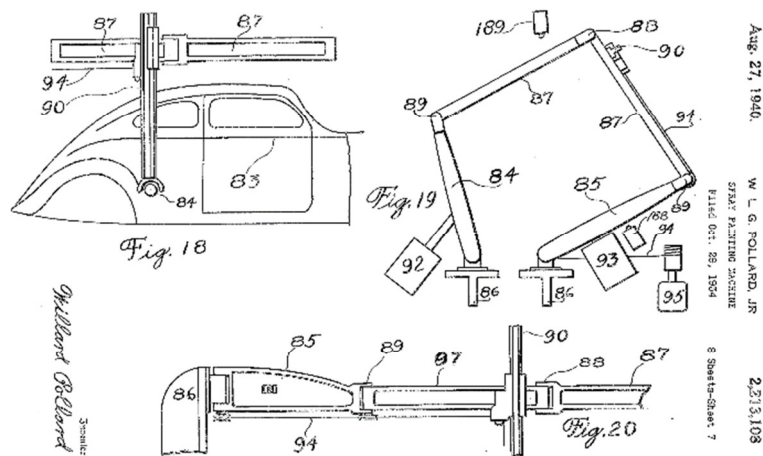


Figure 1-11 Spray Painting Machine (Pollard, 1940 [3])

After this design, Pollard upgraded his spray machine to a more complex mechanism [4], a parallel mechanism with three branches shown in Figure 1-12. The mechanism has three proximal arms and three distal arms. Three distal arms are connected to the ground via three revolute joints, which are actuated by three rotary actuators. Three distal arms are connected to three proximal arms with three ball joints. Two distal arms are connected to the third distal arm via two regular ball joints. The end-effector is connected to the third distal arm by a regular ball joint. The end-effector orientation is controlled by two screw-threaded shafts actuated by two rotary motors with two sets of ball joints. This is also an integrated system with mechanical manipulator and electrical system. Therefore, this was a five DOFs parallel robot. This position-control apparatus was designed to be installed in an automobile factory to do car painting tasks. It can be a very robust solution for surface tracking.

June 16, 1942.

W. L. V. POLLARD

2,286,571

POSITION CONTROLLING APPARATUS

Original Filed April 22, 1938 4 Sheets-Sheet 2

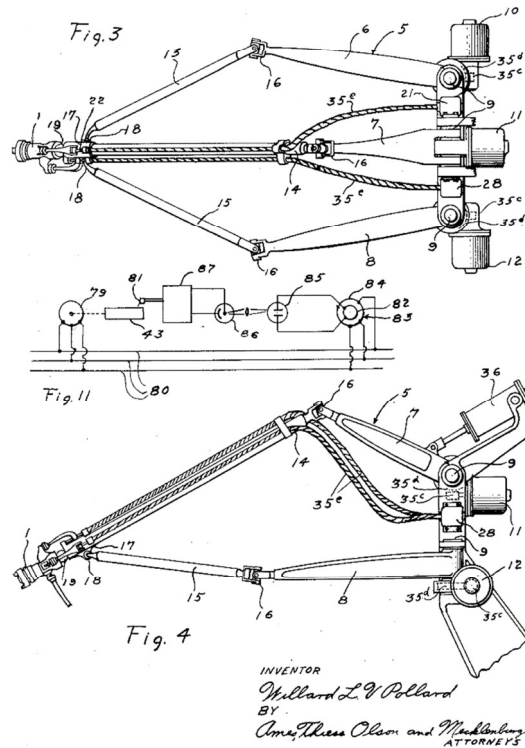


Figure 1-12 Position-controlling apparatus (Pollard, 1942 [4])

The universal tire testing machine was designed and built by Gough, an automobile engineer in Dunlop Rubber Co. in 1954 [5]. This machine was invented to test tires under aero-landing circumstances. By using this universal rig, different road situations, and touching angles could be determined. Since Gough requires a larger range of motions, he chose the symmetrical form as an octahedron. It was built in 1954 and this machine retired on 2001. In 1965, Stewart published the conceptual design of using hexapod as a new generation flight simulator [6]. There is no doubt that Stewart's thesis had great influence

on the application of the hexapod in motion simulators and industrial fields. This is the reason why this parallel mechanism is widely used and has been called the “Gough-Stewart” platform.

1.6. Parallel Robot Types and Applications

Parallel robots will be classified and presented by increasing number of DOF of the manipulator. Related classical design and application of parallel robot will be introduced in the following sections.

1.6.1. Two DOFs Parallel Robots

Most tasks can be accomplished by a low degree of freedom robot. Low degree of freedom robots, especially two degrees of freedom robot, are popular. Its simple structure, controllability, and low cost are also reasons why it is popular among academic researchers and industrial engineers

Five-Bar robots are driven by two rotary actuators. Its workspace also covers Cartesian coordinates, which is suitable for this task. An end-effector can be installed on the arm intersection. The robot was firstly patented by Hiroshi Makino as Assembly Robot [25].

The original design that he came up with is shown in Figure 1-13.

FIG.4

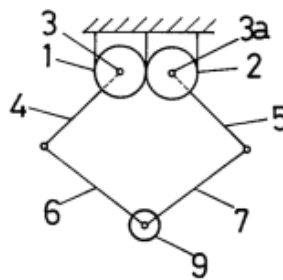


Figure 1-13 Assembly Robot [25]

A Five-Bar planar manipulator is a relatively simple structure, with characteristics of high speed, high accuracy, low inertia and high stiffness with two DOFs. For these reasons, it draws a lot of attention from the academic community. Some prototypes and commercial products have been made, such as the Double SCARA, RP-AH series offered by Mitsubishi Electric. The DexTAR, a Five-Bar planar manipulator designed by professor Bonev [12]. As the price is reduced, it has the potential to be widely used in production lines for picking and placing tasks and elements assembly tasks.

The double-SCARA robot is shown in Figure 1-14. Its highest precision can reach plus or minus 0.005 mm and the payload can reach 5 kg. The maximum speed can be 0.5 s/cycle. It can be applied to tasks demanding high speed and high accuracy.



Figure 1-14 MITSUBISHI RP-5ADH [12]

In Figure 1-15, the fastest Five-Bar robot DexTAR is shown. It is driven by two Kollmorgen GOLDLINE rotary motors. All arms lengths are equalized to 230 mm and offset distance of two motors is 275 mm. Based on simulations, the peak torque for motor requires 51 N.m and continuous torque request 17 N.m [12].

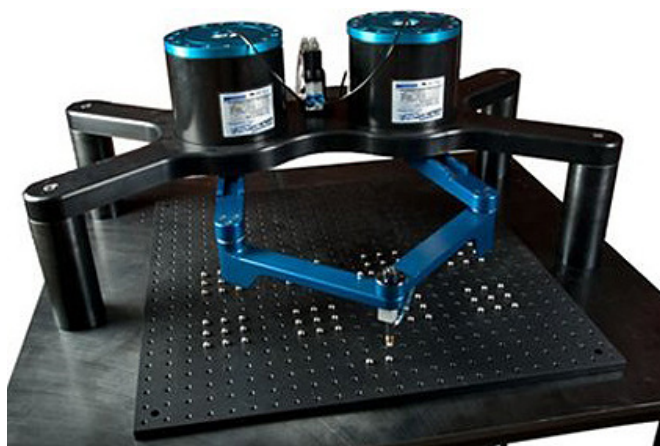


Figure 1-15 DexTAR Robot [12]

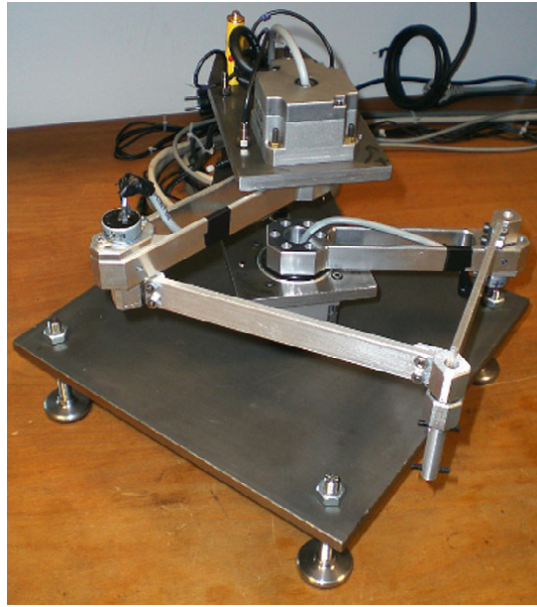


Figure 1-16 5R PKM [15]

In Figure 1-16, the 5R PKM, designed by Politecnico di Milano, is shown [15]. It is also driven by two gear motors with four links, however, in this design, two motors are installed coincidentally.

1.6.2. Three DOFs Parallel Robots

The Delta robot is another successful case in both scientific research and industrial application. In 1990, Clavel from École Polytechnique Fédérale de Lausanne, introduced the Delta robot [7], shown in Figure 1-17. It contains three legs actuated by three rotation actuators. Each leg has two separate bars connected with revolute joints or universal joints. The platform is connected to legs via revolute joints. These three legs give Delta robot three translations degrees of freedom. The fourth leg is actuated by a rotary motor and connected

to the platform via a universal joint. It provides the Delta robot a rotation degree of freedom.

U.S. Patent Dec. 11, 1990 Sheet 1 of 4 4,976,582

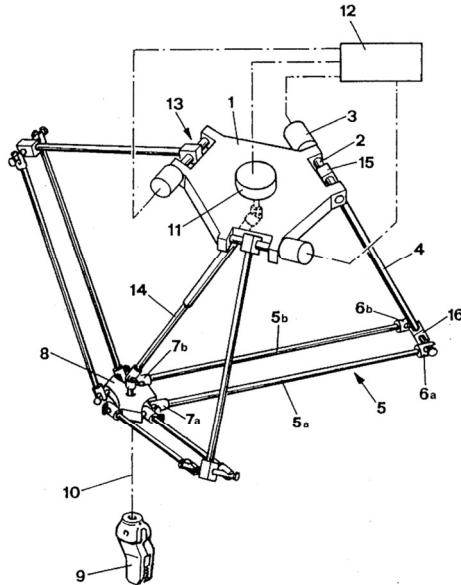


Figure 1-17 Delta Robot [7]

The payload and workspace of the Delta robot are small. However, the Delta robot has unmatched dynamic performance. In a lab environment, Delta robot's maximum acceleration can reach 50 g. Its light weight and fast speed make it become a competitive candidate for picking and placing tasks on factory assembly lines.



Figure 1-18 IRB 360 FlexPicker (ABB Ltd.)

In Figure 1-18, the FlexPicker is shown. It is a mature Delta robot product, which was launched in 1999. Its end-effector can be extended to a cable connected vacuum system for rapid picking and releasing. It has been widely applied in the food industry and electronics industry.



Figure 1-19 Tricept T605 (PKM Tricept S.L.)

Parallel robots are also widely used in industry. A prominent industrial application is the parallel machine tool. Traditional machines are usually serial kinematic mechanisms, such as computer numerical control (CNC) machines. In order to overcome the serial mechanism's error accumulating problem, high standard serial CNC machines usually have very big arms with large mass and complicated design for each moving axis. It causes maintenance issues to CNC machines. While serial kinematic machine tool trades dexterity for high accuracy, parallel machine combines high rigidity and accuracy with a good

dynamic response. For traditional machine tools, they have real tracks as reference axes. For a parallel kinematic machine, its end-effector motion is referred to virtual axes. The parallel mechanism permits a height load on end-effector, which is supported by multiple parallel legs and distributed in a more reasonable way. A parallel machine tool can machine complex 3D surfaces with relatively simple structure and high rigidity. In Figure 1-19, it's a parallel machine tool designed by PKM Tricept SL (former NEOS ROBOTICS AB).

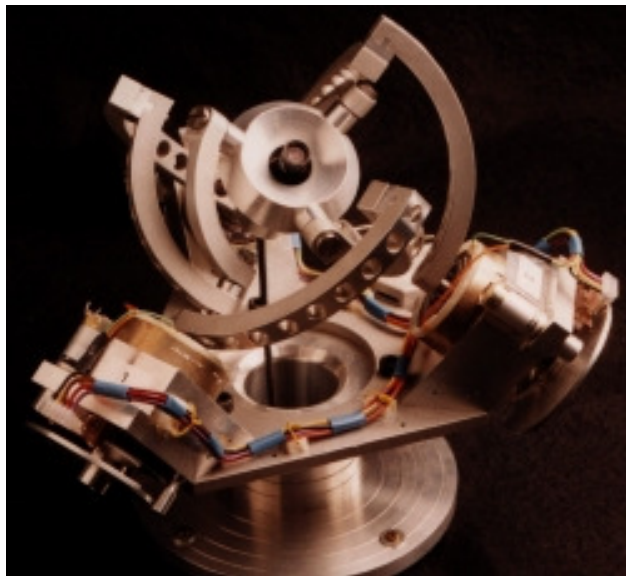


Figure 1-20 The Agile Eye (3-DOF)

Agile Eye was developed by Gosselin [9]. Its original design was a three-degree-of-freedom robot applied as a camera orienting device. It has a compact mechanism structure. All rotary axes are coincident at one point. While this kind of robot does not have a large workspace, they are suitable for tasks needing fast orientation

changes. The mini camera is installed on the end-effector and it can be pointed within a cone of 140° opening with plus or minus 30° in torsion [9]. It can reach $1000^\circ/s$ maximum angular velocity and $20000^\circ/s$ maximum angular acceleration, as shown in Figure 1-20.

1.6.3. Six DOFs Parallel Robots

As mentioned in the previous section, The Hexapods is a typical parallel robot with six DOFs shown in Figure 1-21. Six DOFs parallel robots are widely used as aircraft simulators or water vehicle simulators. Many companies started building parallel robots and sold them around the world to train pilots on the ground.

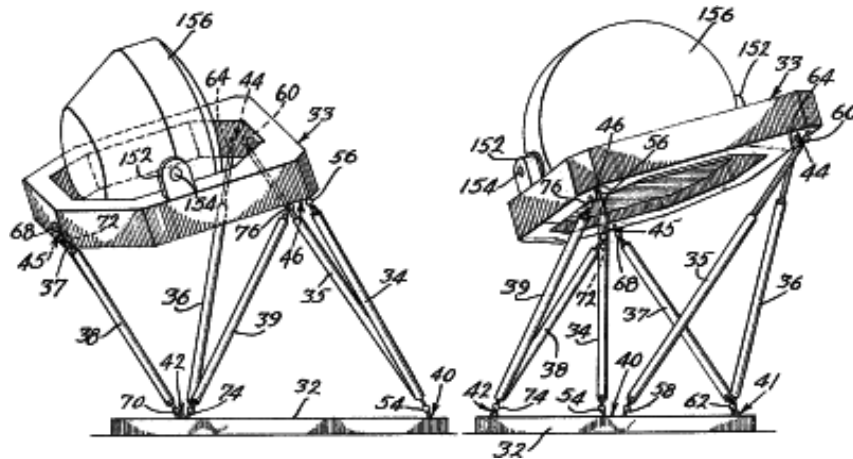


Figure 1-21 Motion Simulator [10]

This technology has increased efficiency and made it safer to train. A C-17 simulation center based on the Stewart mechanism has been designed by Boeing and was delivered to

US air force in 2013, shown in Figure 1-22.



Figure 1-22 C-17 Training Simulator

In Newfoundland and Labrador, offshore platforms are built and offshore workers' safety is a big issue. Fully trained safety boat drivers and life rescuers are in high demand. A set of ship bridge simulators was introduced to the Marine Institute in 1994 and upgraded in 2006, as shown in Figure 1-23. This simulator was also designed based on the six DOFs Stewart parallel robot. It can simulate a boat driven in difficult weather and sea conditions to aid in preparing sea captains for sea.



Figure 1-23 Full Mission Ship's Bridge Simulator

Parallel robots are also applied as micropositioning systems. In Figure 1-24, the hexapod parallel robot M-850 is shown. It was chosen as a surgical robot. The Fraunhofer Institute for Manufacturing Engineering and Automation (IPA), introduced the idea of a surgical robot [8].

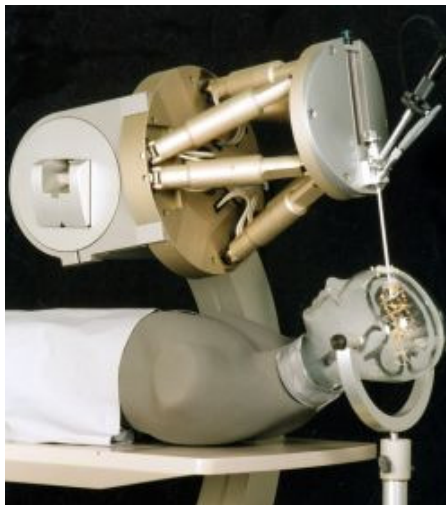


Figure 1-24 M-850 Medical Robot

1.7. Auto-Samplers

Auto-samplers are robotic systems that can automatically deliver a sample into the sample container. Manual sampling is still being used today but is inefficient for research requiring large quantities of samples to be analyzed. Compared to manual sampling, auto-samplers provide continuous, reproducible sampling freeing researchers of repetitive tasks. There are two kinds of auto-samplers; one is the rotating auto-sampler and the other is planar auto-sampler.

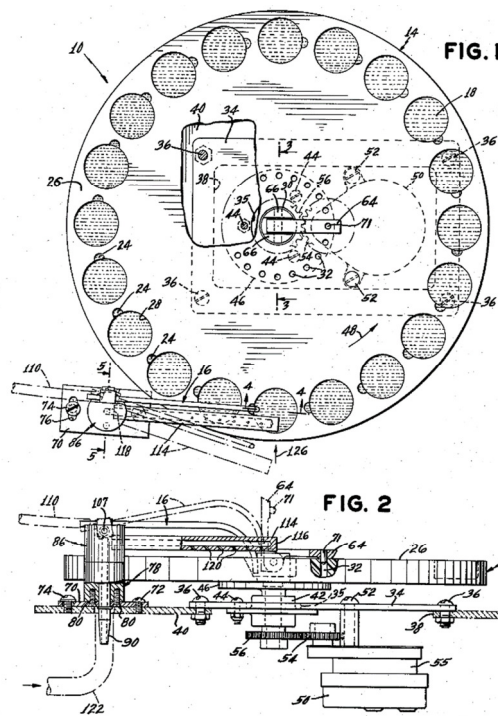


Figure 1-25 Automatic analyzing apparatus [13]

The first automatic device designed for sampling was introduced by US inventor Skeggs in 1959. One object of the present invention is the provision of an apparatus for

automatically feeding in succession a plurality of different liquid samples [13]. The Rotating auto-sampler was the first prototype.

1.7.1. Rotating Auto-Samplers

Rotating auto-samplers are composed of a rotary actuator and a linear actuator. The rotary actuator shaft is connected to the center of a round plate, which is the sample container rack. The linear actuator injects the sample into the sample container. As shown in Figure 1-26, rotating auto-samplers are widely used in gas chromatography sampling machines with small amount analysis.



Figure 1-26 Agilent 6850 Automatic Liquid Sampler

1.7.2. Planar Auto-Samplers

Planar auto-samplers have two linear actuators. These two linear actuators are

orthogonally installed. One linear actuator drives the sampling unit along the X axis and the other one drives the sampling unit along the Y axis. Planar auto-sampler, shown in Figure 1-27, is usually used for larger scale analysis since it can handle test tubes with regular size.

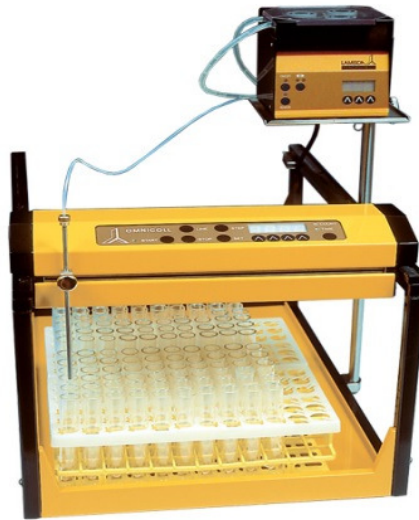


Figure 1-27 Lamda Omnicoll

1.8. Research Objectives

Enhanced Oil Recovery (EOR) refers to the injection of a fluid or combination of fluids to alter the fluid-fluid or fluid-rock properties governing oil recovery, instead of relying on the reservoir pressure to aid recovery. In the absence of a robot, technicians would have to repeatedly sample the fluids over several days. This could potentially lead to unsafe operations due to worker fatigue. Under these circumstances, a robotic automatic sampler

is needed to replace human operation.

The goal of this research project is to design an auto-sampler capable of collecting live oil samples over several days in tubes located in a tray, requiring varied processing times. These samples are used to analyze the composition of the oil and gas. Live oil with dissolved gas is delivered through one tube controlled by the user. It will flow to the auto-sampler, which will position and then inject the live oil into each test tube. Separation of the oil and gas happens in the test tube based on chemical thermodynamics. Generally, this whole process should last several hours. This includes operating the sampling valve upstream.

Live oil conditions are at high pressure (slightly below 1,034 psi) and high temperature (up to 200°C). The quantity of samples will vary with experiment and one complete experiment may last several days. Each sample is an oil and gas mixture, which requires a guarantee of user safety and sampling consistency. The conditions and length of experiment time (up to two weeks in duration) make sampling unsuitable and dangerous for human manipulations.

1.9. Contribution from the Thesis

The objective of this research is to design, develop, and test an auto-sampler for fluid analysis from specialized core flooding experiment. The contributions from this research are outlined below:

Modeling and analysis of a Five-Bar manipulator using bond graph theory: The traditional method to analyze the robot dynamic performance is Newton-Euler method or Lagrangian method. In this research, bond graph theory is used as a new approach to model the Five-Bar system. It is a new method applied to the robot system and it differs from traditional modeling using dynamic equations, while it is a method to describe the energy exchange within the system. The dynamic performance of the manipulator under control task is modeled and analyzed.

Five-Bar workspace and structure optimization: Traditionally, the Five-Bar workspace is modeled based on the geometric method. In this research, the workspace and singularity are modeled based on the vector method, which is more efficient and more general than the geometric method.

Design and development of an Auto-Sampler based on Five-Bar manipulator: Auto-samplers are usually designed based on Cartesian or rotary structures. In this research, it is the first custom-designed Five-Bar Auto-Sampler that is designed and fabricated for crude oil sample handling applications. It has a linear actuator for injection and extraction, which is essential for live oil fluids collection.

Development of a high performance embedded system controlling the manipulator using Beaglebone Black: Auto-samplers typically use low-performance micro controllers.

In this research, a single-board computer Beaglebone Black is applied as the core controller, as it is more powerful, has a low-cost and is more configurable than traditional MCU (Micro Control Unit). It is a new compact controller that came out in 2013 and is widely used in robot control, signal processing, 3D printers etc. In this research, it is the first time Beaglebone Black has been applied as the core controller of an auto-sampler. Both hardware and firmware were implemented for the control operation.

1.10. Organization of the Thesis

Chapter 2 introduces the overall robot design detailing the conceptual design, peripheral design and risk analysis.

Chapter 3 introduces different kinematic models, for example, the geometric model and the vector model. Then it presents forward kinematic analysis and the explicit resolve process is obtained. Finally, it shows the Matlab simulation of robot workspace and singularity analysis.

Chapter 4 provides the process of using the Bond-Graph method to model the auto-sampler's dynamic performance. It introduces the history of bond graph modeling. Then it will use the bond graph to model the auto-sampler and show the obtained dynamic simulation results.

Chapter 5 provides the details of the design and fabrication of the Five-Bar auto-sampler system. It includes the development of the manipulator and the electronic circuit.

Chapter 6 provides the details of the system instrumentation. The development of operational logic and controller is introduced. The Labview GUI is developed and presented in this chapter.

Chapter 7 delivers the commissioning of the Five-Bar autosampler. The test scripts are proposed and related tests are performed. Three tests, operational test, failure test, and fluid test, are obtained with related test results.

The final Chapter 8 summarizes the whole thesis. It gives the conclusions and future work can be done related to the auto-sampler in oil and gas application. The future work if the request is introduced in this chapter.

Chapter 2

2. Overall Robot Design

In this chapter, as the start-up stage, the Auto-Sampler needs an overall plan of the design.

The first objective is the conceptual design of the overall auto-sampler, taking into consideration any design constraints. The auto-sampler should be designed to follow and satisfy these constraints. The traditional auto-sampler is introduced and new options considered. These alternatives are compared based on design criteria and the most suitable concept is selected. The peripheral of the Auto-Sampler is designed and presented.

In the end, a risk analysis of the Auto-Sampler unit is performed and presented. The detailed design method, such as kinematics analysis, dynamics analysis, and control are discussed in the following related chapters.

2.1. Design Constraints

As introduced in the previous research objective section, the auto-sampler will be used to sample, collect, and separate live oil samples from a high pressure, high temperature specialized core analysis experiment. Design constraints for the auto-sampler include the following points.

- The design should be safe for user operation.

- The auto-sampler can complete all sampling work in the lab environment.
- The auto-sampler will be installed in the Hibernia EOR laboratory and the dimensions will be limited to 1.22 m (L) × 0.92 m (W) × 1.00 m (H)

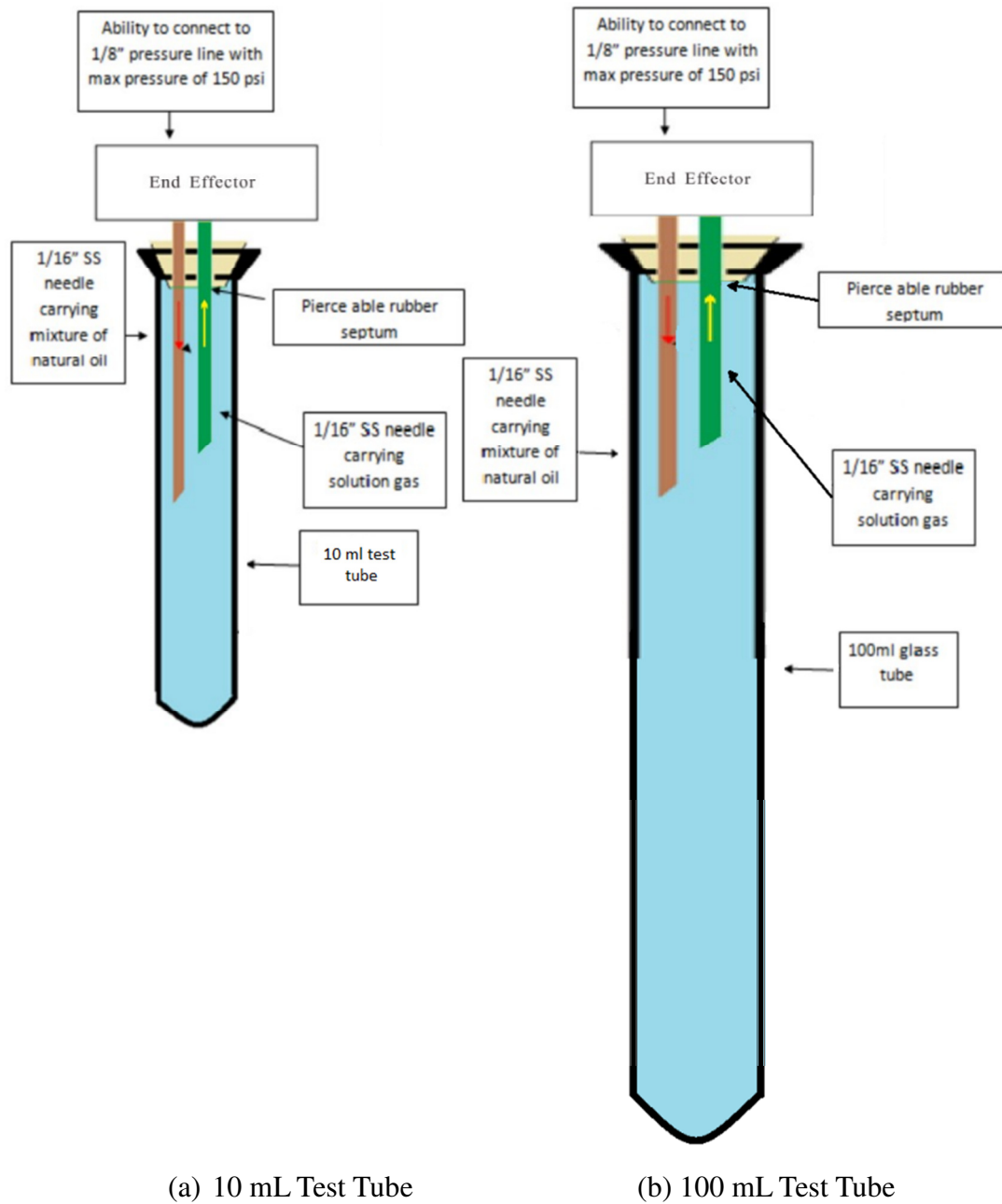


Figure 2-1 Side View of Needle and Test Tube

- The injection and extraction processes happen concurrently, as is shown in Figure 2-1. The process time is limited to 48 hours for each test tube. After all test tubes have finished, a technician will need to intervene, switch out test tubes and restart the program.
- The entire experiment can last several days.
- The operation objects are specified for 10 mL and 100 mL test tubes. The test tubes should be located in the related tube rack.
- The lab is an indoor environment; the operating temperature will be set to 20°C with minor variations due to heating and ventilation.

2.2. Conceptual Design

Based on the previous chapter, the potential robot structure concepts are limited to three alternatives, including Cartesian, SCARA, and Five-Bar robots. In this section, in order to decide with which type of robot to design, a technical comparison matrix on weighted sum method (WSM) is used to screen for the best robot type. The robot types are compared and the most reasonable one chosen.

2.2.1. Methodology

In order to select the conceptual design to be developed, the weighted sum method (WSM) [32] is the most well-known and the simplest multi-criteria decision analysis for evaluating

several alternatives in terms of a number of decision criteria.

The first step is to list all the necessary criteria for the conceptual design. The better the concept meets the criteria, the higher the score it can get in this criteria section. Then in the second step, each criterion has its own weight of importance for this research. The score the concept gets in the criteria is multiplied by the weighted percentage of the same criteria leading to the weighted score. Finally, adding up all the weighted scores from each criterion results in the final score for the concept. The selected concept will be the one with the highest final score.

Cost (30 %)

The cost was given the maximum weight because it is the most important aspect of the design product. This product is designed as lab equipment for academic purposes. Hence, a low-cost design was a very important criterion.

Payload (30%)

The task suitability of a robot is directly dependent on how many types of end-effector can be installed on the robot. Hence, if the robot has the capability to install heavier end-effectors, it will expand the possibility to finish more general tasks. In this design, a linear actuator will be installed as the end-effector to fulfill the vertical injection and extraction motion.

Actuator (20%)

A simpler design is usually more robust and easier to maintain. The number of actuators is an important criterion. The final design should have the least number of actuators. The type of actuator is another part of the criteria. Rotary actuators have many advantages over linear actuators. Rotary actuators have a less mechanical backlash. Rotary actuators have higher power conversion efficiency than linear actuators. Linear actuators are usually transformed from rotary actuators, and this process contains energy loss during the transition. Linear actuators need to be guided, have alignment problems, can have hard spots, sticky slip, low stiffness, and small bandwidths.

Research Value (20%)

One of the design objectives was to push the limit of low-cost pick-and-place and palletizing equipment. If the design had more potential problems to be solved, the greater the research value was given for the design.

2.2.2. Results

The total score of each criterion is three points. In terms of research value, the Cartesian robot is the most common one and it has been widely applied in auto-sampler design, and linear actuators are easy to control. SCARA has also been thoroughly researched and has been produced on a large scale, however, in auto-sampler design, it is a new idea. The

Five-Bar robot has not been widely produced and applying it as an auto-sampler is a totally new idea.

In order to justify the comparison, there are three market available Cartesian type Auto-Samplers. They are Fisher CF1, Buchi C-660, and Lamda OMNICOLL so this concept gets one point. There is only one SCARA based Auto-Sampler as Agilent 7620-AS so that SCARA gets two points. Auto-Sampler based on Five-Bar is not available currently. So Five-Bar concept gets the highest score as three points.

Table 2-1 Research Value Comparison

Concepts	Research Value Points
Cartesian Robot	1
SCARA Robot	2
Five-Bar Robot	3

In order to justify the comparison, for the electrical linear actuator, it is usually designed for converting the rotary motion to linear motion through a lead screw or ball screw. Energy will be lost during this motion conversion process. The conversion efficiency varies from 85% to 90%, while the rotary actuator is usually greater than 95%.

The precision of the linear actuator is worse than the rotary actuator. Cartesian robot motions are performed by two linear actuators while SCARA and Five-Bar motions are both performed by two rotary actuators. As a result, Five-Bar and SCARA are allocated

three points and Cartesian is designated two points.

Table 2-2 Actuator Comparison

Concepts	Actuator Points
Cartesian Robot	2
SCARA Robot	3
Five-Bar Robot	3

As for robot payload, SCARA is not good at heavy load for its serial mechanical structure. The arm deflection is another problem for SCARA. As mentioned in chapter two, the Five-Bar is a parallel robot, and it has a better payload than SCARA robot due to its mechanical structure. Since the Cartesian robot supports the frame consistently over the entire range of motion, a typical Cartesian robot can pick and place a heavier load than a Five-Bar robot if the frame is heavy and strong enough.

In order to justify the comparison results, the load/mass property is calculated. For Cartesian robot, for example, EPSON EZ3, it has 10 kg payload with 40 kg self-mass, so its load/mass is 0.25. For SCARA robot, for example, EPSON G3 has 3 kg payload with 27 kg self-mass, so its load/mass is 0.11. As for Five-Bar robot, in this research, our design has a 2.7 kg payload with 8.5 kg self-mass, so its load/mass is 0.32. So Five-Bar robot has the highest three points, while Cartesian gets two points and SCARA gets one point.

Table 2-3 Payload Comparison

Concepts	Payload Points
Cartesian Robot	2
SCARA Robot	1
Five-Bar Robot	3

In order to reach the same precision level as SCARA and Five-Bar, Cartesian will need very precise linear actuators, which will raise the cost. SCARA robot has good precision. But as mentioned, the serial mechanical structure has the arm deflection problem. So with the same size, SCARA has to cost more in arm strength in material and better motor performance than Five-Bar robot.

In order to justify the comparison, three quotations are obtained from the market. A Cartesian system costs \$12,000 CAD, a SCARA system costs \$21,000 CAD, and a Five-Bar system costs \$15,000 CAD. The points are calculated as $3 - \frac{P_i - 12000}{12000} \times 3$, where P_i is the price of the related system.

Table 2-4 Cost Comparison

Concepts	Cost Points
Cartesian Robot	3
SCARA Robot	0.75
Five-Bar Robot	2.25

Based on previous comparisons and WSM introduction, results are shown as following Table 2-5.

Table 2-5 Concept Selection Results

	Research (20 %)	Actuator (20 %)	Payload (30 %)	Cost (30 %)	Total
Cartesian	0.2	0.4	0.6	0.9	2.1
SCARA	0.4	0.6	0.3	0.2	1.5
Five-Bar	0.6	0.6	0.9	0.7	2.8

Based on results summarized in Table 2-5, the Five-Bar parallel robot was chosen as the design solution for the lab auto-sampler.

2.3. Peripheral Design

After choosing a Five-Bar manipulator conceptually, the peripheral ancillary components have to be designed before the manipulator design, including the test tubes chosen and the test tube rack design.

The design constraints include physical size, cost, and material compatibility. The proposed auto-sampler must fit within a physical space of 0.92 m width × 1.22 m length × 1.00 m height.

The oil is introduced into the work cell through one 1/8” pressure piping tube. After the experiment, gas will be extracted through the tube and transmitted into the next section.

The whole process diagram is shown in Figure 2-2. Test tubes will sit in the tube rack and rack, which is manually loaded by a technician.

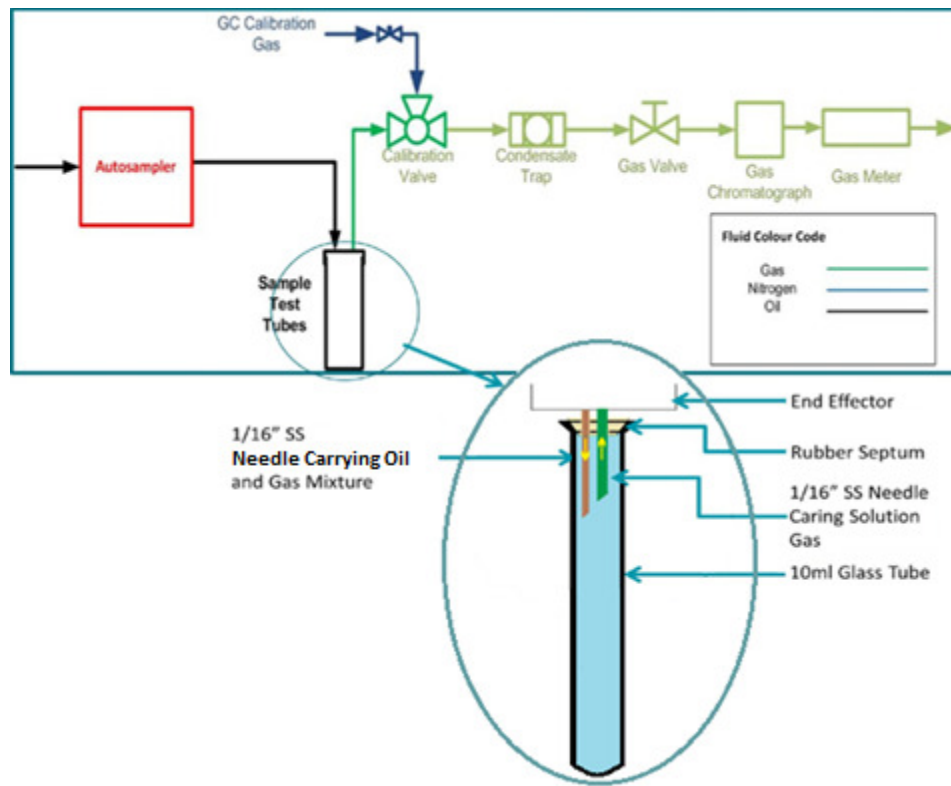


Figure 2-2 Auto-Sampler within Process Flow Diagram

2.3.1. Methodology

The suitable test tube rack should be light weight, not dissolving with crude oil with relatively low cost. The common materials are aluminum alloy 6061 and acrylic. As for the acrylic, it is not dissolving with crude oil, as well as the Aluminum alloy 6061. As for the material density, aluminum 6061 is $2768\text{kg}/\text{m}^3$ while the acrylic is $1190\text{kg}/\text{m}^3$. As for the material cost, the acrylic sheet with 0.25 inch thickness is $\$17/\text{ft}^2$ while the same size of the aluminum alloy 6061 sheet is $\$41/\text{ft}^2$. Moreover, the acrylic sheet is easy to be cut and customized machining for two sizes of test tubes. With proper drilling, it can firmly hold test tube.

2.3.2. Result

Two sizes of test tubes are shown in Figure 2-3. The detailed dimensions of two different test tubes are shown in Table 2-6.



Figure 2-3 Comparison of Two Kinds of Tubes

Table 2-6 Dimensions of Different Test Tubes

Test Tube	Inner Diameter	Outer Diameter	Body Diameter	Length
Small (10 mL)	7.50 mm	18.65 mm	12.70 mm	246.00 mm
Large (100 mL)	24.80 mm	34.10 mm	32.90 mm	313.00 mm



Figure 2-4 Plastic Lid for Test Tube

Each test tube will be covered by a matching lid, which consists of three parts, a plastic head, a rubber interlayer, and a plastic bottom, as shown in Figure 2-4. The lid has a screw thread and can be fixed over the mouth of the test tubes. The outer diameter is 16.00 mm, the inner diameter is 11.40 mm, and the gross length of plastic cap is 52.1 mm. The gross length of the test tube with the cap is about 278 mm.

For the test tube rack, it is made of the acrylic. For one small rack, the length is 335 mm, the

width 268 mm, the height 245 mm. It holds thirty test tubes. The ridge between two cells is 45 mm. The technician will load racks into the work cell. Details of the rack are shown in Figure 2-5. In order to ensure the stability of test tubes during the whole process, a flat table should be fixed in the work cell. It has four metal edges and a table bar to immobilize the rack.

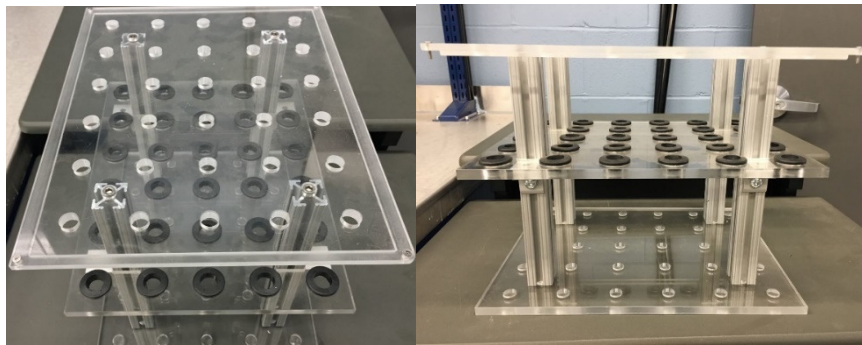


Figure 2-5 Small Racks for Small Test Tubes

This is a general design because if the diameter of each small test tube hole is expanded on the top plate, it will turn to the rack for the large test tubes. The reasons for using the acrylic as the rack material are enough strength to hold glass test tubes, cheaper than same volume aluminum, and not dissolved by crude oil.

2.4. Risk Analysis for Auto-Sampler

As introduced in the previous sections, the Auto-Sampler is just one unit of the whole lab experiment process. The risk analysis of the rest surrounding equipment has been done by the Hibernia EOR lab. However, the risk analysis for Auto-Sampler is still essential and

important to the overall lab safety.

2.4.1. Methodology

In safety and risk engineering, there are two common techniques used for risk analysis, which are Hazard and Operability (HAZOP) and Failure Mode Effect Analysis (FMEA) [14]. They are applied for risk analysis with different purposes.

HAZOP is a simple structured methodology for hazard identification and assessment. Piping and instrumentation diagram (P&ID), process flow diagram (PFD), material flow diagrams, and operating manuals are examined to identify causes and consequences for all possible deviations from the normal operation that could arise. FMEA is often used as an alternative method to HAZOP studies [14]. It is an examination of an individual component such as pumps, vessels, valves, etc. to identify the likely failures which may have undesired effects on system operation.

The difference between those two methods is that HAZOP emphasizes the hazard identification of a whole process based on clear P&ID and PFD. FMEA emphasizes the hazard identification of a single component inside of the process. Moreover, FMEA identifies and eliminates concerns early in the development of a design and focuses on prevention of the risk. After the product concept is settled but before specific hardware is selected or manufactured, it is the best time to apply FMEA [14].

Based on the characteristics of these two methods and PFD is shown in Figure 2-2, the Auto-Sampler is a single component within the whole process and FMEA is more suitable for the research.

2.4.2. Results

Table 2-7 FMEA Sheet for Auto-Sampler

Possible Risks	Cause	Consequence	Protection
No safety distance	Operator gets too close to control Auto-Sampler	Reportable physical injury	Auto-Sampler is remotely controlled through communication cable
			Auto-Sampler is isolated from operator by safety cage
	Ignoring the working condition of the Auto-Sampler	Reportable physical injury	A light tower can make sure working mode recognized in distance
			Offer best practice procedure to operator
Start working cycle without safety cage closure	Operator forgets to close the door before working cycle	Reportable physical injury and loss of process	Door sensor is designed to detect the door whether the door is firmly closed
			Power breaker is designed to cut power the Auto-Sampler if the door is not closed before working cycle
Break in normal working cycle	Safety cage is opened during normal working cycle	Reportable physical injury and loss of process	Door sensor is designed to detect the break in within the normal working cycle
			Power breaker is designed to cut the power of Auto-Sampler
			Door status signal is sent to controller for pausing experiment through communication cable
Leak from piping system	Loose piping or fitting	Contamination and loss of material	Routine equipment check and maintenance
			Safety cage separates operator and Auto-Sampler

The FMEA is performed for the Auto-Sampler and results are shown in Table 2-7. Based on the result, it will be the principle design guideline for the following auto-sampler design.

2.5. Final Design and Discussion

The auto-sampler itself is a five-bar manipulator. It has the advantages of light weight and robust structure. The final physical dimension of the auto-sampler is 0.45 m width×0.55 m length×0.90 m height. The size is smaller than the 0.92 m width×1.22 m length×1.00 m height requirement. The auto-sampler is made of aluminum and the test tube rack is made of acrylic. Both materials are not dissolving with crude oil.

Based on FMEA analysis, essential components have to be considered for the auto-sampler system, including safety cage, light tower, door sensor, and power breaker switch. The safety cage will be used to separate user and the manipulator, not only for the safety of the user but also for avoiding interruptions to the auto-sampler system from the environment. The light tower will let the user and other people around the auto-sampler notice what the current status of the auto-sampler is in. The door sensor is an important part of giving the door status signal to the system controller, which will apply strategies based on the door status. Power breaker is used to cut the power for neutralizing the system when the ongoing experiment is intervened by the user unintentionally.

Chapter 3

3. Kinematics Analysis

3.1. Introduction

The kinematic analysis describes the implicit relationship between geometrical variables and motion variables of the mechanism without considering forces, power, or energy causing motion. Robot kinematics is used to solve the motion relationship between input parts and output parts, such as position, velocity and acceleration and also the geometric configuration parameters of either task space or actuator/joint space. More precisely, for the Five-Bar parallel manipulator, robot position analysis was used to find the relationship between the input actuator angles and the end-effector output position. Robot kinematics has two branches: inverse kinematics and forward kinematics. Inverse kinematics uses the known position of the end-effector to solve the unknown positions of the actuators. Conversely, forward kinematics uses the known positions of the actuators to solve the unknown position of the end-effector. For serial robots, the forward position analysis is easy to calculate but the inverse position analysis is difficult. Conversely, for parallel robots, the inverse position analysis is easy to calculate but the forward position analysis is difficult [34].

3.2. Literature Review

By the definition from Merlet [39], the inverse kinematics consists in establishing the value of the joint coordinates corresponding to the end-effector configuration. The inverse kinematics problem of a Five-Bar robot is defined as solving unknown two motor angles by known conditions, in particular, the end-effector position in Cartesian coordinates.

In 2006, Liu introduced the Geometric method for solving the inverse kinematic problem [36]. In this paper, the kinematic model is built based on geometric relationships. This method is explicit for modeling the Five-Bar manipulator workspace. In 2010, Bonev concluded the previous works and introduced an explicit model based on vectors of the Five-Bar configuration [26]. In our study, the workspace will be simulated based on this model.

In 1991, Angeles introduced the kinematics characteristics of Five-Bar manipulator [37]. In 1990, Gosselin and Angeles introduced analysis method for parallel mechanism [38]. Based on it, the explicit relationship between the end-effector velocity and the input angular velocity is built, which is the Jacobian matrix of the manipulator. By calculating the determinant value of the robot Jacobian matrix, the singularities of the robot can be obtained. Based on the kinematics analysis, the optimized dimensions of the robot are obtained from the simulation results.

As a planar parallel robot, the identification and analysis of the workspace in Cartesian coordinates are the results of the kinematic analysis. The workspace includes effective workspace and boundaries caused by singularities.

The position of a point on XOY plane is inputted into the inverse kinematic model, from which we identify whether or not it is in the effective workspace. The forward kinematic model is used to calculate the boundaries caused by singularities.

After the effective workspace is obtained, the singularity points that exist in the workspace are calculated. Marking all singularity points and connecting all of them, the boundary of the workspace is obtained. By differentiating the inverse kinematic model, the inverse Jacobian matrix is obtained, which links the known end-effector velocity and unknown actuators velocities. By differentiating the forward kinematic model, the forward Jacobian matrix is obtained, which links the known actuators velocities and unknown end-effector velocities. By substituting the point on XOY plane and its related actuator angles into the inverse Jacobian matrix and forward Jacobian matrix, if the determinant of either matrix is zero, then this point is marked as the singularity point. The integrated workspace of the Five-Bar robot is obtained by combining all of the effective workspace points and all of the singularity points connected into the boundary.

3.3. Kinematics Modelling Methodology

In this section, the position analysis of Five-Bar robot will be presented. The position analysis includes solving inverse kinematics problem (IKP) and forward kinematics problem (FKP). In order to solve the IKP and FKP of Five-Bar robot, its inverse kinematic model, and forward kinematic model will be presented in this section.

3.3.1. The Inverse Kinematics Model

In Figure 3-1, a sketch of the Five-Bar robot is shown, where each variable or component is labeled. Inverse kinematics was used to derive the actuator angles from end-effector position.

Proximal arms are labeled as L1 and L2. Distal arms are labeled as L3 and L4. Two active joints are connected with two fixed actuators, labeled as A1 and A2. Three passive joints are labeled as B1, B2, and P. It contains two DOFs on the XY plane. The end-effector is settled at the P joint.

In this section, vectors will be used to solve Five-Bar robot inverse kinematics. The vector approach is a general method and it is applied on DexTAR calibration model, which is testified as a very accurate model [27].

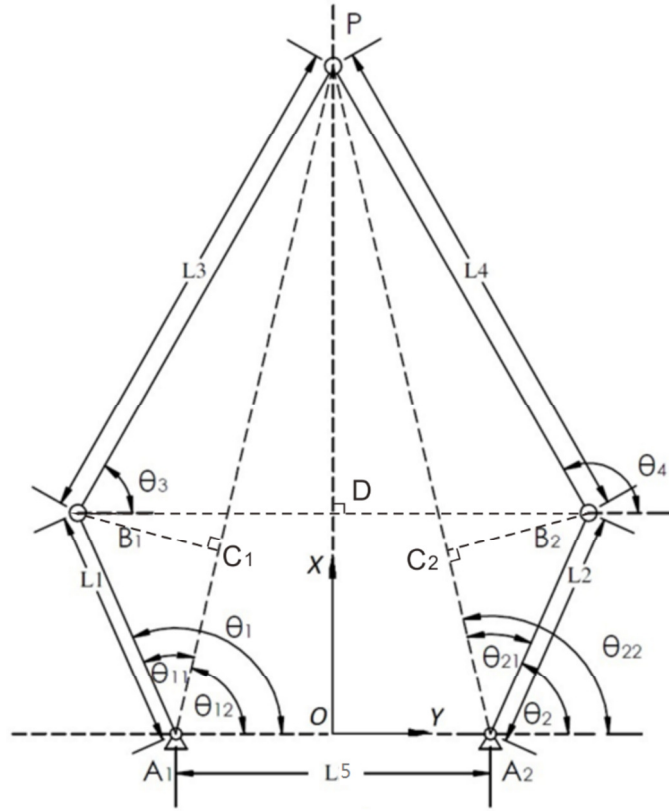


Figure 3-1 Sketch of Five-Bar Robot for Vector Method

For the vector method, the following kinematic derivations obey the fixed base reference frame shown in Figure 3-1. The end-effector's position is defined as

$$P = \begin{bmatrix} x \\ y \end{bmatrix} \quad (3-1)$$

In the fixed base reference coordinate,

$$\overrightarrow{r_{A_1 B_1}} = \frac{|A_1 C_1|}{|A_1 P|} \overrightarrow{r_{A_1 P}} \pm \frac{|B_1 C_1|}{|A_1 P|} \begin{bmatrix} 0 & 1 \\ -1 & 0 \end{bmatrix} \overrightarrow{r_{A_1 P}} \quad (3-2)$$

The operator will decide working mode of the first kinematic chain. The positive sign will lead to positive working mode while negative sign will lead to negative working mode.

$$\overrightarrow{r_{A_1P}} = \overrightarrow{r_{OP}} - \overrightarrow{r_{OA_1}} = \begin{bmatrix} x \\ y \end{bmatrix} - \begin{bmatrix} -\frac{L_5}{2} \\ 0 \end{bmatrix} \quad (3-3)$$

$$L_1^2 - L_3^2 = |\overline{A_1C_1}|^2 - |\overline{C_1P}|^2 \quad (3-4)$$

$$|\overline{A_1P}|^2 = |\overline{A_1C_1}|^2 + |\overline{C_1P}|^2 + 2|\overline{A_1C_1}||\overline{C_1P}| \quad (3-5)$$

Adding (3-4) and (3-5) together gives

$$L_1^2 - L_3^2 + |\overline{A_1P}|^2 = 2|\overline{A_1C_1}|^2 + 2|\overline{A_1C_1}||\overline{C_1P}| = 2|\overline{A_1C_1}||\overline{A_1P}| \quad (3-6)$$

$|\overline{A_1C_1}|$ can be represented as

$$|\overline{A_1C_1}| = \frac{L_1^2 - L_3^2 + |\overline{A_1P}|^2}{2|\overline{A_1P}|} \quad (3-7)$$

$$|\overline{A_1P}| = \sqrt{{}^T r_{A_1P} r_{A_1P}} \quad (3-8)$$

$$|B_1C_1| = \sqrt{L_1^2 - |\overline{A_1C_1}|^2} \quad (3-9)$$

Substituting equations (3-5), (3-7), (3-8), and (3-9) into (3-2) to solve equation for $\overrightarrow{r_{A_1B_1}}$

leads to,

$$\overrightarrow{r_{A_1B_1}} = \begin{bmatrix} x_{A_1B_1} \\ y_{A_1B_1} \end{bmatrix} \quad (3-10)$$

Based on equation (3-10), motor one's desired angle θ_1 can be solved,

$$\theta_1 = \arctan(y_{A_1B_1}, x_{A_1B_1}) \quad (3-11)$$

The same process can be applied to determine the value of θ_2 ,

$$\overline{r_{A_2B_2}} = \frac{|A_2C_2|}{|A_2P|} \overline{r_{A_2P}} \pm \frac{|C_2B_2|}{|A_2P|} \begin{bmatrix} 0 & 1 \\ -1 & 0 \end{bmatrix} \overline{r_{A_2P}} \quad (3-12)$$

The operator will decide working mode of the second kinematic chain. The positive sign will lead to positive working mode while the negative sign will lead to negative working mode.

$$\overline{r_{A_2P}} = \overline{r_{OP}} - \overline{r_{OA_2}} = \begin{bmatrix} x \\ y \end{bmatrix} - \begin{bmatrix} \frac{L_5}{2} \\ 0 \end{bmatrix} \quad (3-13)$$

$$L_2^2 - L_4^2 = |\overline{A_2C_2}|^2 - |\overline{C_2P}|^2 \quad (3-14)$$

$$|\overline{A_2P}|^2 = |\overline{A_2C_2}|^2 + |\overline{C_2P}|^2 + 2|\overline{A_2C_2}||\overline{C_2P}| \quad (3-15)$$

Adding (3-14) and (3-15) together leads to,

$$L_2^2 - L_4^2 + |\overline{A_2P}|^2 = 2|\overline{A_2C_2}|^2 + 2|\overline{A_2C_2}||\overline{C_2P}| = 2|\overline{A_2C_2}||\overline{A_2P}| \quad (3-16)$$

Simplifying equation (3-16) can resolve the value of $|\overline{A_2C_2}|$,

$$|\overline{A_2C_2}| = \frac{L_2^2 - L_4^2 + |\overline{A_2P}|^2}{2|\overline{A_2P}|} \quad (3-17)$$

$$|\overline{A_2P}| = \sqrt{\overline{r_{A_2P}}^T \overline{r_{A_2P}}} \quad (3-18)$$

$$|B_2C_2| = \sqrt{L_2^2 - |\overline{A_2C_2}|^2} \quad (3-19)$$

Substituting equations (3-15), (3-17), (3-18) and (3-19) into (3-12) to solve equation for $\overline{r_{A_2B_2}}$ generates,

$$\overline{r_{A_2B_2}} = \begin{bmatrix} x_{A_2B_2} \\ y_{A_2B_2} \end{bmatrix} \quad (3-20)$$

Based on equation (3-20), the desired angle for motor two can be derived,

$$\theta_2 = \arctan 2(y_{A_2B_2}, x_{A_2B_2}) \quad (3-21)$$

By using the vector approach to building the inverse kinematic model, the position of a point is inputted into the model, showing in equation (3-1). After calculation, the model gives the related actuator angles from equations (3-11), and (3-21). If the two angles are positive, then this point can be marked as a point inside of effective workspace.

3.3.2. The Forward Kinematics Model

The forward kinematics is to determine the pose of the end-effector of a parallel robot from its actuated joint coordinates [39].

The forward kinematics of Five-Bar parallel robot solves unknown value of the end-effector position on Cartesian coordinate by the known two actuating motor angles.

The vector method is used to solve forward kinematics.

Since the two actuating motor angles θ_1 and θ_2 are known, the end-effector position is

$$\overline{OP} = \begin{bmatrix} x \\ y \end{bmatrix} = \overline{OB_1} + \frac{|\overline{B_1D}|}{|\overline{B_1B_2}|} \overline{B_1B_2} + \frac{|\overline{DP}|}{|\overline{B_1B_2}|} \begin{bmatrix} 0 & -1 \\ 1 & 0 \end{bmatrix} \overline{B_1B_2} \quad (3-22)$$

Proximal arms $\overline{OB_1}$ and $\overline{OB_2}$ can be presented as,

$$\overline{OB_1} = \begin{bmatrix} -\frac{d}{2} + L_1 \cos \theta_1 \\ L_1 \sin \theta_1 \end{bmatrix} \quad (3-23)$$

$$\overline{OB_2} = \begin{bmatrix} \frac{d}{2} + L_2 \cos \theta_2 \\ L_2 \sin \theta_2 \end{bmatrix} \quad (3-24)$$

$$L_3^2 - L_4^2 = |\overline{B_1D}|^2 - |\overline{DB_2}|^2 \quad (3-25)$$

$$|\overline{B_1B_2}|^2 = |\overline{B_1D}|^2 + |\overline{DB_2}|^2 + 2|\overline{B_1D}||\overline{DB_2}| \quad (3-26)$$

Adding equations (3-25) and (3-26) together gives,

$$L_3^2 - L_4^2 + |\overline{B_1B_2}|^2 = 2|\overline{B_1D}|^2 + 2|\overline{B_1D}||\overline{DB_2}| \quad (3-27)$$

After factorization and simplification of equation (3-27), we get

$$\left| \overline{B_1 D} \right| = \frac{L_3^2 - L_4^2 + \left| \overline{B_1 B_2} \right|^2}{2 \left| \overline{B_1 B_2} \right|} \quad (3-28)$$

Using vector calculation rules,

$$\overline{B_1 B_2} = \overline{OB_2} - \overline{OB_1} \quad (3-29)$$

$$\left| \overline{B_1 B_2} \right| = \sqrt{\overline{B_1 B_2}^T \overline{B_1 B_2}} \quad (3-30)$$

$$\left| \overline{DP} \right| = \sqrt{L_3^2 - \left| \overline{B_1 D} \right|^2} \quad (3-31)$$

Substituting equations (3-28), (3-29), (3-30) and (3-31) into equation (3-22), the unknown values of x and y can be solved from the known values of θ_1 and θ_2 ,

$$\overline{B_1 B_2} = \begin{bmatrix} m_1 \\ m_2 \end{bmatrix} \quad (3-32)$$

where

$$m_1 = L_5 + L_2 \cos \theta_2 - L_1 \cos \theta_1 \quad (3-33)$$

$$m_2 = L_2 \sin \theta_2 - L_1 \sin \theta_1 \quad (3-34)$$

For simplification purpose, a temporary variable N_1 was used as,

$$N_1 = \frac{\left| \overline{B_1 D} \right|}{\left| \overline{B_1 B_2} \right|} = \frac{L_2^2 - L_4^2 + m_1^2 + m_2^2}{2(m_1^2 + m_2^2)} \quad (3-35)$$

$$\frac{|\overline{DP}|}{|\overline{B_1B_2}|} = \sqrt{\frac{L_3^2 - N_1^2}{m_1^2 + m_2^2}} \quad (3-36)$$

Substituting equations (3-23), (3-32), (3-35) and (3-36) into (3-22) gives,

$$x = L_1 \cos \theta_1 - \frac{L_3}{2} + N_1 m_1 - m_2 \sqrt{\frac{L_3^2 - N_1^2}{m_1^2 + m_2^2}} \quad (3-37)$$

$$y = L_1 \sin \theta_1 + N_1 m_2 + m_1 \sqrt{\frac{L_3^2 - N_1^2}{m_1^2 + m_2^2}} \quad (3-38)$$

$$\overline{B_1P} = \overline{OP} - \overline{OB_1} = \begin{bmatrix} N_1 m_1 - m_2 \sqrt{\frac{L_3^2}{m_1^2 + m_2^2} - N_1^2} \\ N_1 m_2 + m_1 \sqrt{\frac{L_3^2}{m_1^2 + m_2^2} - N_1^2} \end{bmatrix} \quad (3-39)$$

$$\overline{B_2P} = \overline{OP} - \overline{OB_2} = \begin{bmatrix} L_1 \cos \theta_1 - d - L_2 \cos \theta_2 + N_1 m_1 - m_2 \sqrt{\frac{L_3^2}{m_1^2 + m_2^2} - N_1^2} \\ L_1 \sin \theta_1 + N_1 m_2 - L_2 \sin \theta_2 + m_1 \sqrt{\frac{L_3^2}{m_1^2 + m_2^2} - N_1^2} \end{bmatrix} \quad (3-40)$$

$$\theta_3 = \arctan(y_{B_1P}, x_{B_1P}) \quad (3-41)$$

$$\theta_4 = \arctan(y_{B_2P}, x_{B_2P}) \quad (3-42)$$

The forward kinematic model is obtained by vector approach. As mentioned in section 3.2, it is prepared for the following differentiation leading to the singularity calculation.

3.3.3. Robot Working Modes

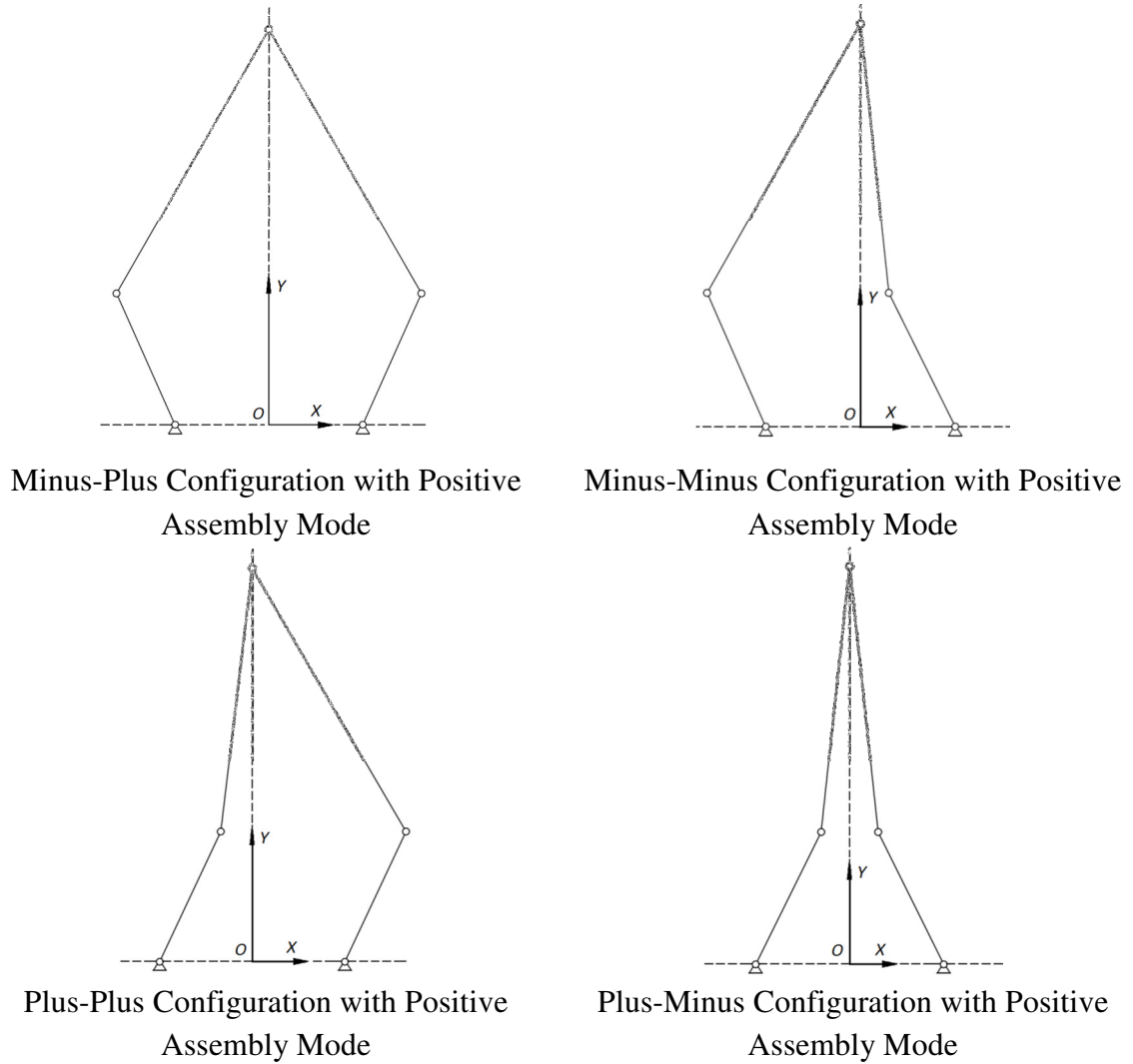


Figure 3-2 Working Modes of Five-Bar Robot

As shown Figure 3-2, if one point is defined as the desired point on the XY plane, usually Five-Bar parallel robot can have four configurations to reach that point, as plus-plus, minus-minus, plus-minus and minus-plus [26]. Negative assembly mode is complex with kinematic singularities, which is not usually used in engineering application. In this work,

the minus-plus configuration with positive assembly mode was chosen.

3.4. Differential Kinematics Modelling Methodology

The differential kinematics is well defined by Tsai [34]. The vector space spanned by the joint variables is called joint space, and the vector space spanned by the end-effector location, the end-effector space. For robot manipulators, the differential kinematics is defined as the mathematical relation that transforms the joint rates in the actuator space to the velocity state in the end-effector space.

Differential kinematics can be derived from two perspectives. From the first perspective, introduced by Huang [35], Jacobian matrix is implemented for the conversion between robot output velocities and input velocities, by differentiating inverse kinematic model and forward kinematic model.

From there as the second perspective, Gosselin moved further to build the relationship between the output velocity V and \dot{q} [38]. If the output position is X and the input angle is q , the robot input output implicit equation can be defined as,

$$f(q, X) = 0$$

After the differentiation with respect to time, it can be written as,

$$AV + B \dot{q} = 0$$

Where $A = \frac{\partial f(q, X)}{\partial x}$ and $B = \frac{\partial f(q, X)}{\partial q}$ and the forward kinematic Jacobian matrix can be derived as,

$$J_f = -A^{-1}B$$

The inverse kinematic Jacobian matrix can be derived as,

$$J_i = -B^{-1}A$$

In this section, we will accept Huang's method. By using the inverse kinematic model in section 3.3, all effective points can be found and combined as the effective workspace, which is a part of the kinematic analysis. As another part of the kinematic analysis, the singularity should be obtained and combined into the workspace boundary. In order to do it, the inverse Jacobian matrix and forward Jacobian matrix should be derived.

We can substitute any point on XOY and its related two actuator angles into inverse Jacobian matrix and forward Jacobian matrix. If either matrix determinant value equals zero, it means this point is a singularity point. If all singularity points are obtained and combined, the singularity points lead to the workspace boundary locus. The detailed methodology about singularity derivation is introduced in this section.

3.4.1. The Forward Differential Kinematics Model

In this sub-section, the forward Jacobian matrix will be derived through the forward differential kinematics model. The determinant value of forward Jacobian matrix will contribute to the judgment of singularity point.

The Jacobian matrix can be written as $J(q)$. If the end-effector velocity is V and the input velocity is \dot{q} , then

$$V = J(q) \dot{q}$$

$$\dot{x} = \frac{\partial x(q_1, q_2)}{\partial t} = \frac{\partial x(q_1, q_2)}{\partial q_1} \frac{\partial q_1}{\partial t} + \frac{\partial x(q_1, q_2)}{\partial q_2} \frac{\partial q_2}{\partial t} = J_{F11} \dot{q}_1 + J_{F12} \dot{q}_2 \quad (3-43)$$

$$\dot{y} = \frac{\partial y(q_1, q_2)}{\partial t} = \frac{\partial y(q_1, q_2)}{\partial q_1} \frac{\partial q_1}{\partial t} + \frac{\partial y(q_1, q_2)}{\partial q_2} \frac{\partial q_2}{\partial t} = J_{F21} \dot{q}_1 + J_{F22} \dot{q}_2 \quad (3-44)$$

Based on equation (3-43) and equation (3-44), the relationship between end-effector output velocity V and actuators input velocities \dot{q}_1, \dot{q}_2 can be shown as,

$$V = \begin{bmatrix} \dot{x} \\ \dot{y} \end{bmatrix} = \begin{bmatrix} J_{F11} & J_{F12} \\ J_{F21} & J_{F22} \end{bmatrix} \begin{bmatrix} \dot{q}_1 \\ \dot{q}_2 \end{bmatrix} = J_F \dot{q} \quad (3-45)$$

Expanding equations (3-37) (3-38), the end-effector position can be written as,

$$\begin{aligned}
x = f_1(q_1, q_2) = & \\
& -\frac{L_5}{2} + L_1 \cos(q_1) + (L_5 + L_2 \cos(q_2) - L_1 \cos(q_1)) \times \\
& \frac{(L_3^2 - L_4^2 + (L_5 + L_2 \cos(q_2) - L_1 \cos(q_1))^2 + (L_2 \sin(q_2) - L_1 \sin(q_1))^2)}{2(L_5 + L_2 \cos(q_2) - L_1 \cos(q_1))^2 + (L_2 \sin(q_2) - L_1 \sin(q_1))^2} - \\
& \sqrt{4L_3^2 - \frac{(L_3^2 - L_4^2 + (L_5 + L_2 \cos(q_2) - L_1 \cos(q_1))^2 + (L_2 \sin(q_2) - L_1 \sin(q_1))^2)^2}{(L_5 + L_2 \cos(q_2) - L_1 \cos(q_1))^2 + (L_2 \sin(q_2) - L_1 \sin(q_1))^2}} \times \\
& \frac{(L_2 \sin(q_2) - L_1 \sin(q_1))}{2\sqrt{(L_5 + L_2 \cos(q_2) - L_1 \cos(q_1))^2 + (L_2 \sin(q_2) - L_1 \sin(q_1))^2}}
\end{aligned}
\tag{3-46}$$

$$\begin{aligned}
y = f_2(q_1, q_2) = & \\
& L_1 \sin(q_1) + (L_2 \sin(q_2) - L_1 \sin(q_1)) \times \\
& \frac{(L_3^2 - L_4^2 + (L_5 + L_2 \cos(q_2) - L_1 \cos(q_1))^2 + (L_2 \sin(q_2) - L_1 \sin(q_1))^2)}{2(L_5 + L_2 \cos(q_2) - L_1 \cos(q_1))^2 + (L_2 \sin(q_2) - L_1 \sin(q_1))^2} + \\
& (L_5 + L_2 \cos(q_2) - L_1 \cos(q_1)) \times \\
& \sqrt{4L_3^2 - \frac{(L_3^2 - L_4^2 + (L_5 + L_2 \cos(q_2) - L_1 \cos(q_1))^2 + (L_2 \sin(q_2) - L_1 \sin(q_1))^2)^2}{(L_5 + L_2 \cos(q_2) - L_1 \cos(q_1))^2 + (L_2 \sin(q_2) - L_1 \sin(q_1))^2}} \\
& \frac{2\sqrt{(L_5 + L_2 \cos(q_2) - L_1 \cos(q_1))^2 + (L_2 \sin(q_2) - L_1 \sin(q_1))^2}}{2\sqrt{(L_5 + L_2 \cos(q_2) - L_1 \cos(q_1))^2 + (L_2 \sin(q_2) - L_1 \sin(q_1))^2}}
\end{aligned}
\tag{3-47}$$

Based on equations (3-46) and (3-47), the unknown end-effector positions can be

calculated based on known parameters such as manipulator arm lengths L_1 , L_2 , L_3 and

L_4 , the distance between two motors L_5 , two motor input angles q_1 and q_2 .

After partial differentiation equation (3-46) with respect to input actuator angles q_1 and q_2 , J_{F11} and J_{F12} will be derived. Using a similar method, after partial differentiation equation (3-47) with respect to input actuator angles q_1 and q_2 , J_{F21} and J_{F22} are derived and they are shown in Appendix.

$$J_{F11} = \frac{\partial x(q_1, q_2)}{\partial q_1} \quad (3-48)$$

$$J_{F12} = \frac{\partial x(q_1, q_2)}{\partial q_2} \quad (3-49)$$

$$J_{F21} = \frac{\partial y(q_1, q_2)}{\partial q_1} \quad (3-50)$$

$$J_{F22} = \frac{\partial y(q_1, q_2)}{\partial q_2} \quad (3-51)$$

By substituting J_{F11} , J_{F12} , J_{F21} , and J_{F22} into the matrix, the forward Jacobian matrix J_F can be obtained.

$$J_F = \begin{bmatrix} J_{F11} & J_{F12} \\ J_{F21} & J_{F22} \end{bmatrix} \quad (3-52)$$

3.4.2. The Inverse Differential Kinematics Model

In this sub-section, the inverse Jacobian matrix will be derived through the inverse differential kinematics model. The determinant value of inverse Jacobian matrix will

contribute to the judgment of singularity point.

The inverse Jacobian Matrix can be obtained by a differentiating inverse kinematic model with respect to time. The input actuator velocities \dot{q}_1 and \dot{q}_2 can be represented in end-effector velocities \dot{x} and \dot{y} with the following equations.

$$\dot{q}_1 = \frac{dx}{dt} = \frac{\partial q_1(x, y)}{\partial x} \frac{\partial x}{\partial t} + \frac{\partial q_1(x, y)}{\partial y} \frac{\partial y}{\partial t} = J_{I11} \dot{x} + J_{I12} \dot{y} \quad (3-53)$$

$$\dot{q}_2 = \frac{dx}{dt} = \frac{\partial q_2(x, y)}{\partial x} \frac{\partial x}{\partial t} + \frac{\partial q_2(x, y)}{\partial y} \frac{\partial y}{\partial t} = J_{I21} \dot{x} + J_{I22} \dot{y} \quad (3-54)$$

The following partial differential functions provided by inverse differential kinematics model.

$$J_{I11} = \frac{\partial q_1(x, y)}{\partial x} \quad (3-55)$$

$$J_{I12} = \frac{\partial q_1(x, y)}{\partial y} \quad (3-56)$$

$$J_{I21} = \frac{\partial q_2(x, y)}{\partial x} \quad (3-57)$$

$$J_{I22} = \frac{\partial q_2(x, y)}{\partial y} \quad (3-58)$$

$$\dot{q} = \begin{bmatrix} \dot{q}_1 \\ \dot{q}_2 \end{bmatrix} = \begin{bmatrix} J_{I11} & J_{I12} \\ J_{I21} & J_{I22} \end{bmatrix} \begin{bmatrix} \dot{x} \\ \dot{y} \end{bmatrix} = J_I V \quad (3-59)$$

By substituting J_{I11} , J_{I12} , J_{I21} , and J_{I22} into the matrix, the forward Jacobian matrix J_I can be obtained.

$$J_I = \begin{bmatrix} J_{I11} & J_{I12} \\ J_{I21} & J_{I22} \end{bmatrix} \quad (3-60)$$

3.4.3. Singularities

In the robot workspace, when the robot arrives at certain points, it might not be able to continue moving. It will lose or gain one or more degree of freedoms. These special positions can influence robot normal operation, worse more, break the robot mechanism. These special positions are called as singularities.

In 1990, Gosselin and Angeles provided a method to calculate singularities inside the workspace of the parallel robot [38].

From equations (3-52) and (3-60), the determinant values of J_F and J_I can be represented as,

$$\det(J_F) = \det \begin{pmatrix} J_{F11} & J_{F12} \\ J_{F21} & J_{F22} \end{pmatrix} = J_{F11}J_{F22} - J_{F21}J_{F12} \quad (3-61)$$

$$\det(J_I) = \det \begin{pmatrix} J_{I11} & J_{I12} \\ J_{I21} & J_{I22} \end{pmatrix} = J_{I11}J_{I22} - J_{I21}J_{I12} \quad (3-62)$$

Based on linear algebra knowledge, when the columns of the matrix are dependent vectors

or the rows of the matrix are dependent vectors, the determinant value of this matrix is zero.

Either $\det(J_F) = 0$ or $\det(J_I) = 0$ are satisfied, the point in the workspace can be marked as a singularity point. This will be applied to find the boundary of the workspace in the kinematic analysis.

(a) Serial Singular Configuration

When one side of arms are fully extended or fully folded, the robot falls into the serial singular configuration, introduced by Merlet [39]. Under this singular configuration, the end-effector P will not be able to move along one direction, which is A_1P or A_2P in this case. Serial singularities decide the size of robot workspace outer boundary. This type of singularity is a loss of degree of freedom (DOF) leading to manipulator performing the unpredictable motion.

Singularity loci can be obtained through workspace boundary calculations. A Five-Bar manipulator has four possibilities, which are shown in Figure 3-3. The configuration in Figure 3-3 (a) is the first kinematic chain as A_1B_1P fully extended. The configuration in Figure 3-3 (b) is the second kinematic chain as A_2B_2P fully extended. The configuration in Figure 3-3 (c) is the first kinematic chain as A_1B_1P fully folded. The configuration in Figure 3-3 (d) is the second kinematic chain as A_2B_2P fully folded.

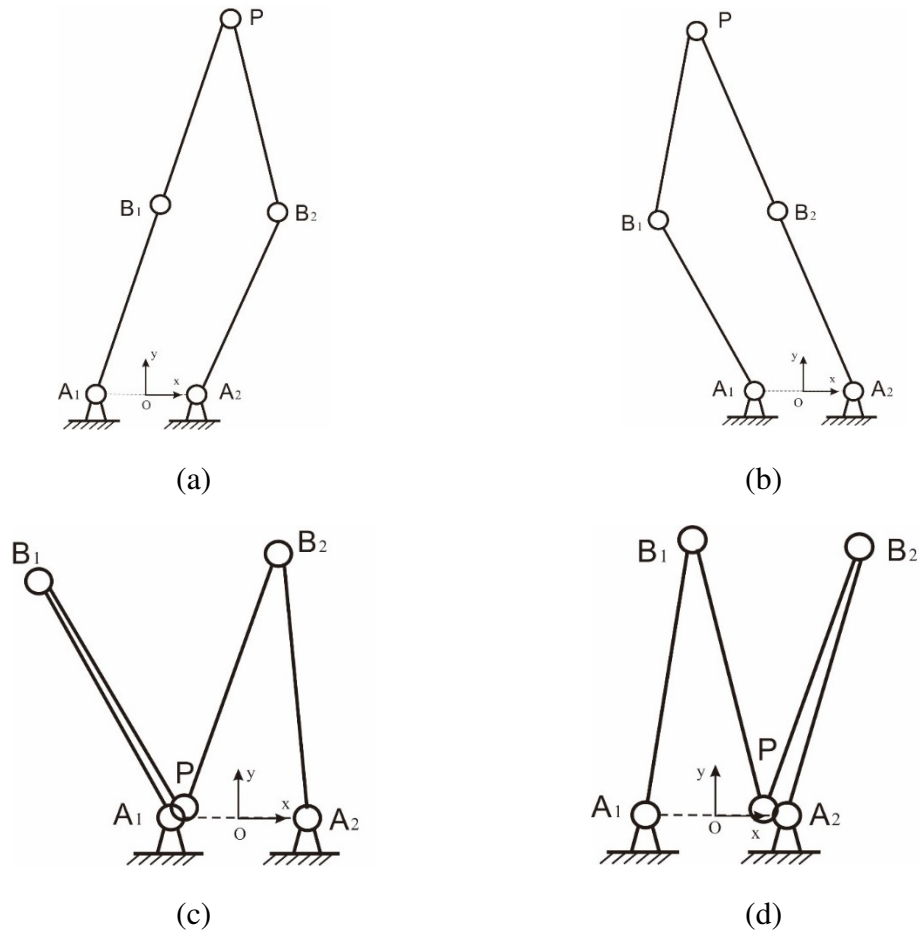


Figure 3-3 Serial Singular Configurations

When the robot is in serial singular configuration, the singularity evaluation condition is

$\det(J_F) = 0$. The end-effector will not be moved along A_1P or A_2P direction.

(b) Parallel Singular Configuration

While serial singularities exist along the outer boundary of robot workspace, parallel

singularities exist within the robot workspace. This kind of singularity is also called a ‘dead

point' [38], as when the robot falls into the parallel singular configuration, it will gain at least one DOF. The robot becomes uncontrollable.

When B_1P or B_2P are in the co-linear position, the Five-Bar manipulator falls into parallel singularity configuration. There are two possible parallel singular configurations for Five-Bar manipulator. The first possible situation is that B_1P or B_2P are fully folded, and points B_1 and B_2 are coincident shown in Figure 3-4.

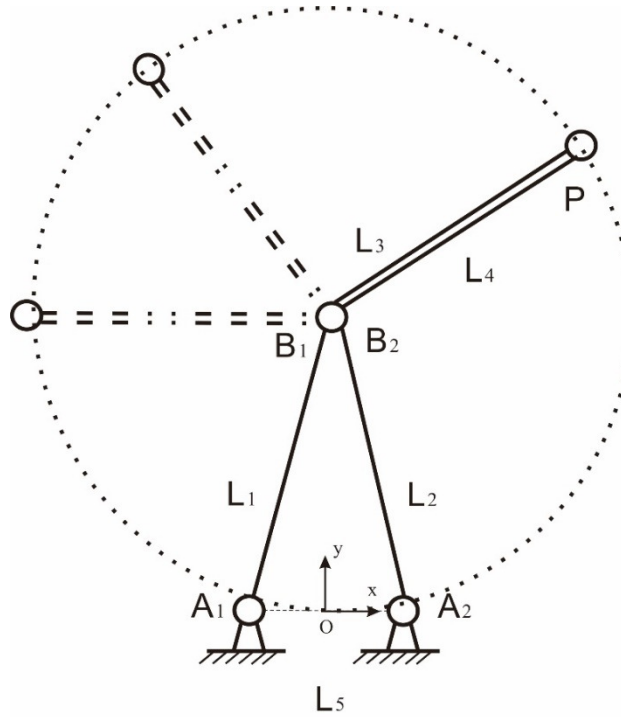


Figure 3-4 B_1P or B_2P Fully Folded

The second possible situation is that B_1P or B_2P are fully extended, hence points B_1 and B_2 are co-linear, as shown in Figure 3-5.

In the first parallel singular configuration, the end-effector P is on a circle with a radius

$r = L_3 = L_4$. So the end-effector contour can be written as,

$$x^2 + \left(y \pm \sqrt{L_1^2 - \frac{L_5^2}{2}} \right)^2 = L_3^2$$

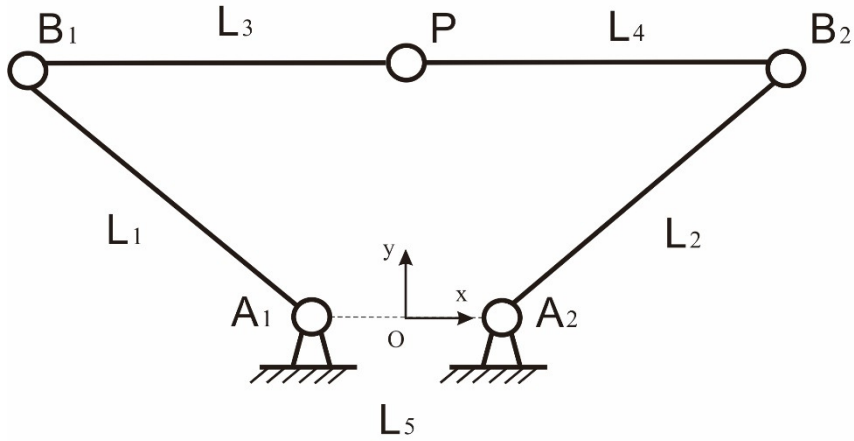


Figure 3-5 B_1P or B_2P Fully Extended

In the second parallel singular configuration, the end-effector P is at the mid-point of line

B_1PB_2 . So the end-effector contour can be written as,

$$x = \frac{L_1 \cos(q_1) + L_2 \cos(q_2)}{2} \quad (3-63)$$

$$y = \frac{L_1 \sin(q_1) + L_2 \sin(q_2)}{2} \quad (3-64)$$

When the robot is in parallel singular configuration, the condition is $\det(J_I) = 0$.

3.5. Kinematics Optimization Methodology

Workspace is an important criterion to evaluate the kinematic performance of the robot. A larger workspace means that the robot can fulfill more tasks. For pick-and-place tasks, the workspace is crucial since the robot can handle more objects on an assembly line. In comparison to serial robots, parallel robots usually cover a usually more limited workspace. At the same time, some sub-volumes may be unavailable in its workspace. Hence the end-effector orientation is not a concern but effectively optimizing the parallel robot workspace is important in design.

3.5.1. Workspace Calculation Algorithm

Based on previous sections about Inverse Kinematics Problem (IKP) and Forward Kinematics Problem (FKP) analysis, the workspace of a Five-Bar robot can be calculated as the following algorithm. It comes from the trial and error method with the help of high-performance computing technology.

As shown in Figure 3-2, an effective point within the five-bar workspace can be reached by one working mode or multiple working modes. The workspace of each working mode should be calculated separately.

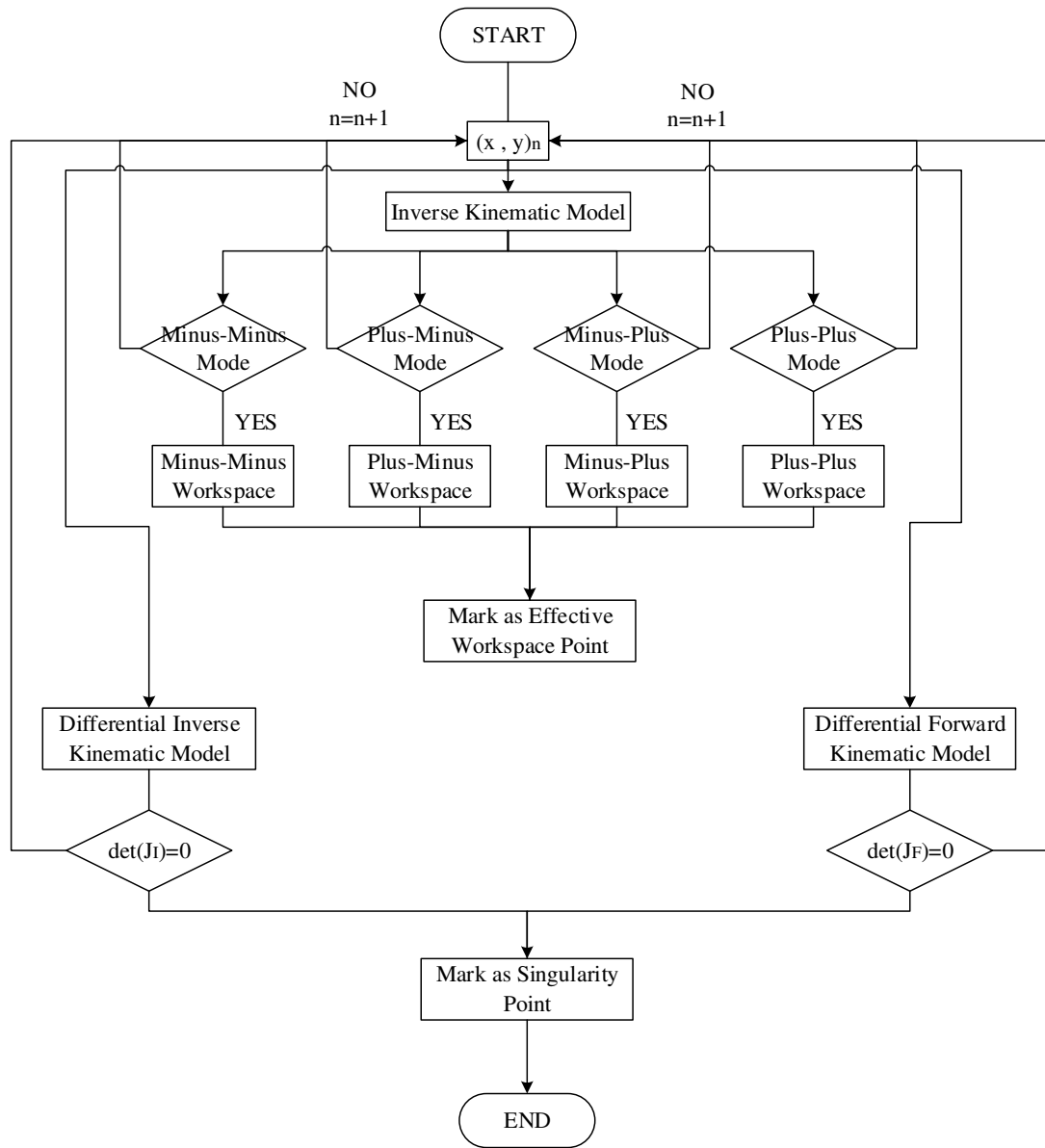


Figure 3-6 Workspace Algorithm

Since the total length of the proximal arm and distal arm is fixed, the effective workspace of Five-Bar robot is limited to a square area, each side equaling to the side arm's total length. In Cartesian planar space, the workspace of Five-Bar robot is located within a square area

with $L_1 + L_2$ as the side length. The area can be evenly divided into $n \times n$ discrete points. The interval between each two close points is $\frac{L_1+L_2}{n-1}$. These points can be compacted into a matrix.

The calculation process diagram is shown in Figure 3-6. The point on the Cartesian coordinate acts as an input. On the one hand, it is put into the inverse kinematic model, derived in section 3.3, to check if it fits any working mode. If the point fits in, it will be marked as an effective workspace point. On the other hand, the point will be put into differential inverse kinematic model and differential forward kinematic model, to check the values of inverse Jacobian matrix and forward Jacobian matrix. If either one equals to zero, this point will be marked as a singularity point. All effective workspace points will compose the effective workspace and singularity points will compose the boundary of the workspace.

3.5.2. Area Ratio Calculation Technique

For a Five-Bar robot, its workspace is determined by the length of the proximal arm, the length of the distal arm and the offset of the two actuators. The relationship between the arm ratio and area ratio is non-linear. Based on the design, there are few restrictions for the area ratio calculation:

1. Adopt inverse workspace calculation algorithm.

2. Only calculate the minus-plus working mode
3. The actuators' offset is 80mm and total side arm's length is 480 mm.

Different proximal arm to distal arm ratios are assigned. Applying those restrictions, applying the workspace calculation algorithm, the effective workspace area and ineffective workspace area belonging to different arm ratios can be calculated. Hence the area ratio versus arm ratio curve can be plotted. The optimized arm length can be calculated.

3.6. Results

In this section, the arm ratio result will be presented. Based on previous workspace algorithm, the area of the workspace can change under different arm ratio. The trend curve will be used to decide the arm ratio to reach the largest workspace area. After the arm dimension is settled, the workspace and singularity locus of each working mode will be calculated and plotted.

In Figure 3-7, the arm ratio is defined as the value of proximal arm length over distal arm length, can influence the effective area workspace. Based on this curve, the maximum effective area is at 0.9 arm ratio. Hence the selected theoretical optimal dimension for distal arm length is 250 mm and proximal arm length is 230 mm.

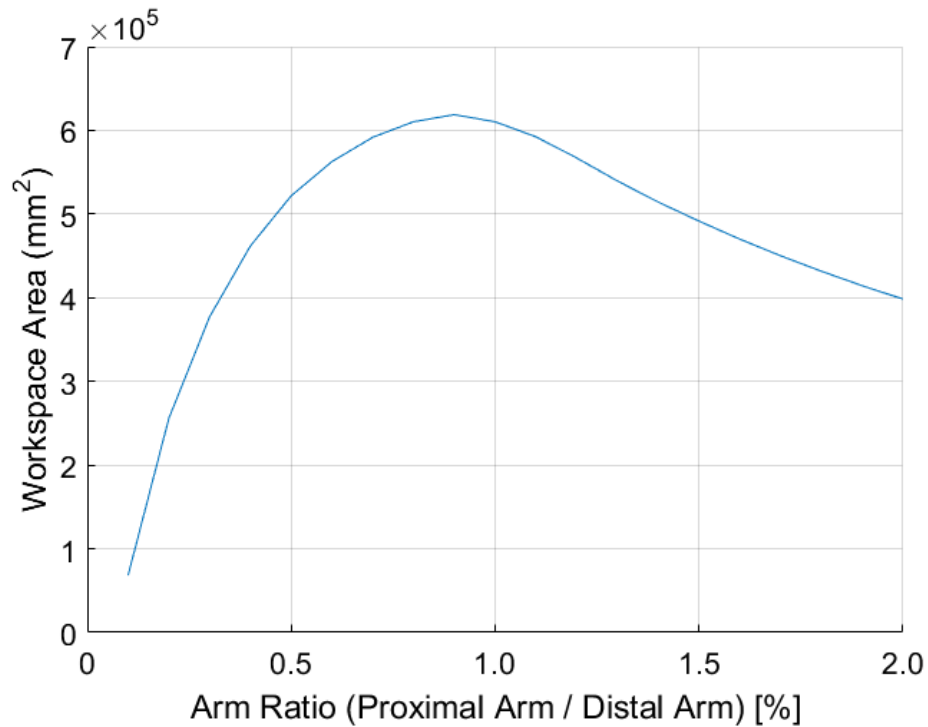


Figure 3-7 Workspace Optimization

By applying the kinematic analysis derived in previous sections and workspace calculation algorithm, we can plot the workspace of Five-Bar manipulator.

A Five-Bar robot has four working modes shown in Figure 3-2: minus-plus mode, plus-minus mode, plus-plus mode and minus-minus mode. Each mode has two assembly modes, which are positive assembly mode and negative assembly mode. In total, a Five-Bar parallel robot has eight different working configurations. However, the negative assembly mode is complex and not useful for industrial application. The problem is more that the assembly mode cannot physically be achieved since bars would collide or occupy

the same space. Therefore, it was not considered further in this work. Only the positive assembly mode will be investigated. The small distal arm length leads to a larger workspace while it introduces longer singularity loci. On the other hand, longer distal arm length leads to shorter singularity loci, which results in a lower chance of losing the degree of freedom, but it will decrease the workspace area.

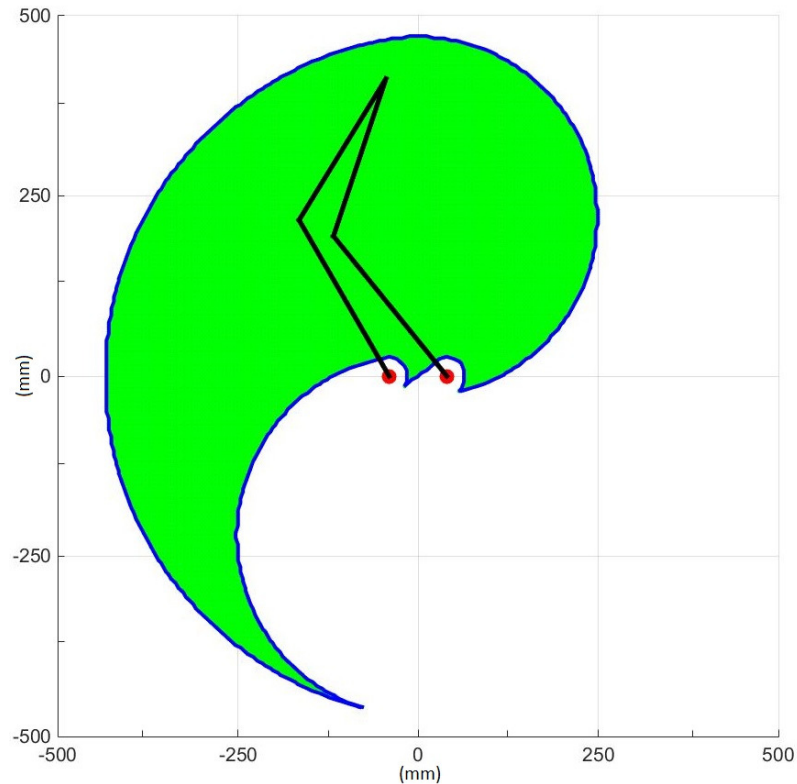


Figure 3-8 Workspace of Minus-Minus Mode

As Figure 3-8 shown, the robot configuration is a minus-minus mode with 230 mm proximal arm, 250 mm distal arm, and 80 mm actuators offset distance. The green area is the effective workspace of Five-Bar robot in minus-minus mode. The unreachable area is

the white area. The blue boundary of the effective workspace is caused by singularity points, which makes robot lose DOF, which is the locus of the workspace.

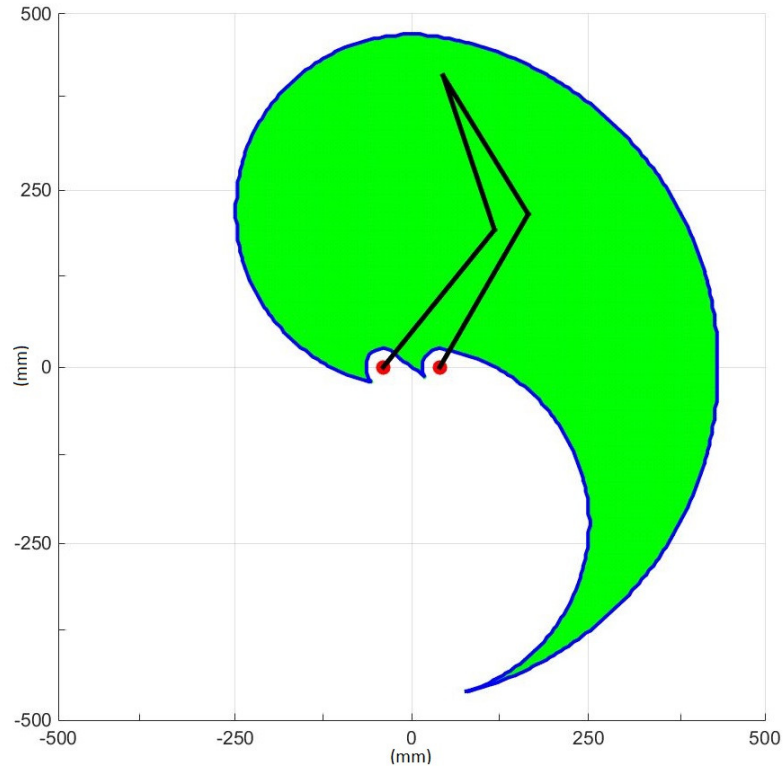


Figure 3-9 Workspace of Plus-Plus Mode

As Figure 3-9 shown, the green area is the effective workspace of five-robot effective workspace in plus-plus mode. As Figure 3-10 shown, the green area is the effective workspace of five-robot effective workspace in plus-minus mode. As Figure 3-11 shown, the green area is the effective workspace of five-robot effective workspace in minus-plus mode, which is actually the mirror image of the minus-minus working mode. The minus-minus mode is the mirror image of plus-plus mode because of symmetric configuration. It has the same size of workspace area.

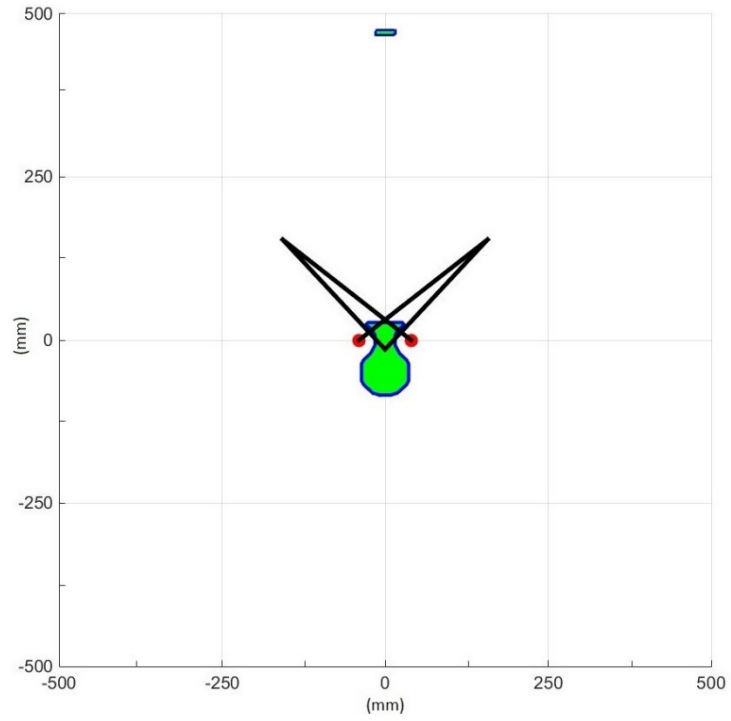


Figure 3-10 Workspace of Plus-Minus Mode

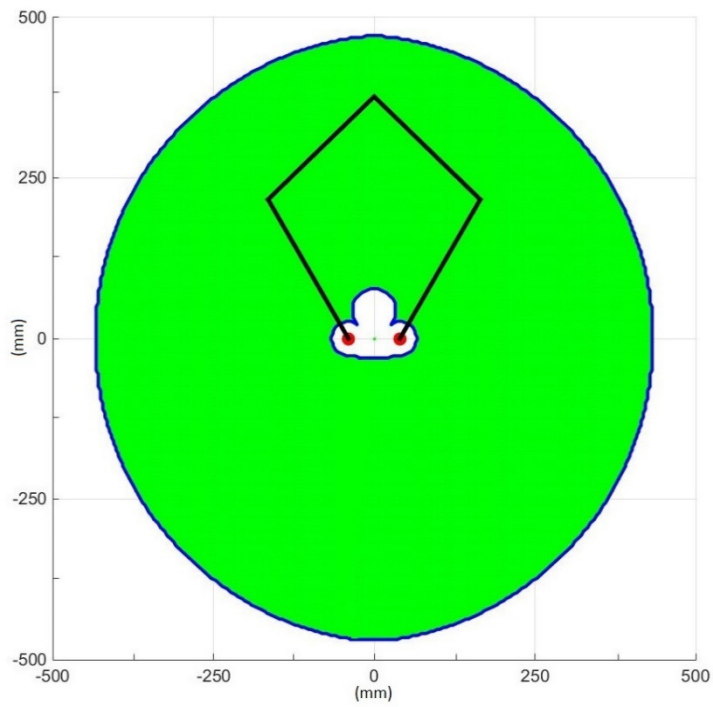


Figure 3-11 Workspace of Minus-Plus Mode

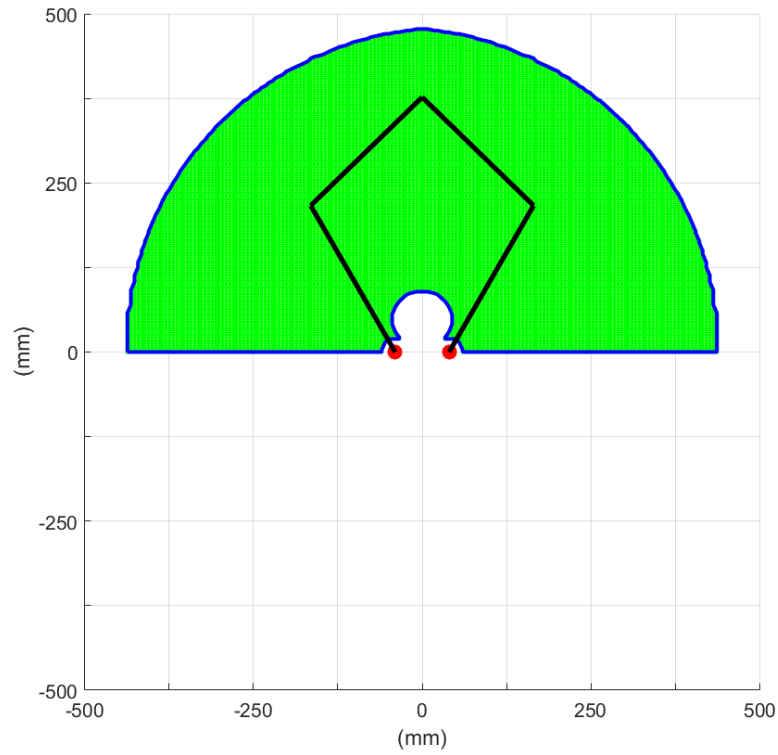


Figure 3-12 Five-Bar Auto-Sampler Workspace

The workspace of this research is shown in Figure 3-12. By comparing the size of all configuration workspaces, the workspaces and singularity boundaries of the plus-plus mode is symmetric to minus-minus mode. The minus-plus mode covers the largest effective workspace with the smallest unreachable area. This is the single working configuration accepted in this research. We only use half of the workspace, which makes the control easier.

Chapter 4

4. Dynamic Analysis

4.1. Introduction

Dynamic analysis is important for robot design. Unlike the kinematic analysis, the dynamic analysis concerns about the robot in motion with velocity and acceleration. It researches the relationship between the forces, the torques, and the robot motion. The purpose of the dynamic analysis is to build a mathematical model describing the dynamic performance of the mechanism. It is the foundation of designing the robot system. The simulation results can be used to find the requirement forces or torques of the actuator and to optimize the control algorithm.

Robot dynamic analysis consists of two parts defined by Tsai [34]. When all actuators' input torque or force and changing trend along the time are known, they are used to derive the end-effector's trajectories in the manipulator workspace, expressed in terms of positions, velocity, and acceleration changing to follow a certain target trajectory. This process is called forward dynamic analysis. Conversely, if the end-effector's velocity and acceleration change along the time are known, they are used to derive the actuators' input torques. This process is called inverse dynamic analysis. Researchers mainly focus on inverse dynamic analysis, which is useful for robot power source design, task-oriented

structure design and to choose actuators. Forward dynamics is utilized for simulation and in control.

In this research, the bond graph model of the five-bar robot is built. In order to justify the relative new bond graph approach, the traditional Lagrangian approach is performed to validate the bond-graph model under the same case. Finally, bond graph model will simulate the robot under PID control and the dynamic simulation results will be presented.

4.2. Literature Review

A parallel robot has a closed kinematic loop, and multiple inputs coupled to each other. These characteristics give parallel robots a complicated dynamics. Several methods exist for solving the dynamic problem.

The Newton–Euler approach is based on Newton's law and Euler's equation, shown in equations (4-1) and (4-2). For linear and angular motion they are directly applied to individual bodies [28]. But this approach requires lots of constraint force analysis, which makes it difficult to lead to actuator torques.

$$\sum F = ma \quad (4-1)$$

$$\sum M + \sum r \times F = r_{cg} \times ma + I\alpha + \omega \times I\omega \quad (4-2)$$

The Lagrangian approach is used from the energy balance perspective [30]. The bond graph

is another dynamic approach [40], which is relatively new compared to the Lagrangian approach.

In 2006, Hu has introduced a simplified Lagrangian model to research the dynamic performance of Five-Bar robot [30].

In 2003, the reduced order model analysis method is used by Ouyang [29]. It is another approach for dynamic modeling of closed loop mechanisms. It is used to develop the dynamic model of the Five-Bar mechanism. The method that he employed for dynamic modeling is from Ghorbel. In 1994, Ghorbel has derived a reduced model for the equations of motion of constrained model for the equations of motion of constrained rigid bodies, including closed-chain mechanism [31]. This modeling method is an approach based on Lagrangian equations.

Lagrangian modeling method is tedious and demanding of high-performance computation. The non-linear results are difficult to optimize. It is caused by the parallel robot characteristic of closed and coupling kinematic structure. As a result of that, Lagrangian traditional modeling method is not the best choice for Five-Bar robot dynamic analysis and engineering design application. It needs a new method to fulfill this objective.

The bond graph is a method to describe system power exchange, transmission, storage, and

dissipation. By introducing real parameters and variables, it can objectively show the relationship between all variables and get explicit state equations. In 1960, bond-graph method was firstly introduced by Paynter [40]. By applying Bond-Graph method in the Five-Bar robot dynamic modeling, a more efficient dynamic model is built. The results will be simulated and presented in this research. Based on the dynamic analysis, the motor torque and arm design are optimized based on the simulation results.

4.3. Bond Graph Modeling

Karnopp and Rosenberg (1990) greatly expanded the bond graph. Many different types of systems can be described using the bond graph, for example, electrical, mechanical, hydraulic, biological, chemical, and economic systems [41].

Planar mechanisms were simulated using bond graph by other researchers. Karnopp and Margolis (1979) described the planar mechanism referring to the bond graph [42]. Zeid [43] simulated joint effects on mechanisms using bond graph theory, which precisely describes the energy exchange through joints. A robot system includes mechanical, electrical, magnetic, and control components. The Five-Bar robot modeling is based on Jian's model [45].

Bond graph roots from the energy conversion perspective. A bond graph model is particularly useful to describe systems in which a variety of elements in different energy

domains interact [44]. The electrical motor is an example as it converts electrical energy to mechanical energy. Another example is two jointed rods with one fixed and another one rotating. It transmits mechanical energy to the following rod. So the bond graph can be used to model the electrical motor and two jointed rods. As for a system, if a separate component of the system can be modeled, the system composed of these parts can be modeled by connecting them together. Energy exchange is used to connect between parts within the system. In different energy domain, effort and flow stand for different names and units, shown in Table 4-1.

Table 4-1 Effort and Flow in Different Energy Domain [41]

Energy Domain	Effort (e)	Unit	Flow (f)	Unit
Mechanical Translation	Force	N	Linear Velocity	m/s
Mechanical Rotation	Torque	$N \cdot m$	Angular Velocity	rad/s
Electrical	Voltage	V	Current	A
Hydraulic	Pressure	Pa	Flow Rate	m^3/s

The basic energy transmission is shown in Figure 4-1, where there is a stroke on the bond called the causal stroke. The causal stroke on either end of the bond has a different meaning. (a) If the causal stroke is on the B side, it means effort is output of A, input to B; flow is output of B, input to A. (b) If the causal stroke is on the A side, it means effort is output of B, input to A; flow is output of A, input to B [41]. And the half-arrow is defined as the direction of positive energy flow.

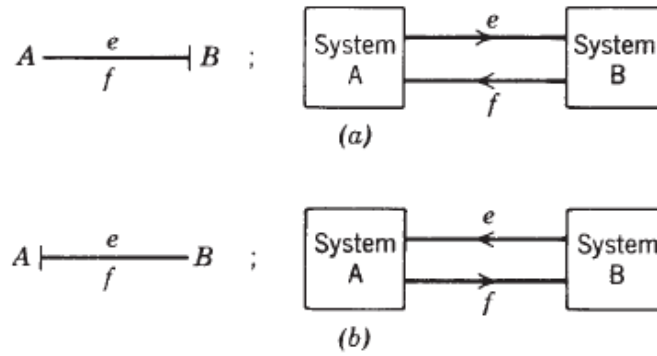
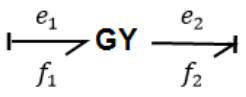
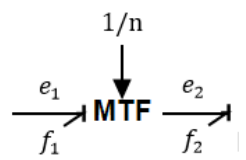
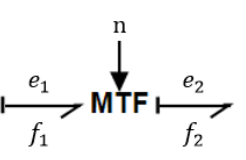


Figure 4-1 Bond Graph Causality [41]

The basic components in the bond graph are introduced in Table 4-2.

Table 4-2 Basic Components in Bond Graph

Name	Category	Symbol	Equations	Explanation
0 Junction	Effort-Equal Junction		$f_1 + f_2 + f_3 = 0$ $e_1 = e_2 = e_3$	
1 Junction	Flow-Equal Junction		$f_1 = f_2 = f_3$ $e_1 + e_2 + e_3 = 0$	
Transformer	Effort-In Causality		$f_1 = (1/n)f_2$ $e_2 = (1/n)e_1$	(1/n) is the constant value in "TF"
	Effort-Out Causality		$f_2 = (n)f_1$ $e_1 = (n)e_2$	(n) is the constant value in "TF"
Gyrator	Effort-In Causality		$f_1 = (1/r)e_2$ $f_2 = (1/r)e_1$	(1/r) is the constant value in "GY"

	Effort-Out Causality		$e_2 = (r)f_1$ $e_1 = (r)f_2$	(r) is the constant value in “GY”
Modulated Transformer	Effort-In Causality		$f_1 = (1/n)f_2$ $e_2 = (1/n)e_1$	(1/n) is the variable in “MTF”, defined by outside signal
	Effort-Out Causality		$f_2 = (n)f_1$ $e_1 = (n)e_2$	(n) is the variable in “MTF”, defined by outside signal

As bond graph modeling for the five-bar manipulator, the four arms are modeled as rigid bars. Two DC motors are modeled in the bond graph. These components are connected by rotation joints, which are modeled as parasitic elements. The five-bar manipulator bond graph model is obtained by connecting them one by one. The energy is transmitted between them and represented in the bond graph.

Many new bond graph practitioners represent bond graphs as a revolutionary new approach that is different from Newton-Euler or Lagrangian. Bond graphs are a very convenient way of representing either of those methods. The biggest advantages of bond graphs for five bar mechanism are: 1) they make it easier to implement multibody systems since by constraining the velocities. It automatically satisfies Newton’s Laws. Constraint forces can

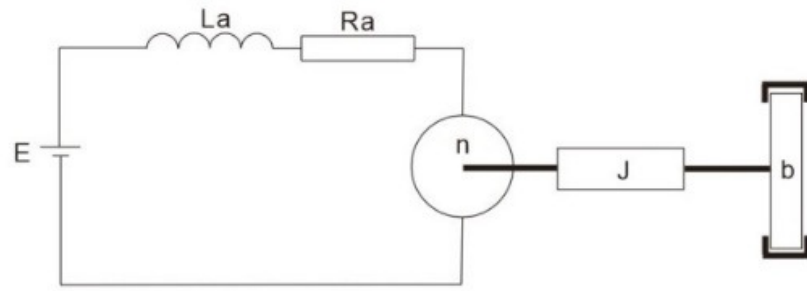
be easily generated by compliant joint elements. Parasitic elements can be implemented in ways other than bond graphs. 2) bond graphs make a model reduction, model expansion and interfacing mechanism models with controllers and electrical systems easier.

4.3.1. Bond Graph Modelling of the Actuators

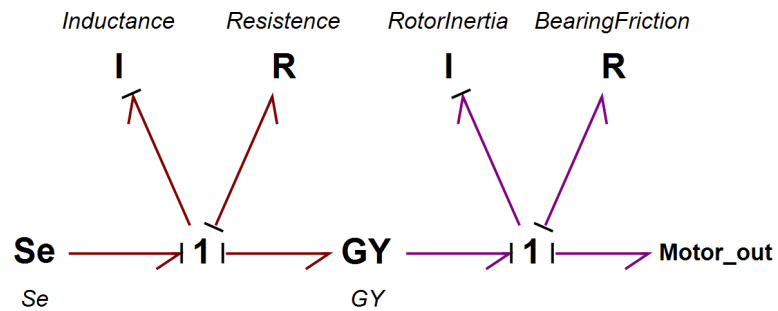
DC motor converts the electrical energy (voltage) into mechanical energy (angular velocity). In this section, the bond graph model of the DC motor will be built. Figure 4-2 (a) shows the sketch of a DC motor. It comprises inductance L_a , resistance R_a , motor constant n , rotor inertia J , bearing friction b .

In the bond graph, shown in Figure 4-2 (b), the energy is described as effort and flow.

Effort multiplied by flow produces power. In this case, voltage is the effort and current are the flow. In the 0 junction, the flow sums to zero and the efforts are equal. In the 1 junction, the efforts sum to zero and the flows are equal. Since inductance, resistance, and voltage source are in serial connection, the current is equal to both components. They are connected by 1 junction. GY component in DC motor is current to torque conversion parameter. Since the rotary friction and rotary inertia are on the same shaft, they share the same rotary velocity so that they are connected by 1 junction. The motor output is a flow output, which is the angular velocity in this case.



(a)



(b)

Figure 4-2 Bond Graph Model of DC Motor [46]

For DC motor, reference [46] derived the following transformation model. DC motor relative parameters are shown Table 4-3. The bond graph model of the DC motor is shown in Figure 4-2.

Table 4-3 DC Motor Parameters

Parameters	Quantity	Units
n (GY)	253	N. m/A
I (Inductance)	121	μH
I (Rotor Inertia)	98.6	g. cm^2
R (Resistance)	0.346	Ω
R (Bearing Friction)	3×10^{-5}	N. s/m

4.3.2. Bond Graph Modelling of Robot Arms

Karnopp and Rosenberg (1968) made multiple rigid body models, and they proposed the Eulerian Junction Structure (EJS) model [44]. Another approach, multiport model, is used in this research is to model multibody mechanical systems, which is easy to understand and implement in bond graphs, is to define a set of body-fixed coordinate, and constrain them using velocity constraint equations. If the velocity nodes in a bond graph, then the force or torque equations will be automatically satisfied. The robot arm is a rigid body and multiport model can be applied to it. A rigid arm is shown in Figure 4-3. This model is built based on each body fixed frame fixed on the arm center of mass. Through frame transformation

matrix gR_b , a point in the body frame as $\begin{bmatrix} X' \\ Y' \end{bmatrix}$ can be transformed to ground frame as

$\begin{bmatrix} X \\ Y \end{bmatrix}$. Vice versa, if the point in the ground frame needs to be transformed to body fixed

frame, then the inverse ${}^gR_b^{-1}$, or same as gR_b , should be used.

$$\begin{bmatrix} X \\ Y \end{bmatrix} = {}^gR_b \begin{bmatrix} X' \\ Y' \end{bmatrix} + \begin{bmatrix} AG \cos(\theta_i) \\ AG \sin(\theta_i) \end{bmatrix} \quad (4-3)$$

Where ${}^gR_b = \begin{bmatrix} \cos(\theta_i) & -\sin(\theta_i) \\ \sin(\theta_i) & \cos(\theta_i) \end{bmatrix}$. If the equation (4-3) is differentiated, we can get

$$\begin{bmatrix} V_{ix} \\ V_{iy} \end{bmatrix} = \begin{bmatrix} \cos(\theta_i) & -\sin(\theta_i) \\ \sin(\theta_i) & \cos(\theta_i) \end{bmatrix} \begin{bmatrix} V_{ix'} \\ V_{iy'} \end{bmatrix} + \dot{\theta}_i \begin{bmatrix} -\sin(\theta_i) & -\cos(\theta_i) \\ \cos(\theta_i) & -\sin(\theta_i) \end{bmatrix} \begin{bmatrix} X' \\ Y' \end{bmatrix} + \begin{bmatrix} -AG \sin(\theta_i) \dot{\theta}_i \\ AG \cos(\theta_i) \dot{\theta}_i \end{bmatrix} \quad (4-4)$$

When the rigid arm moves, the body frame moves. The velocity represented in body frame needs to be transformed to ground frame. Based on equation (4-4), the linear velocity can be transformed and delivered from the end-effector coordinate up to ground coordinate, where actuator locates and is fixed to the base.

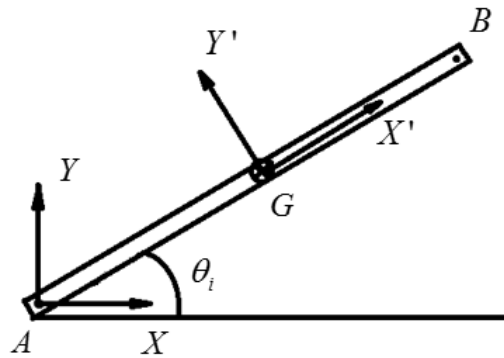


Figure 4-3 Rigid Arm

The Five-Bar workspace is planar and located in the XY plane where the influence of gravity is insignificant. So each arm mass is equally assumed to be 100 grams. Each arm is represented with an EJS model. Its rotation refers to the ground frame and it can be shown in gR_b matrix. Based on the previous introduction about the bond graph, angular velocity, and linear velocity flow. Using bond graph and the transformation equations in (4-4), the relationship between velocity and angular velocity can be built. It is a suitable method to model the planar manipulator.

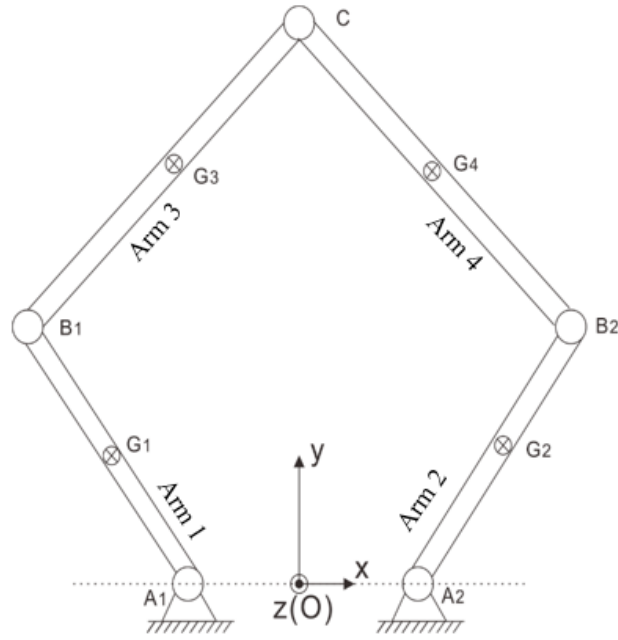


Figure 4-4 Five-Bar Sketch

As Figure 4-4, all variables reference the same base coordinate. The Z-direction is perpendicular to the XY plane and points out of the paper.

The bond graph sub-model of arm one is shown in Figure 4-5. In this model, the continuous power storage element is labeled as J_{G1} and it represents arm rotation inertia referring to the Z-axis. The variables M_{1x} and M_{1y} represent beam inertia elements standing for gravity influence. Since this mechanism workspace is in the XY plane and the arm is fixed on the motor shaft, the torque created by gravity is balanced by the support torque. We assume gravity has limited influence on the Five-Bar robot dynamic performance. So these two elements are assigned very small values. The same method is used for the other arms.

The x-direction velocity of the proximal arm on point A_1 is V_{A1x} , and V_{A1y} is the y-direction velocity of arm one on point A_1 . The x-direction velocity of arm one on point B_1 is V_{B1x} , and V_{B1y} is the y-direction velocity of arm one on point B_1 . The x-direction velocity of arm one on mass center G is V_{G1x} and V_{G1y} is the y-direction velocity of arm one on mass center G . For the adoption of symmetrical configuration, arm two A_2B_2 model can be built using the same method. Point A_1 and point A_2 are fixed on the ground, thus equations (4-6) and (4-7) both equal to zero.

In this arm one (proximal arm) sub-model, proximal arm length is assigned and velocity equations on each end are derived as,

$$A_1G_1 = B_1G_1 = \frac{L_1}{2} = \frac{L_2}{2} = 115mm \quad (4-5)$$

$$V_{A1x} = V_{G1x} + A_1G_1 \times \sin \theta_1 \times \omega_1 = 0 \quad (4-6)$$

$$V_{A1y} = V_{G1y} - A_1G_1 \times \cos \theta_1 \times \omega_1 = 0 \quad (4-7)$$

$$V_{B1x} = V_{G1x} - B_1G_1 \times \sin \theta_1 \times \omega_1 \quad (4-8)$$

$$V_{B1y} = V_{G1y} - B_1G_1 \times \cos \theta_1 \times \omega_1 \quad (4-9)$$



93

Arm three (distal arm) B_1C is modeled with the Eulerian junction structure model which is shown in Figure 4-6. In this sub-model, here V_{B1x} is the x-direction velocity of arm one on point B_1 , and V_{B1y} is the y-direction velocity of arm one on point B_1 . By sharing the same velocity at point B_1 , proximal arm model and distal arm model can be bridged. The x-direction velocity of arm one on point C is V_{cx} , and V_{cy} is the y-direction velocity of arm one on point C . The x-direction velocity of arm three on mass center G_3 is V_{G3x} , and V_{G3y} is the y-direction velocity of arm three on mass center G_3 . All these velocity variables refer to ground frame. For the adoption of symmetrical configuration, arm four B_2C model can be built with the same method.

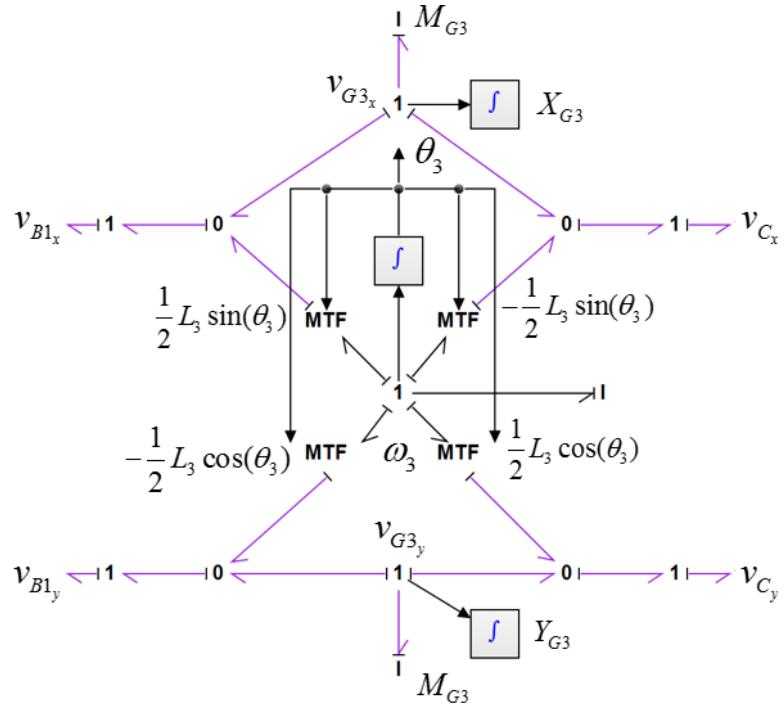
$$CG_3 = B_1G_3 = \frac{L_3}{2} = 125mm \quad (4-10)$$

$$V_{B3x} = V_{G3x} + B_1G_3 \times \sin \theta_3 \times \omega_3 \quad (4-11)$$

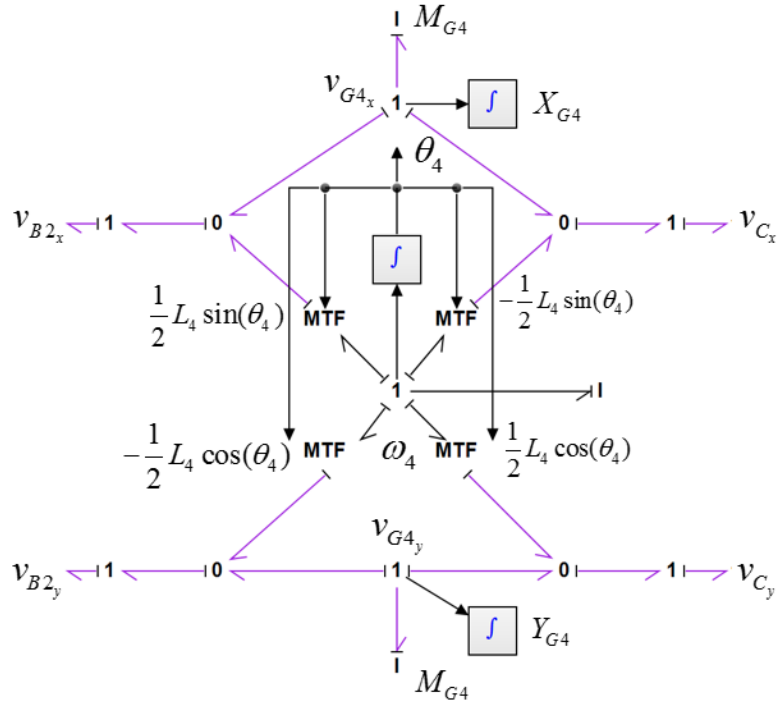
$$V_{B3y} = V_{G3y} - B_1G_3 \times \cos \theta_3 \times \omega_3 \quad (4-12)$$

$$V_{Cx} = V_{G3x} - CG_3 \times \sin \theta_3 \times \omega_3 \quad (4-13)$$

$$V_{Cy} = V_{G3y} + CG_3 \times \cos \theta_3 \times \omega_3 \quad (4-14)$$



(a) Sub-model of Arm Three



(b) Sub-model of Arm Four

Figure 4-6 Bond Graph Model of Arm Three B_1C and Arm Four B_2C

4.3.3. Bond Graph Modelling of Parasitic Element

It is relatively common to encounter derivative causality in the mechanical part of the system due to the assumption that inertia elements such as rigid bodies are connected rigidly [47].

To eliminate derivative causality, a parasitic element is built to isolate inertial components from the rest of the system. Since the integral causality of each energy-storing element is preserved, the bond graph leads to explicit differential equations, which then can be easily integrated using explicit algorithms [48].

Figure 4-7 shows the two ports parasitic element sub-model. It can be treated as a set of parallel spring and damper with large values. This method introduces high-frequency mode into the system. In this model, $R = 1 \times 10^3$ and $C = 1 \times 10^{-6}$, which represent damping and compliance. Increasing damping can improve computation times. Large damping and compliance values render the system stiffer and longer computations result. This may reach excessive values.

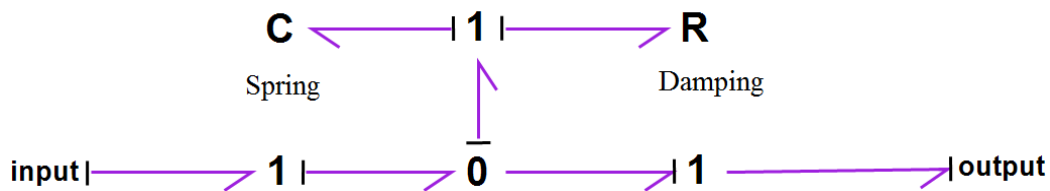


Figure 4-7 Bond Graph Model of Isolator

4.3.4. Bond Graph Modelling of the Complete Robot

As a whole robotic system, controllers are studied and the dynamic results shown in the following figure. In Figure 4-8, a comprehensive bond graph model is built in a bond graph modeling software 20-Sim. Parameters, such as arms momentum of inertia, mass, used in 20-Sim software are evaluated and created through Solidworks model.

From the bottom to the top, the Ideal x and Ideal y is the desired location for end-effector position on XY plane. Then the Ideal x and Ideal y are converted to Ideal θ_1 and Ideal θ_2 by inverse kinematics. The error between the desired angle and current angle for arm one is as input for PID controller, the same process for arm two. The PID control outputs are sent to a power source, which is limited from -24 V to 24 V. The electrical energy is converted to mechanical angular velocity. Through the isolators, in this case, they representing the rigid joints between arms, the energy is transmitted to the following arms.

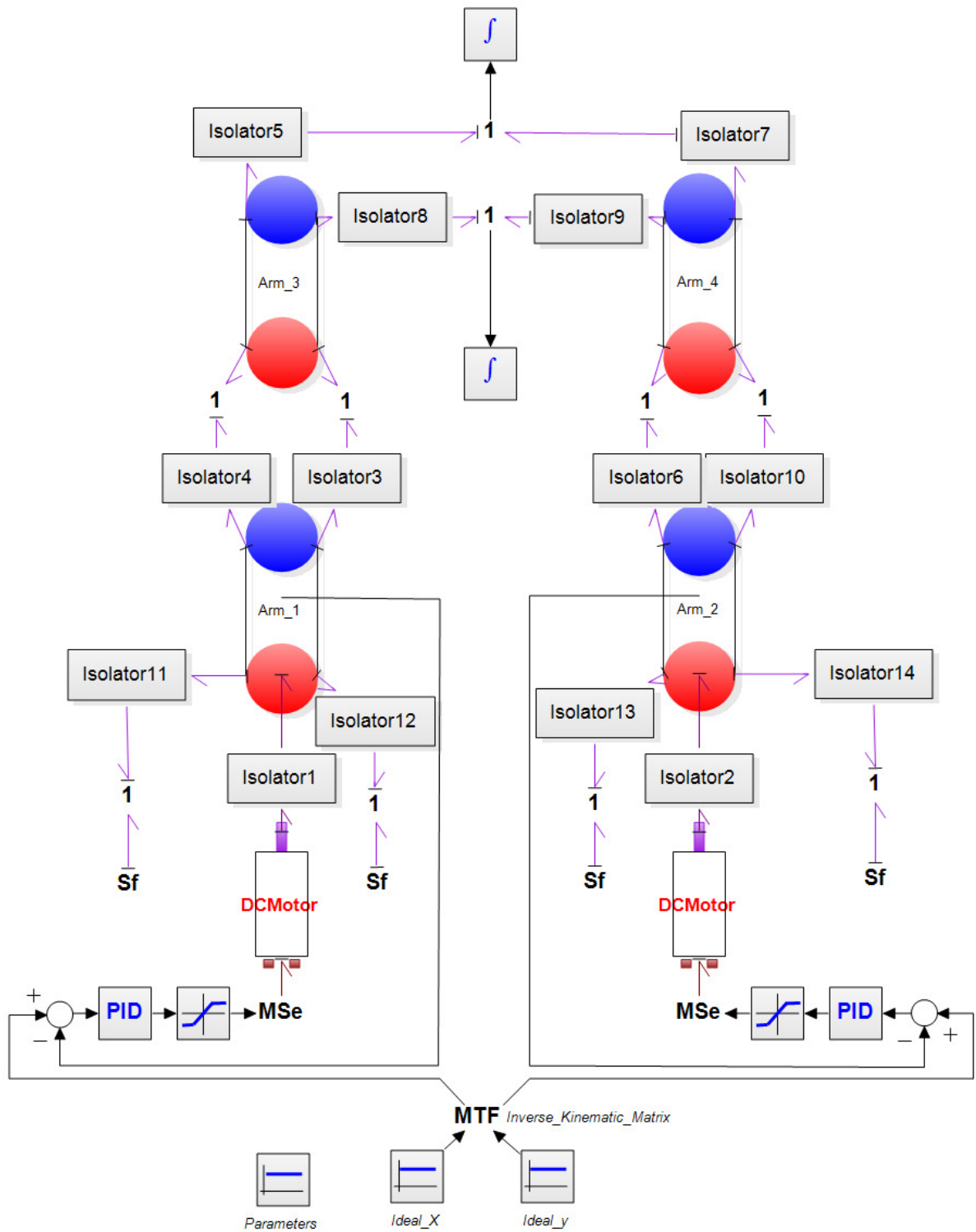


Figure 4-8 Integrated Bond Graph of a Five-Bar Parallel Robot

4.3.5. Bond Graph Modelling of the Control System

The PID control loop is named after three correcting components. The proportional, integral and derivative terms are summed to calculate the output of the PID controller. The process diagram of the PID controller in parallel form is shown in Figure 4-9. It is a popular controller researched since the 1890s and widely applied in industrial design since 1911 [63]. It is reliable and it has many alternative forms and tuning methods can be applied.

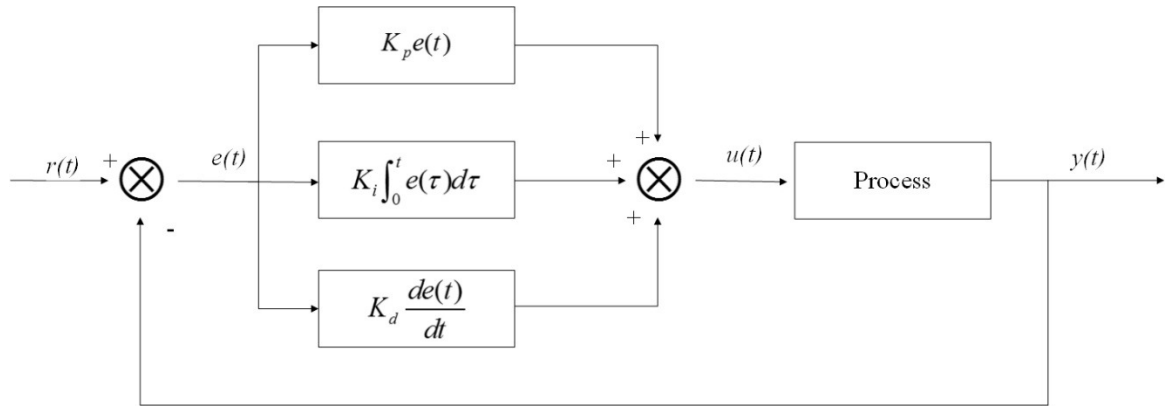


Figure 4-9 PID Controller Process Diagram

The controller output is defined as the following algorithm [63]:

$$u(t) = K_p e(t) + K_i \int_0^t e(\tau) d\tau + K_d \frac{de(t)}{dt}$$

The $e(t)$ is the error input, the difference between current desired motor angle and current motor angle feedback.

The K_p is the proportional gain parameter. A high value of K_p leads to a linear large change for a small error value. It can raise the responsiveness and sensitivity of the system but it may cause the system to be unstable if the value is too high.

The K_i is the integral gain parameter. A high value of K_i leads to the acceleration of the system towards the set point. It multiplies the accumulated error since time 0 so it can result in an overshoot.

The K_d is the derivative gain parameter. It multiplies the derivative of the error change over time. It raises the stability and noise resistance ability of the system.

τ is the integration variable and it takes on values from time 0 to current time t .

The series PID controller structure is shown in Figure 4-10. This controller also has four parameters including proportional gain K_p , derivative gain K_d , and integral gain K_i . It is a PID controller in series form and its transfer function is the following [49]. It is modified from the traditional parallel PID controller. In this model, two series PID controllers are separately implemented for each motor control.

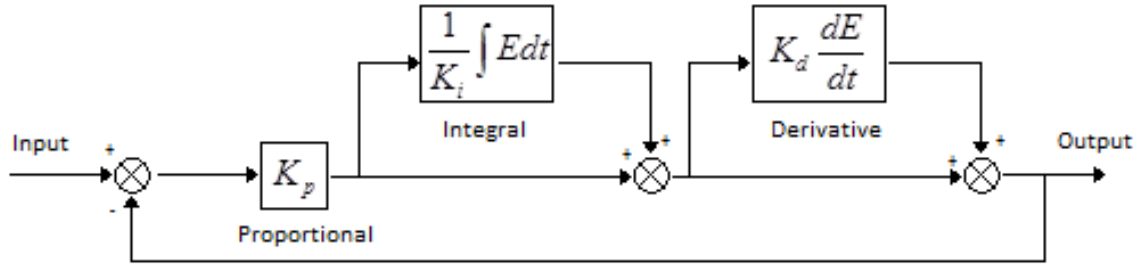


Figure 4-10 Series PID Controller

The PID controller continuously calculates an error value as the difference between the desired set point and a measured process variable [63]. The desired point in Cartesian coordinates is converted into two desired actuator angles through the inverse kinematic algorithm described in the previous section. These two desired angles are set points. The PID input signal is the error between set point angle and the real angle feedback.

$$\text{Output} = K_p \left(E + \frac{1}{K_i} \int E dt \right) \left(1 + K_d \frac{dE}{dt} \right)$$

Three control parameters K_p , K_d , and K_i can influence the control result. Trial and error method is used to tune the controller. Until the error between the desired angle and controlled angle is smaller than 5% of the difference between an initial angle and final angle.

4.4. Lagrangian Modeling

The dynamic model of Five-Bar manipulator based on reduced Lagrangian method [31]

will be presented in this section. All the parameters are matched with parameters shown in Figure 3-1. By input all known parameters into the model, it will give out the needed toques in the end.

$$\begin{bmatrix} \theta_1 \\ \theta_2 \\ \theta_3 \\ \theta_4 \end{bmatrix} = \begin{bmatrix} q_1 \\ q_2 \\ q_3 \\ q_4 \end{bmatrix} \quad (4-15)$$

$$\begin{bmatrix} \square \\ \theta_1 \\ \square \\ \theta_2 \\ \square \\ \theta_3 \\ \square \\ \theta_4 \end{bmatrix} = \begin{bmatrix} \square \\ q_1 \\ \square \\ q_2 \\ \square \\ q_3 \\ \square \\ q_4 \end{bmatrix} \quad (4-16)$$

$$a = 2L_4\lambda \quad (4-17)$$

$$b = 2L_4\mu \quad (4-18)$$

$$c = L_3^2 - L_4^2 - \mu^2 - \lambda^2 \quad (4-19)$$

$$\lambda = L_2 \cos(q_2) - L_1 \cos(q_1) + L_5 \quad (4-20)$$

$$\mu = L_2 \sin(q_2) - L_1 \sin(q_1) \quad (4-21)$$

$$q_{13} = q_1 + q_3 \quad (4-22)$$

$$q_{24} = q_2 + q_4 \quad (4-23)$$

Based on equations from (4-15) to (4-23),

$$q_3 = \tan^{-1} \left[\frac{\mu + L_4 \sin(q_{24})}{\lambda - L_4 \sin(q_{24})} \right] - q_1 \quad (4-24)$$

$$q_4 = \tan^{-1} \left[\frac{\pm \sqrt{a^2 + b^2 - c^2}}{c} \right] - \tan^{-1} \left[\frac{b}{a} \right] - q_2 \quad (4-25)$$

$$q_3 = \frac{L_1 \sin(q_{24} - q_1) q_1 + L_2 \sin(q_2 - q_{24}) q_2}{L_2 \sin(q_{13} - q_{24})} - q_1 \quad (4-26)$$

$$q_4 = \frac{L_2 \sin(q_{13} - q_2) q_2 + L_1 \sin(q_1 - q_{13}) q_1}{L_4 \sin(q_{24} - q_{13})} - q_2 \quad (4-27)$$

Based on equations from (4-24) to (4-27), we can calculate the following essential parameters.

$$\psi_{11} = -L_1 \sin(q_1) - L_3 \sin(q_1 + q_3) \quad (4-28)$$

$$\psi_{12} = L_2 \sin(q_2) + L_4 \sin(q_2 + q_4) \quad (4-29)$$

$$\psi_{13} = -L_3 \sin(q_1 + q_3) \quad (4-30)$$

$$\psi_{14} = L_4 \sin(q_2 + q_4) \quad (4-31)$$

$$\psi_{21} = L_1 \cos(q_1) + L_3 \cos(q_1 + q_3) \quad (4-32)$$

$$\psi_{22} = -L_2 \cos(q_2) - L_4 \cos(q_2 + q_4) \quad (4-33)$$

$$\psi_{23} = L_3 \cos(q_1 + q_3) \quad (4-34)$$

$$\psi_{24} = -L_4 \cos(q_2 + q_4) \quad (4-35)$$

$$\psi_{q'}(q') = \begin{bmatrix} \psi_{11} & \psi_{12} & \psi_{13} & \psi_{14} \\ \psi_{21} & \psi_{22} & \psi_{23} & \psi_{24} \\ 1 & 0 & 0 & 0 \\ 0 & 1 & 0 & 0 \end{bmatrix} \quad (4-36)$$

$$\psi_q(q', q') = \begin{bmatrix} \psi_{11} & \psi_{12} & \psi_{13} & \psi_{14} \\ \psi_{21} & \psi_{22} & \psi_{23} & \psi_{24} \\ 0 & 0 & 0 & 0 \\ 0 & 0 & 0 & 0 \end{bmatrix} \quad (4-37)$$

$$\rho(q') = \psi_{q'}^{-1}(q') \begin{bmatrix} 0 & 0 \\ 0 & 0 \\ 1 & 0 \\ 0 & 1 \end{bmatrix} \quad (4-38)$$

$$\dot{\rho}(q', q') = -\psi_{q'}^{-1}(q') \dot{\psi}_q(q', q') \rho(q') \quad (4-39)$$

The dynamic model of the Five-Bar manipulator is,

$$T = \begin{bmatrix} \tau_1 \\ \tau_2 \end{bmatrix} = D(q') \ddot{q} + C(q', \dot{q}') \dot{q} + G(q') \quad (4-40)$$

Where τ_1 and τ_2 are the torque applied on the two active joints fixed on base. Since the research is focusing on the Five-Bar planar manipulator, the gravity will not be considered. So the simplified model will be,

$$T = \begin{bmatrix} \tau_1 \\ \tau_2 \end{bmatrix} = D(q') \ddot{q} + C(q', \dot{q}') \dot{q} \quad (4-41)$$

$$D(q') = \rho(q')^T D'(q') \rho(q') \quad (4-42)$$

$$C(q', \dot{q}') = \rho(q')^T C'(q', \dot{q}') \rho(q') + \rho(q')^T D'(q') \dot{\rho}(q', \dot{q}') \quad (4-43)$$

$D'(q')$ is the inertia matrix and $C'(q', \dot{q}')$ is the centrifugal and Coriolis terms matrix,

which are defined as follows:

$$D(q') = \begin{bmatrix} d_{11} & 0 & d_{13} & 0 \\ 0 & d_{22} & 0 & d_{24} \\ d_{31} & 0 & d_{33} & 0 \\ 0 & d_{42} & 0 & d_{44} \end{bmatrix} \quad (4-44)$$

$$C'(q', q') = \begin{bmatrix} h_1 q_3 & 0 & h_1(q_1 + q_3) & 0 \\ 0 & h_2 q_4 & 0 & h_2(q_2 + q_4) \\ -h_1 q_1 & 0 & 0 & 0 \\ 0 & -h_2 q_2 & 0 & 0 \end{bmatrix} \quad (4-45)$$

$r_i = \frac{L_i}{2}$ ($i = 1, 2, 3, 4$) represents the mass center of the each arm. I_i ($i = 1, 2, 3, 4$)

represents the inertia of each arm and m_i ($i = 1, 2, 3, 4$) represents the mass of each arm:

$$d_{11} = m_1 r_1^2 + m_3 (L_1^2 + r_3^2 + 2L_1 r_3 \cos(q_3)) + I_1 + I_3 \quad (4-46)$$

$$d_{13} = d_{31} = m_3 (r_3^2 + L_1 r_3 \cos(q_3)) + I_3 \quad (4-47)$$

$$d_{22} = m_2 r_2^2 + m_4 (L_2^2 + r_4^2 + 2L_2 r_4 \cos(q_4)) + I_2 + I_4 \quad (4-48)$$

$$d_{24} = d_{42} = m_4 (r_4^2 + L_2 r_4 \cos(q_4)) + I_4 \quad (4-49)$$

$$d_{33} = m_3 r_3^2 + I_3 \quad (4-50)$$

$$d_{44} = m_4 r_4^2 + I_4 \quad (4-51)$$

$$h_1 = -m_3 L_1 r_3 \sin(q_3) \quad (4-52)$$

$$h_2 = -m_4 L_2 r_4 \sin(q_4) \quad (4-53)$$

4.5. Bond Graph and Lagrangian Results Comparison

By applying equations from (4-15) to (4-53), the dynamic model of the Five-Bar manipulator can be built. In order to compare the Bond-Graph method and traditional Lagrangian method, a trajectory will be assumed within the workspace. The bond graph model and Lagrangian model will perform the same trajectory to validate the Bond-Graph modelling.

The input angles are shown as (4-54) and (4-55).

$$\theta_1 = 112.5^\circ - 22.5^\circ \cos(\pi t) \quad (4-54)$$

$$\theta_2 = 67.5^\circ + 22.5^\circ \cos(\pi t) \quad (4-55)$$

The trajectory within workspace is shown in Figure 4-11. Based on the input angles, the end-effector will move back and forth along the Y axis. The position results of the end-effector from the Lagrangian model and Bond-Graph model are shown in Figure 4-12.

The input angles and related angular velocities are shown and compared in Figure 4-13.

Finally, the input torques are shown and compared in Figure 4-14.

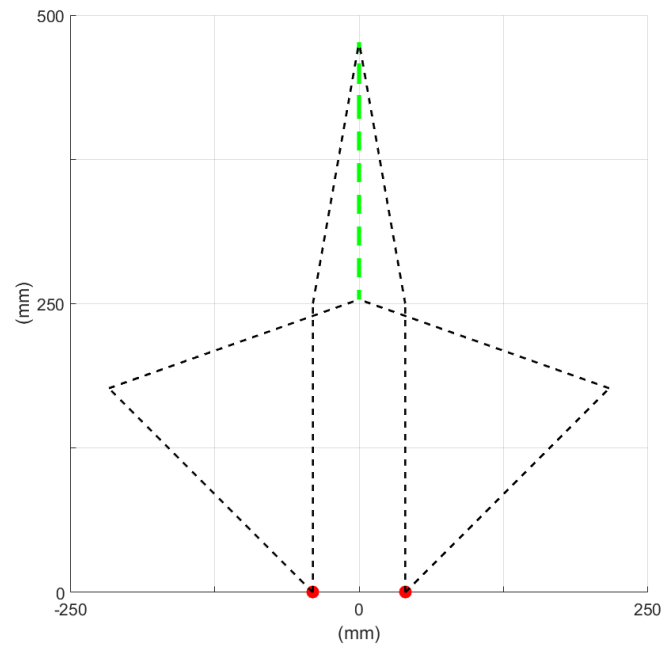


Figure 4-11 Validation Trajectory

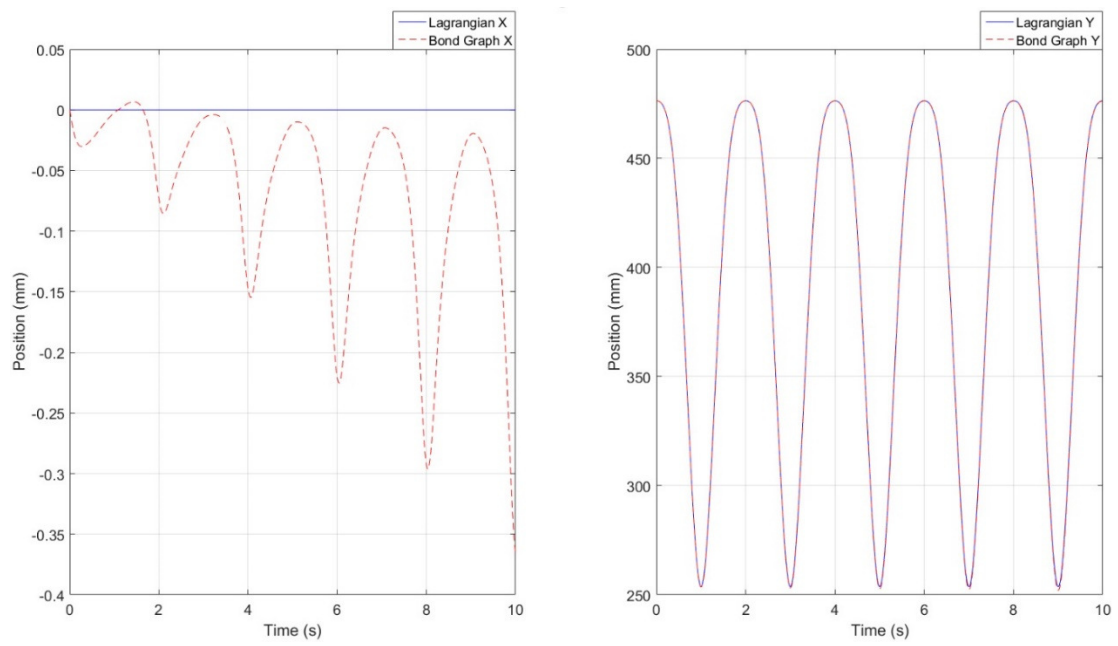


Figure 4-12 Trajectory Position Comparison

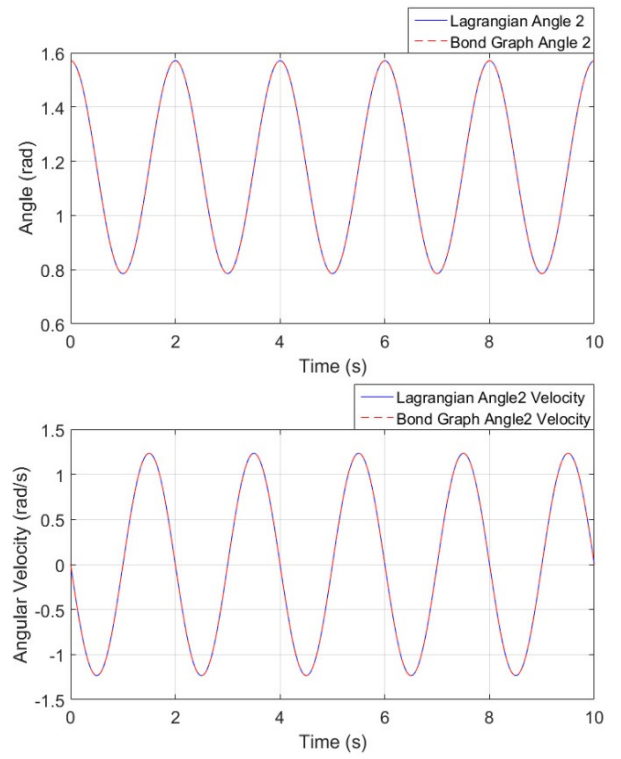
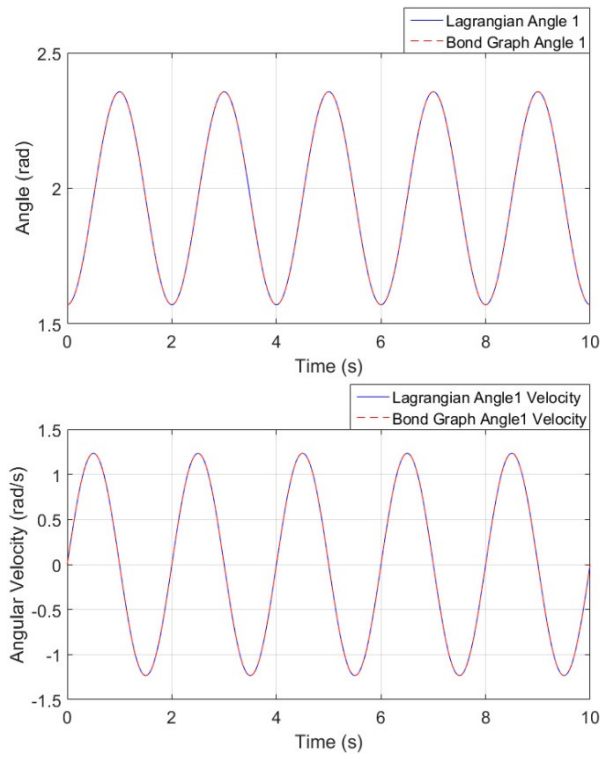


Figure 4-13 Angles and Angular Velocities Comparison

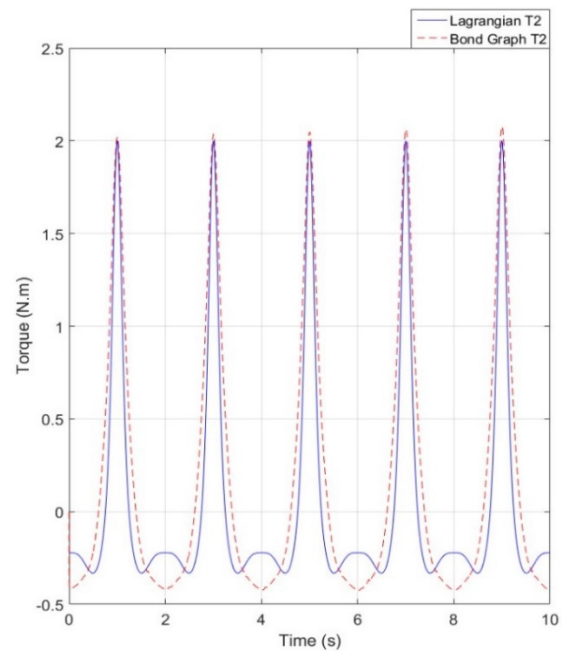
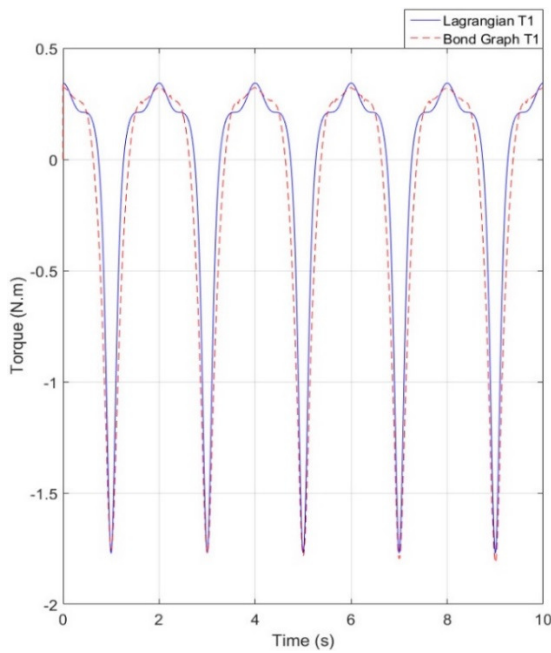


Figure 4-14 Torques Comparison

Based on the comparison results from the two dynamic modeling methods, the errors between Bond-Graph model and Lagrangian model are in reasonable scale. In Figure 4-12, the X position results maximum error is less than 0.5 mm comparing to 250 mm moving distance back and forth; the Y position results matches perfectly. From Figure 4-13 we can find angle one, angle two, angular velocity one and angular velocity two all matches perfectly. Finally in Figure 4-14, the positive or negative value means the torque direction and the maximum absolute value is the maximum net torque. The maximum net torque one from Lagrangian is 1.74 N.m while bond graph yields 1.80 N.m; the maximum net torque two from Lagrangian is 2 N.m while bond graph yields 2.07 N.m. The errors are both less than 5%. After all, we conclude bond graph is a valid modeling method for five-bar manipulator dynamic analysis.

The equations are derived and the calculations are done by software. The user does less calculation, but the computer implementation of bond graphs does not reduce calculations or equations compared to any other method.

4.6. Bond Graph Simulation Results

In this section, bond graph simulation results are shown. The properties of the Five-Bar robot should be assigned. Referenced to the Z axis, the principal moment of inertia for each arm is shown in Table 4-4. These four parameters are determined by the dimension and

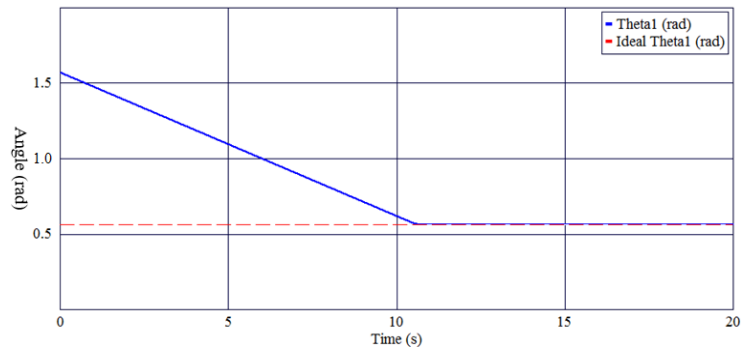
mass of the arm. Torque is the result of the inertia times the angular acceleration.

Table 4-4 Principle Moment of Inertia for Each Arm

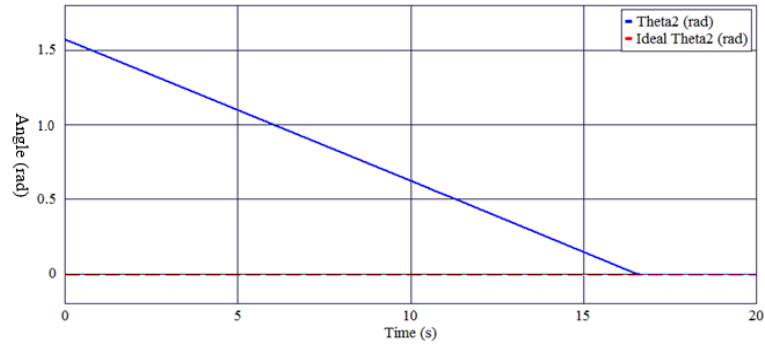
Arm	Principle Moment of Inertia	Unit
#1 (Proximal)	0.01335	$kg \cdot m^2$
#2 (Proximal)	0.01345	$kg \cdot m^2$
#3 (Distal)	0.01301	$kg \cdot m^2$
#4 (Distal)	0.01298	$kg \cdot m^2$

In the simulation, a point to point experiment is proposed. The typical point to point process needs two inputs, the desired X position and the desired Y-position (if this desired position is reachable in minus-plus configuration workspace). Then the algorithm can automatically calculate out all parameters and variables. Motors will move the manipulator to bring the end-effector towards any position set-point.

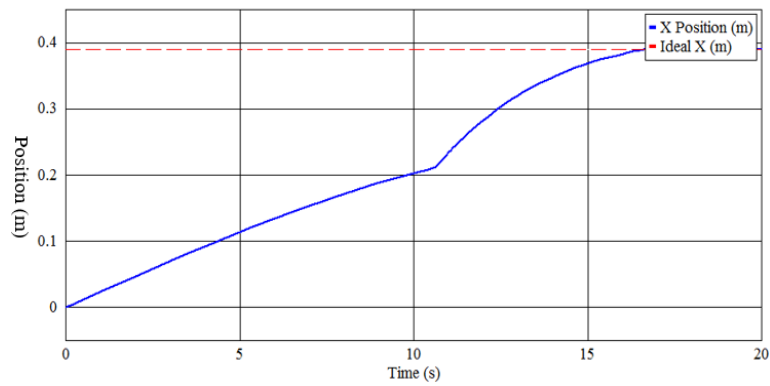
In this section, by using the bond graph model of the complete manipulator with PID controller, we will set the desired point (0.390 m, 0.205 m) for end-effector and it will be driven from the initial point (0 m, 0.477 m) where motor one and motor two are both located at 90° . The control results for motor angles and end-effector position during this process will be shown. The motor torques and torques applied on each arm during this process will be presented as well.



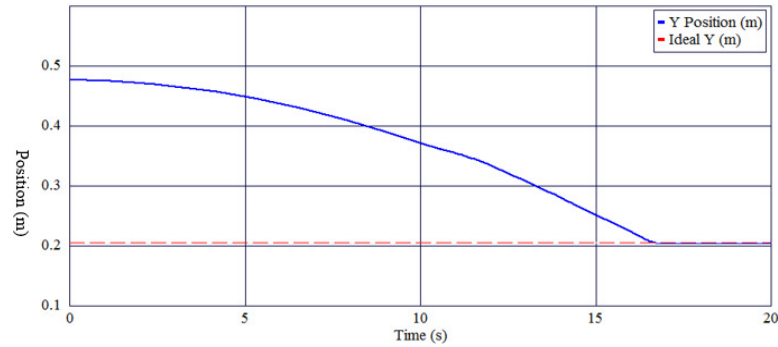
(a) Theta 1 and Desired Theta 1



(b) Theta 2 and Desired Theta 2



(c) End-effector X Position and Ideal X



(d) End-effector Y Position and Ideal Y

Figure 4-15 Angles and Positions Controlled Results

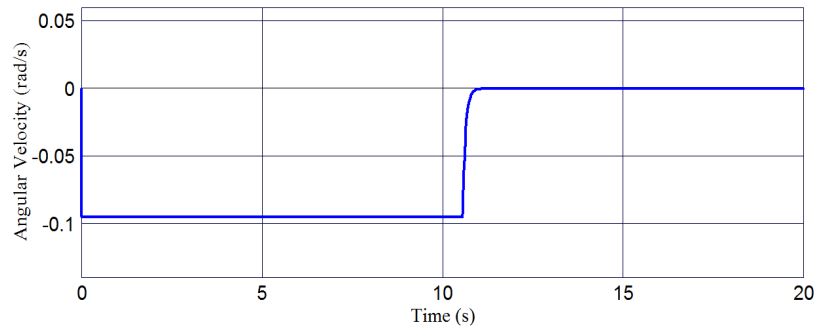
Table 4-5 Angles and Positions Controlled Results

	Theta 1 (rad)	Theta 2 (rad)	X Position (m)	Y Position (m)
Initial	1.5708	1.5708	0	0.4765
Final	0.5621	0.0106	0.3900	0.2043
Desired	0.5629	0.0084	0.3902	0.2050
Difference (Absolute)	0.0008	0.0022	0.0002	0.0007
Errors	0.079%	0.141%	0.051%	0.258%

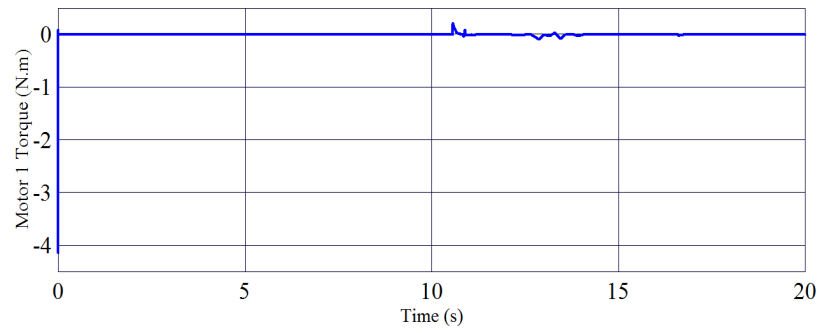
Control error is calculated as $\text{Error} = \frac{|\text{Desired-Final}|}{|\text{Desired-Initial}|} \times 100\%$. If the error is smaller than

5%, we consider the control accuracy is good.

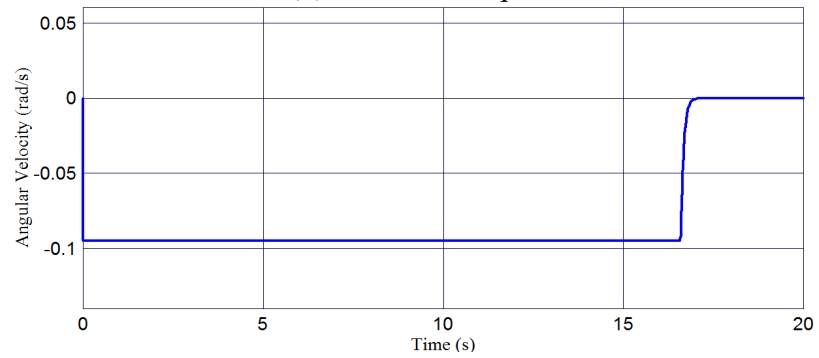
During the process of moving from initial point to the desired point, the motor torque and angular velocity output change are shown in Figure 4-16 and Table 4-6; these are important criteria for robot design. The motor output angular velocity during the process is shown in Figure 4-16(a) and Figure 4-16(c). From the plot, we can see the sudden accelerate from idle status to a constant speed at the start. It means a high torque is needed for acceleration. Referring to Figure 4-16(b) and Figure 4-16(d), this sudden torque is called ‘starting torque’. Its negative or positive signs assign the direction of the torque and angular velocity. Only the absolute value of them are good for us to choose the motor. As the motor output is in constant angular velocity, the angular acceleration is zero, then the motor torque drops to almost zero. Starting torque is no more than 5 N.m, which is available for the motor in the real world. This is the criteria for us to choose the motor.



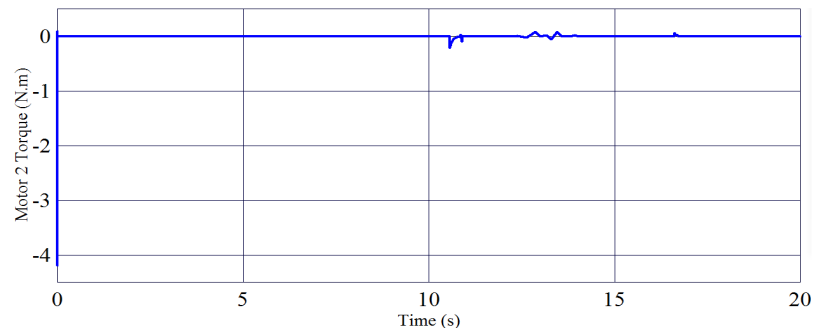
(a) Motor 1 Angular Velocity



(b) Motor 1 Torque



(c) Motor 2 Angular Velocity



(d) Motor 2 Torque

Figure 4-16 Motors Torque and Angular Velocity

Table 4-6 Motors Maximum Net Torque and Angular Velocity

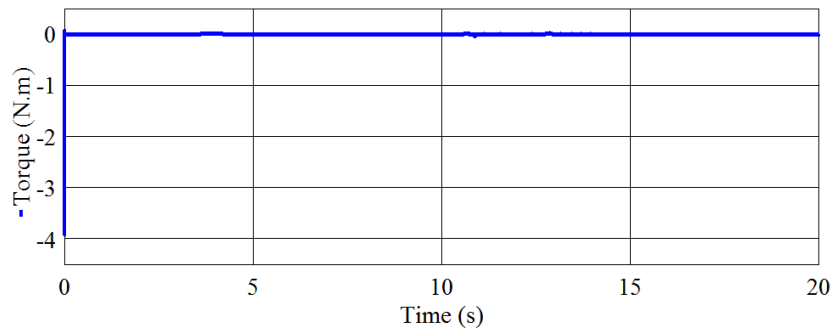
	Max. Torque (N.m)	Max. Angular Velocity ω (rad/s)
First Motor	4.1385	0.0950
Second Motor	4.1970	0.0951

At initial transients, the curve is not smooth. It steps up in a very short time then drop down in a very short time as well. This phenomenon is caused by motor starting torque. Only the absolute value is important for this research instead of the change trend or time gap.

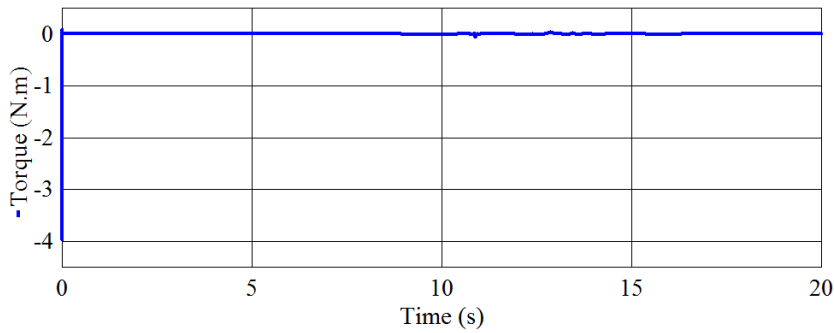
In Figure 4-17 and Table 4-7 , the torque applied on each arm rigid body during the process are provided.

In field application, these plot results can be used to analyze the material properties and mechanical design. The material should bear the maximum net torque applied on the arm. This will give a theoretical requirement for design stage, which is fulfilled in the following chapter.

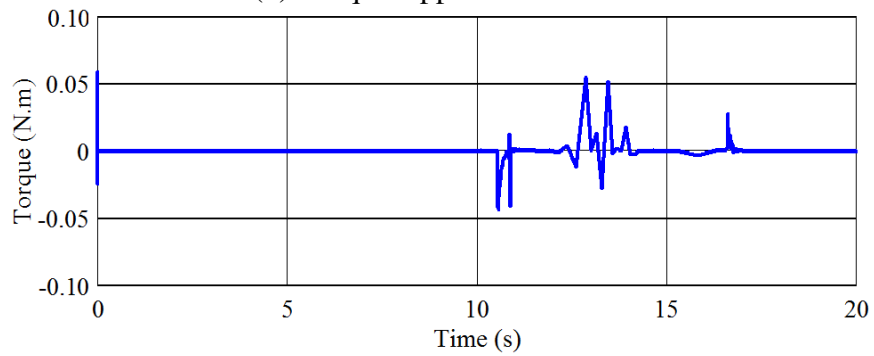
Same as the previous discussion, the negative sign and positive sign of the torques mean the torque direction. The net torque is the absolute value of the torque. Torque is the result of the inertia multiplies angular acceleration. At the start, the arm is accelerated from idle status to a constant angular velocity. It needs a relatively large torque at start. Once the arm is rotating at a constant angular velocity, the torque will drop to almost zero.



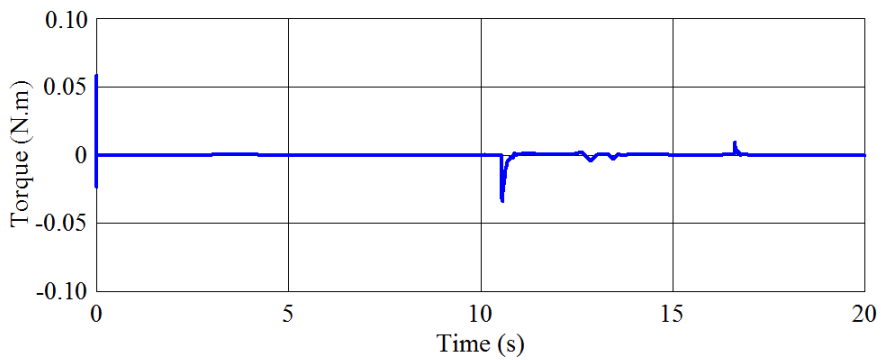
(a) Torque Applied on Arm 1



(b) Torque Applied on Arm 2



(c) Torque Applied on Arm 3



(d) Torque Applied on Arm 4

Figure 4-17 Toques Applied on Arms

Table 4-7 Maximum Net Torques Applied on Arms

	Max. Torque (N.m)
#1 (Proximal Arm)	3.912
#2 (Proximal Arm)	3.971
#3 (Distal Arm)	0.060
#4 (Distal Arm)	0.059

In order to verify displacement, a 3D animation was used to directly verify the whole process in software 20-Sim. The end-effector can successfully reach desired point (0.390 m, 0.205 m) driven from the initial point (0 m, 0.477 m). In Figure 4-18, it shows the process from 0 s to 20 s. It matches the previous simulation results and it is a more direct way to verify and confirm the model is valid for the five-bar manipulator.

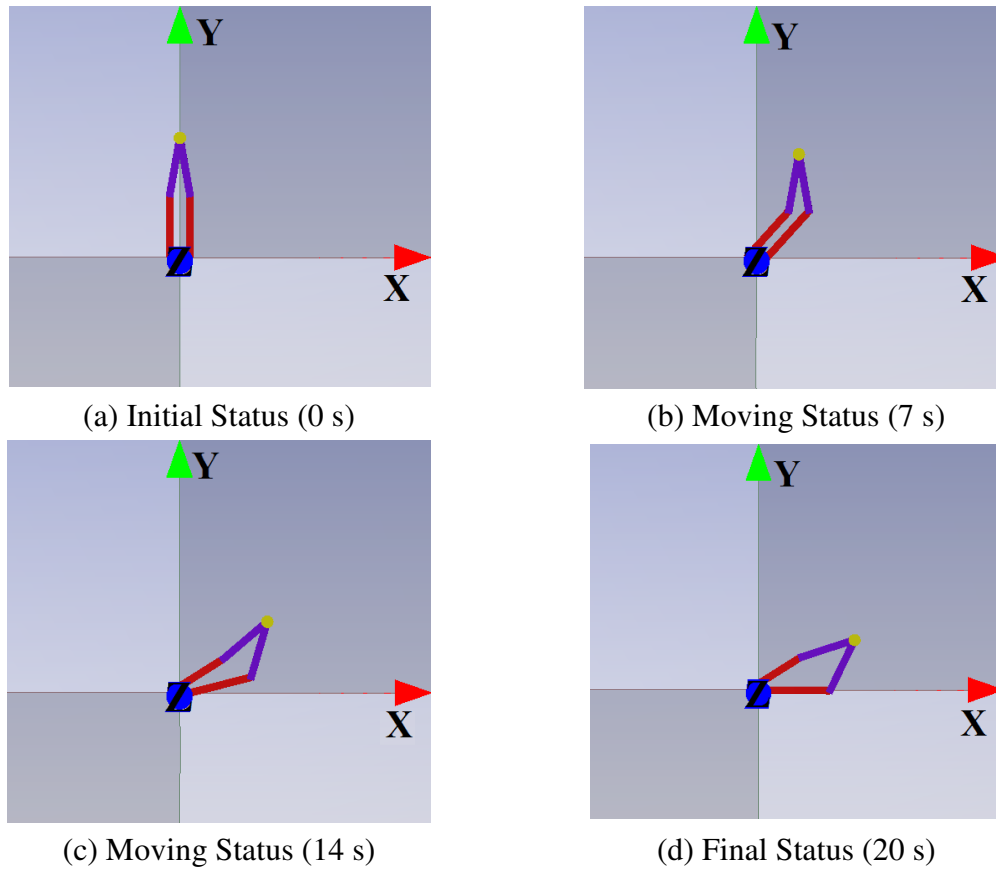


Figure 4-18 3D Animation Moving Process

Overall, based on the results we calculated above, we proved that even though bond graph is a relatively new method than traditional Lagrangian approach, it's still a valid method to fulfill dynamic analysis. PID controller is proved to be an effective controller for the five-bar manipulator. The inverse kinematic algorithm is also proved during the manipulator motion simulation Furthermore, the two motors output torques should be both greater than 5 N.m.

Chapter 5

5. Hardware Design

In this chapter, the design of the Five-Bar robot is presented in detail. The hardware design is divided into two parts: mechanical design and electrical system design.

5.1. Mechanical Design

The solid mechanical manipulator or structure was designed in Solidworks. In order to keep the design consistency, mechanical parts for Five-Bar robot are designed, drawn and analyzed utilizing Solidworks.

On account of using Windows OLE (Object Linking and Embedding) technology, advanced Parasolid kernel and good third-party software supporting technology, Solidworks is a good CAD (Computer Aided Design) software. It has been widely used in different design field such as aerospace, automotive, mechanical and everyday customer products. Memorial University has an academic license for Solidworks.

The mechanical design constraints are obtained from previous chapters,

- The auto-sampler will be located in the laboratory environment using oil and gas, so the manipulator material selection requires that the material not reacts and dissolve

with lab chemicals.

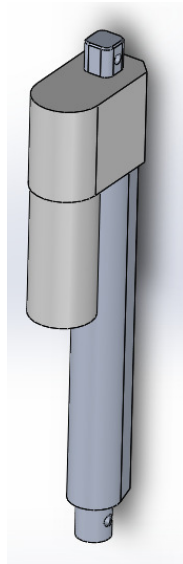
- The dimension of the auto-sampler size is limited within 1.22 m (L) \times 0.92 m (W) \times 1.00 m (H)
- The five-bar manipulator is symmetric where proximal arms $L_1 = L_2 = 230 \text{ mm}$ and distal arms $L_3 = L_4 = 250 \text{ mm}$.
- The motor net torque is greater than 5 N.m.
- The payload is the maximum weight of the end-effector that can be installed on the robot. It is an important specification to evaluate the performance of the robot.

End-effector is fixed on linear apparatus. The linear apparatus locates at the intersection point of two distal arms. The total weight on that point should be less than 2 kg.
- The end-effector should be able to connect 1/8 NPT Tube Fitting.
- The two needles should be both made by 1/16 stainless steel tube. Because 1/32 needle will be bent while piercing the septum and 1/8 is too big for small test tube inner diameter.

5.1.1. Linear Apparatus Design

The linear apparatus is controlled by the controller independently. This means adding a vertical axis on the end-effector and it will accomplish ascending and descending end-effector after the desired point reached. A simple linear actuator can achieve it.

The model P5H-24-150 manufactured by SINOKOKO is good for this task. It is made of aluminum alloy and coil voltage is 24V DC (Direct Current). The stroke length is 150 mm and the maximum speed is 29 mm/s. The peak force is 350 N. The linear actuator is shown in Figure 5-1. The reason of choosing this linear actuator is because of its low cost within \$100 CAD and 150 mm extend length is the only option to limit the auto-sampler height to 1.0 meter, which is the dimension constraint mentioned in previous section.



(a) Linear Actuator

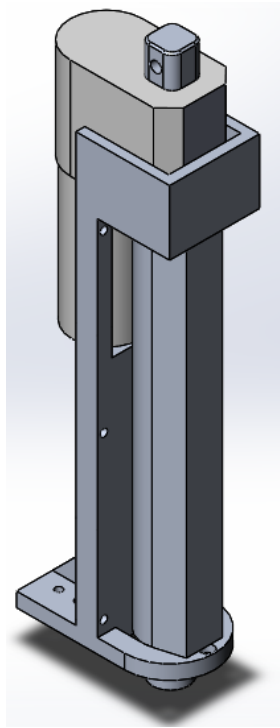


(b) Weight of Linear Actuator

Figure 5-1 SINOKOKO P5H-24-150 Linear Actuator

The detailed linear actuator characteristics and dimension are provided by SINOKOKO [50]. In order to stabilize the linear actuator, an actuator rack is designed to fix it at the intersection point of two distal arms. It is shown in Figure 5-2. The linear apparatus mass is 382.4 grams. Its detailed dimension is shown in the linear apparatus drawing, which is

shown in the appendix.



(a) Linear Actuator in Supporting Rack



(b) Weight of Supporting Rack

Figure 5-2 Linear Apparatus

5.1.2. End-Effector Design

Injection and extraction needles, installed on the end-effector, are made of sharpened 1/16 stainless steel 304 metal flow tube for constraint mentioned above. Its outer diameter is 1.59 mm, and its inner diameter is 0.76 mm. The end-effector is driven by a linear actuator along the Z axis direction.

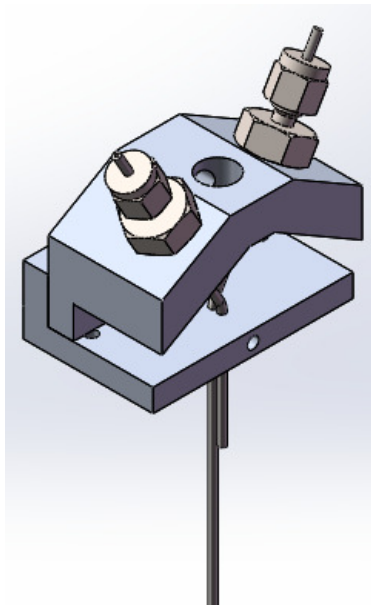
Since the small test tube inner diameter is only 7.50 mm, the two needles need to be located

very close to each other. The two needles are both sharpened to pierce the septum. The piercing experiment will be shown in the following section.

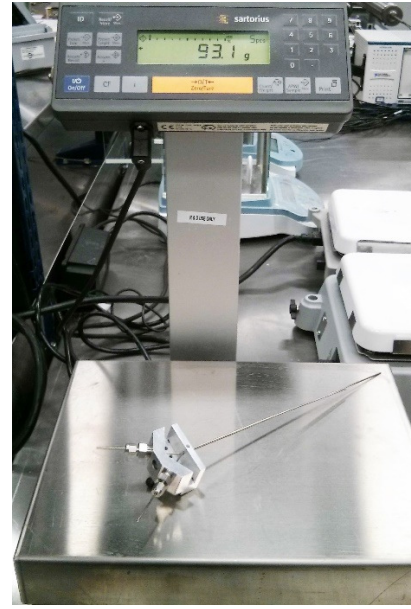
According to the sampling task requirements, the end-effector should tightly fix two 1.5875 mm diameter hollow needles and two matching Swagelok 1/8 NPT (National Pipe Thread) tube fittings.

Since the payload of the robot is constant and limited as 2kg, the manufacturing material should be light and strong. The material should not dissolve in oil and gas. So the end-effector is made of aluminum alloy 6061. The design is shown in Figure 5-3. The end-effector is designed in two parts and they are connected by four screws. The total mass for assembled end effector is 93 grams. The detailed dimensions are shown in the drawings, which are attached in the following appendix.

Based on the measurement, the total weight of linear actuator, linear actuator rack and end-effector is 1.44 kg, which satisfies the 2 kg limited payload constraint.



(a)



(b)

Figure 5-3 End-Effector Design

5.1.3. Motors

As calculated in the previous dynamic simulation, the model of 3257G024CR graphite commutation motor manufactured by FAULHABER was chosen. The nominal voltage is 24V DC with 83.2 W output power. The maximum speed is up to 7000 rpm. The mass of the motor is 242 g.

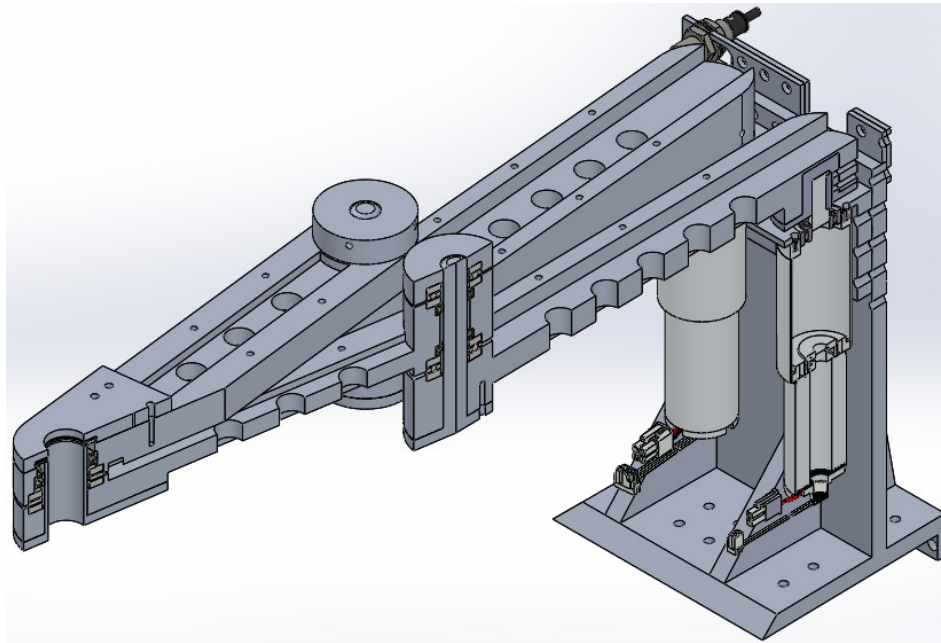
The motor uses the 38A planetary gearbox with 200:1 reduction rate. The maximum continuous output torque is 18 N.m and the intermittent torque is up to 29 N.m, which satisfies the torque constraint calculated in the previous chapter as 5 N.m. The net weight of the gearbox is 330 g. Backlash is motion lost in a mechanism caused by gaps between the

parts. The potential gearheads available on the market are spur gearhead and planetary gearhead. The spur gearhead is well-known for zero backlash but has a low output torque. The planetary gearhead is well-known for having a large output torque with relatively high backlash. An up to date, high-class planetary gearhead usually has less than 1° backlash. For this three gear-stage gearhead, it possesses only less than 0.6° backlash. In the end, spur gearhead cannot reach 5 N.m requirement and the planetary gearhead is our final and only choice under \$2000 CAD.

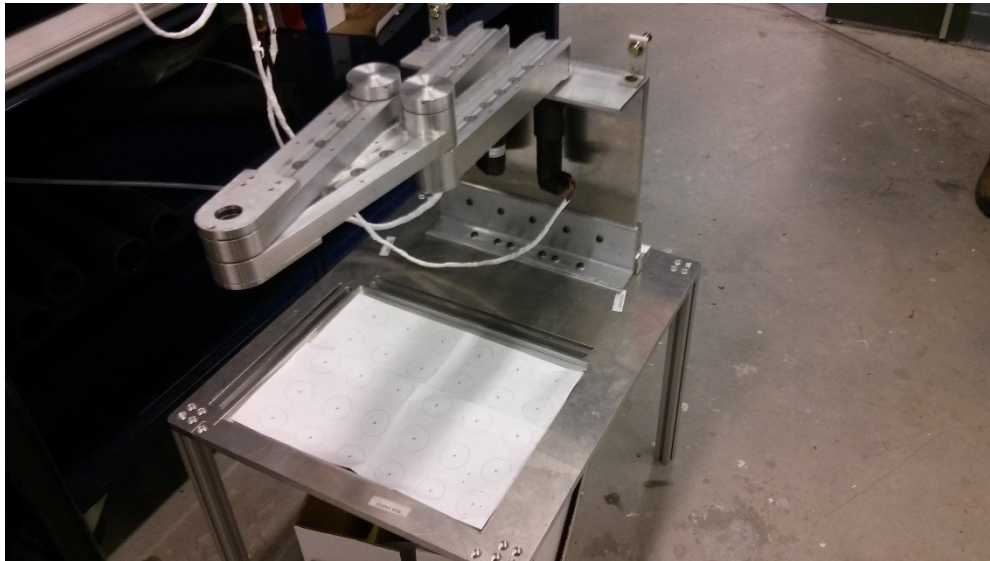
5.1.4. Manipulator Design

The five-bar manipulator design is fulfilled in this section. The constraints for this design is shown in the previous section. Then for the bearing selection, the SKF rating life equation, raised by SKF Group, is used [51]. It will calculate the force applied on bearing caused by the motor driven. By comparing this force with the bearing specification to decide whether it is feasible for our design.

Based on previous kinematics analysis, the proximal arm length is 230 mm and the distal arm length is 250 mm. The motor offset is chosen as 80 mm. A few straight holes are drilled on the arms for weight relief and tube wiring convenience. The machine design and real image are shown in Figure 5-4.



(a) Solidworks Model of Five-Bar Manipulator



(b) Fabricated Five-Bar Manipulator

Figure 5-4 Parallel Machine Design

The bearing life is calculated using the following SKF equations,

$$C_{req} = C_{10} = K_a F_e \left(\frac{L}{K_r} \right)^{\frac{1}{a}} \quad (5-1)$$

Since the gearbox's continuous torque is 18 N.m and the proximal arm length is 230 mm.

So the radial effective force can be calculated as,

$$F_e = \frac{18}{0.23} = 78 N = 17.6 \text{ lbf} \quad (5-2)$$

The defined desired life (cycles) is,

$$N = 100 \times 10^6 \quad (5-3)$$

The reliability is set as,

$$K_r = 90\% \quad (5-4)$$

The factor L equation is,

$$L = \frac{N}{10^6} \quad (5-5)$$

For the ball bearing and it is the outer ring for the shaft

$$a = 3 \quad (5-6)$$

$$K_a = 1 \quad (5-7)$$

The basic dynamic load rating can be calculated, using the known parameters, as,

$$C_{req} = C_{10} = 1 \times 17.6 \times \left(\frac{100}{0.9} \right)^{\frac{1}{3}} = 84.6 \text{ lbf} = 376.3 N \quad (5-8)$$

The shaft diameter should match with the bearing inner diameter and the bearing outer diameter should match the holding hole. So the bearing inner diameter is 15 mm and the outer diameter is 24 mm. Based on these requirements, 6802 double sealed ball bearing manufactured by NSK was chosen. Its specifications are shown as following.

Table 5-1 6802 Double Sealed by NSK Ball Bearing Specifications

Boundary Dimensions (mm)				Basic Load (N)		Factor	Limiting Speeds (rpm)	
d	D	B	r_{\min}	C_r	C_{10}	f_0	Grease	Oil
15	24	5	0.3	2070	1260	15.8	2800	3400

The dimensions of each arm were chosen after a static simulation in Solidworks. The simulation result for the proximal arm and the shaft are shown in Figure 5-5 and Figure 5-6. The external load for the arm is 100 N, which is larger than the total weight of the auto-sampler as 8 kg. The external load for the shaft is 30 N, which is larger than the total weight of the end-effector and linear actuator. Under these loading conditions, the maximum vertical displacement of the arm is 0.1275 mm and the maximum radial displacement of the shaft is 0.0188 mm.

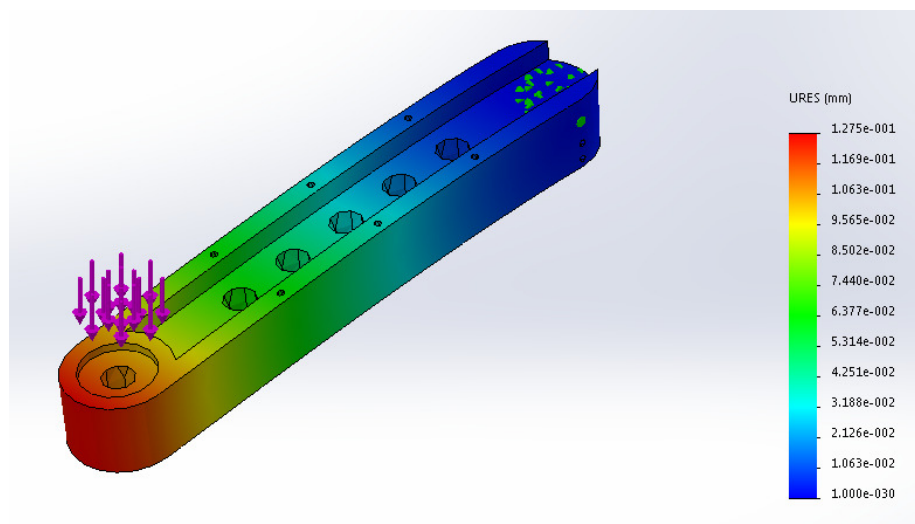


Figure 5-5 Static Analysis of Arm

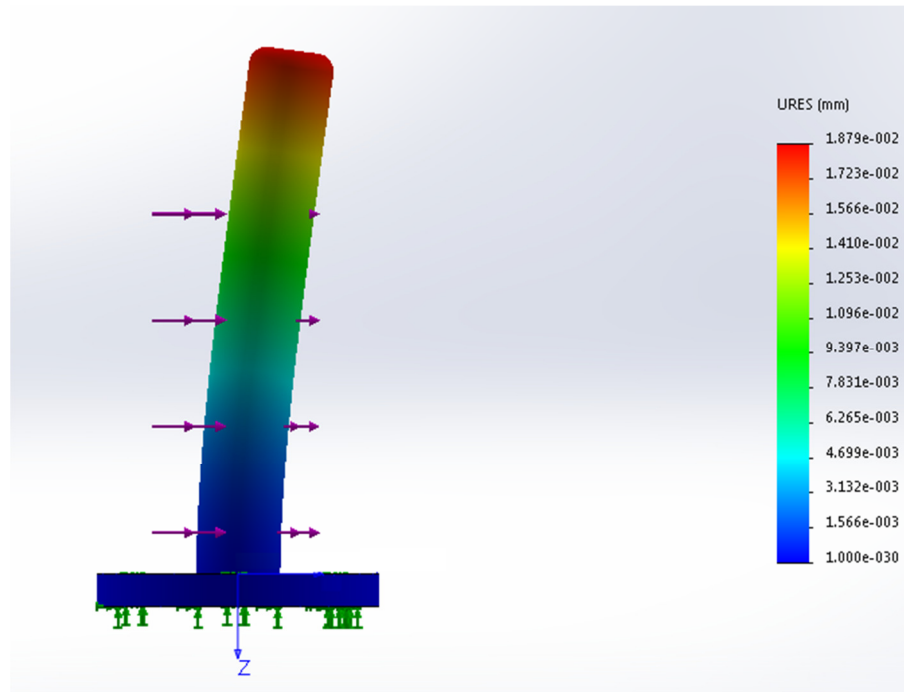


Figure 5-6 Static Analysis of Shaft

5.1.5. Piercing Force Test

The piercing force experiment is conducted using an Instron 5585H floor model testing system to perform tensile and compression tests, which is shown in Figure 5-7. It is a universal static testing system. By fixing the end-effector on the machine tool head and the test tube on the machine base platform, the tool head will drive down injecting the needle into the test tube through the septum and extract needles out afterward. The required force for injection and extraction actions are calculated and reported in Bluehill software.



Figure 5-7 Instron 5585H

By using Instron 5585H and its relative control and its supporting analysis software Bluehill, the force changing during the injection and extraction process will be recorded and plotted on the monitor.

First of all, the experiment object test tube with rubber membrane should be located and fixed on the slot table.

Secondly, the end-effector installed with injection and extraction needle should be installed on the grip, which is shown in Figure 5-8.

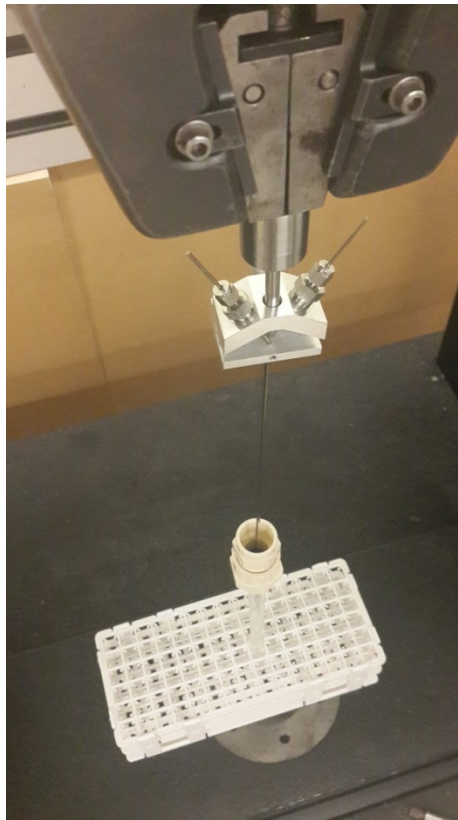


Figure 5-8 Injection and Extraction Experiment

Next, the Bulehill was used to slowly descend the load cell along the load frame. Once the needle almost but hadn't touched the membrane, stop the machine and relocate the test tube to the center of the needles, shown in Figure 5-9, to make sure the needles are in the center of the test tube before injection.

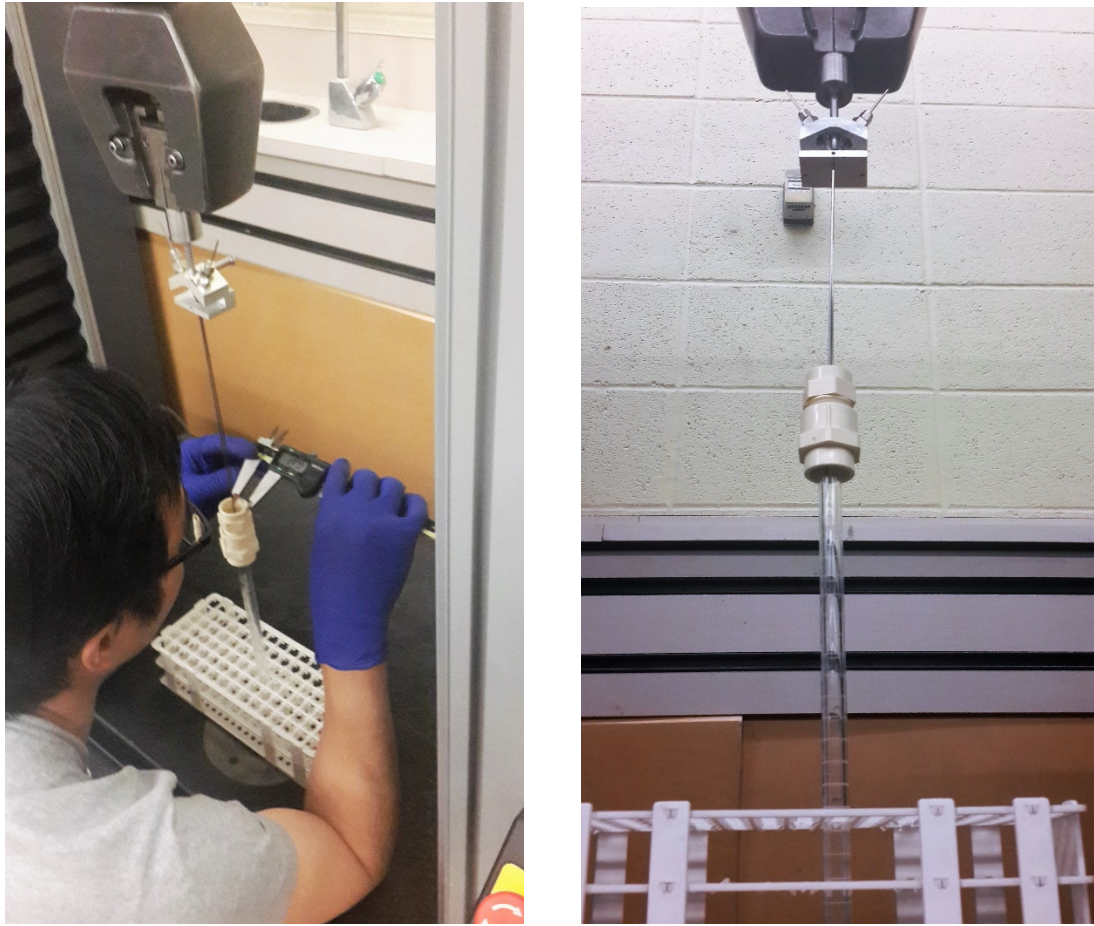


Figure 5-9 Relocate Experiment Object

Once two needles pierced through the membrane, the machine was stopped and the load frame direction was reversed to ascending until two needles were entirely extracted out of the test tube. Shown in Figure 5-10.

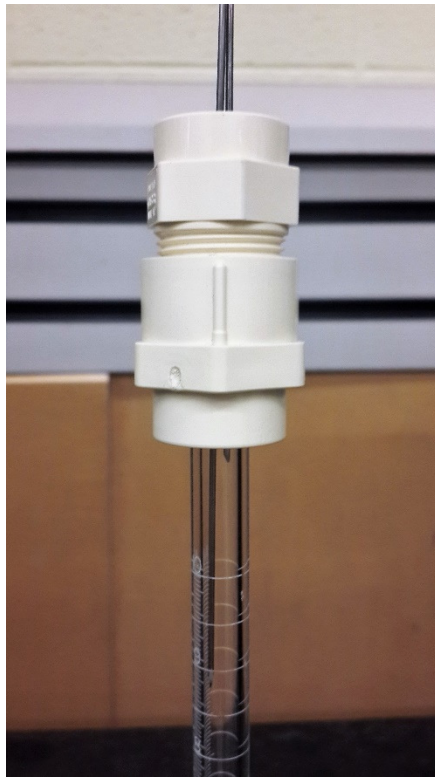


Figure 5-10 Injection and Extraction of Needles into Test Tube

In the end, the experiment is complete and the result can be obtained through the Bluehill software. The experiment result is shown in Figure 5-11. The result indicates that the required maximum injection force is less than 5 N and the required maximum extraction force is less than 10 N. In this design mentioned previously, the P5H 24V DC linear actuator manufactured by SINOKOKO with maximum 350 N meets this requirement.

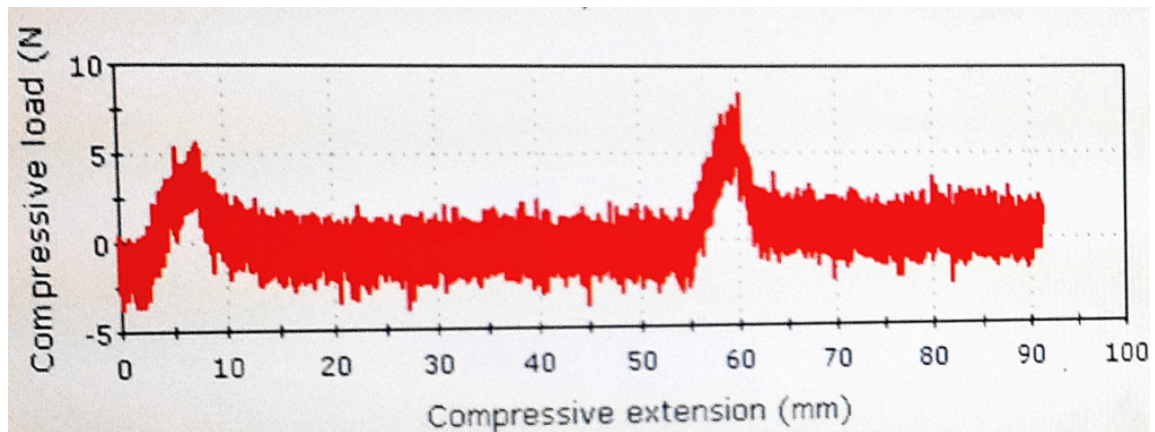


Figure 5-11 Experiment Result

5.1.6. Safety Cage Design

The safety of the user is the design's highest priority. A safety cage is necessary for separating the robot and the user. The auto-sampler should be able to fit into the safety cage. A limit switch will be installed on the door of the gate to help controller monitor the door status. As mentioned above, the constraint dimension for the auto-sampler is 0.92 m width \times 1.22 m length \times 1.00 m. The manufactured size is 0.45 m width \times 0.55 m length \times 0.90 m height, which is smaller than the size requirement. Safety cage should be transparent for the user to observe the experiment and be compact resistance.

The frame structure is composed of four 609.6 mm and eight 914.4 mm aluminum T-slotted framing bars, making the size of the cage as 0.61 m width \times 0.91 m length \times 0.91 m height. They are standard, easy to construct and strong yet lightweight materials. Three surfaces are covered with PVC coated carbon steel mesh. The front clear door is made of 6.35 mm

thick impact-resistant polycarbonate sheet, which is the only impact-resistant transparent material with lowest cost choice. The design is shown in Figure 5-12.

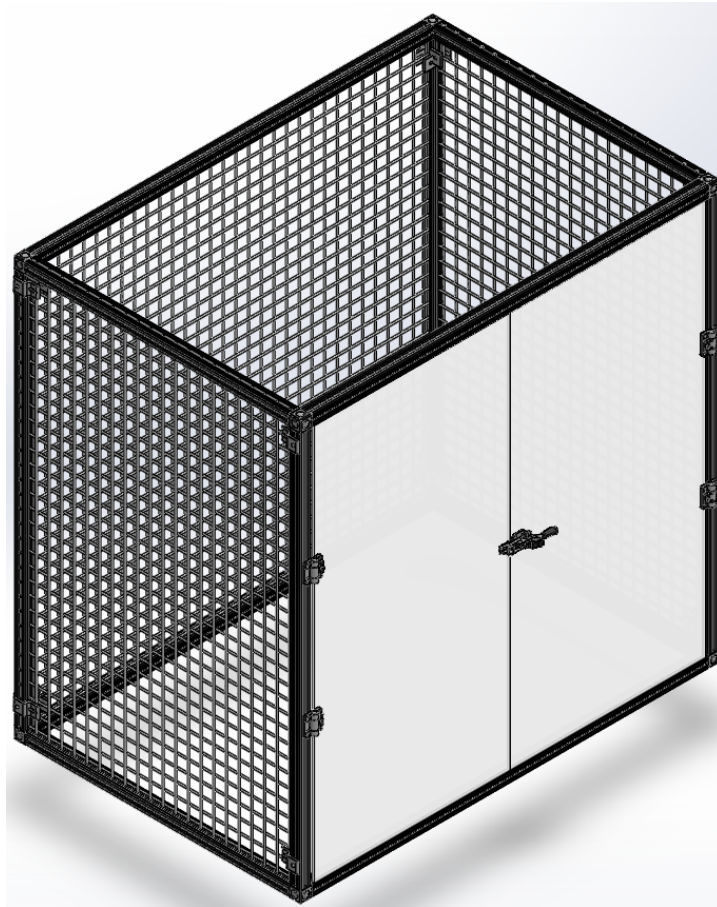


Figure 5-12 Safety Cage

5.2. Electronic Hardware and Circuits

In this section, the electrical system includes DC (direct current) power supply, robot controller DC power supply and power separation and conversion circuits. The main DC power supply is used to power two DC motors, one linear actuator and three lamps for

status indicating. The robot controller DC power supply is a wall adapter. Details about these components and related circuits will be introduced in the following sections. The design constraints include the following,

- The DC power supply is providing 24 V DC with at least 4 A maximum output current.
- The DC power supply should be compatible with 120 V 60 Hz input voltage.
- The DC power supply should be at least 250 W for driving two rotary motors as 83 W each and one linear actuator as 48 W totaling 214 W power requirement.
- The 5V power supply should have maximum 2 A output current to support the controller and the LCD screen.

5.2.1. DC Power Supply

The main power source is the switching mode DC power supply SWS300A-24 [52]. It is shown in Figure 5-13. The input is voltage ranges from 85-265VAC, 47-63Hz. It is the single nominal output power supply and the nominal output voltage is 24V. The output voltage is designed adjustable, which ranges from 20V to 28.8V. The maximum output power is 312W with maximum output current is 13A. The SWS300A-24 efficiency is 82%. It has over current protection when the output current is over 13.7A and the over voltage protection starts when the output voltage is over 30V.



Figure 5-13 SWS300A-24 Power Supply

As for its mechanical characteristics, the weight is 950 g. The operating temperature ranges from -10 to $+65\text{ }^{\circ}\text{C}$. In order to work safely, an inner built blower fan is designed for the active cooling purpose and many holes are drilled for the passive cooling purpose. The dimension of the SWS300A-24 is $52\times 102\times 198\text{ mm}$.

5.2.2. Robot Controller Power Supply

The robot controller is chosen as TTL controller (transistor-transistor logic). It demands a power rail close to $+5\text{V}$, which has a relatively high amount of current to drive other components.

A standard switching AC/DC power adapter is chosen for this purpose [53]. The input

voltage ranges from 110-220VAC. The power supply gives a regulated 5V and maximum output current is 2A.



Figure 5-14 Adafruit Switching AC/DC Power Adapter

As for mechanical characteristics, the cord length is 1830mm and the cord diameter is 3.5mm with a standard coaxial positive tip connector. The overall dimension is 47×33×33 mm.

5.2.3. Power Separation and Conversion Circuits

Since the robot controller uses 5V/3.3V DC but the light bulb uses 24V DC, they have different reference ground. One is the AGND (analog ground) and the other is DGND (digital ground). AGND is from the 24V DC power supply and DGND is from the 5V DC power supply. AGND has more noises that are high enough to influence the robot controller.

As a result of that, ground isolation was necessary. Optocoupler chip SFH617 was applied to isolate the two different grounds. This optocoupler provides up to 5300 V isolation ability. An N-channel MOSFET (Metal-Oxide-Semiconductor Field-Effect Transistor) chip BS270 was applied as the light tower switch. In order to pass the large current, its high-performance version BS270s, with 240mA maximum passing current capability, was chosen. The voltage isolating circuit is designed and shown in Figure 5-15.

If the sensor is the TTL voltage and the controller input is the 3.3V level, which means 2V to 3.3V will be considered as HIGH and 0.8V to 0V will be considered as LOW. Since they share the same power source, the 5V power supply, a voltage division circuit is enough to solve the voltage conversion. It is shown in Figure 5-16. R1 and R2 are the voltage division resistors and R3 is the current limiting resistor.

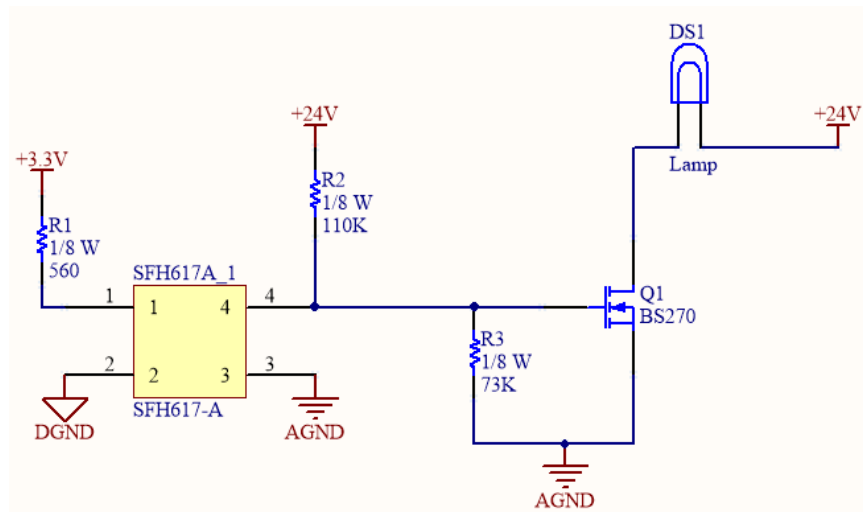


Figure 5-15 Power Separation Circuit

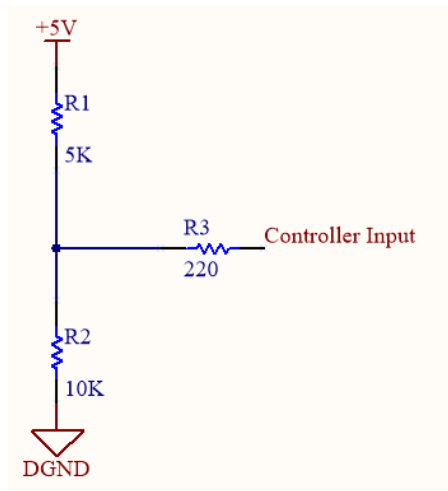


Figure 5-16 Voltage Conversion Circuit

The power extension board is welded and shown in Figure 5-17. The circuit schematic is shown in Figure 5-18. This circuit protects the controller from the powerful 24 V DC power supply.

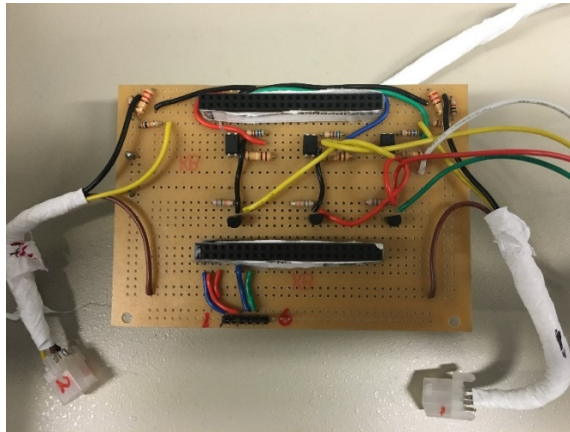


Figure 5-17 Power Extension Board

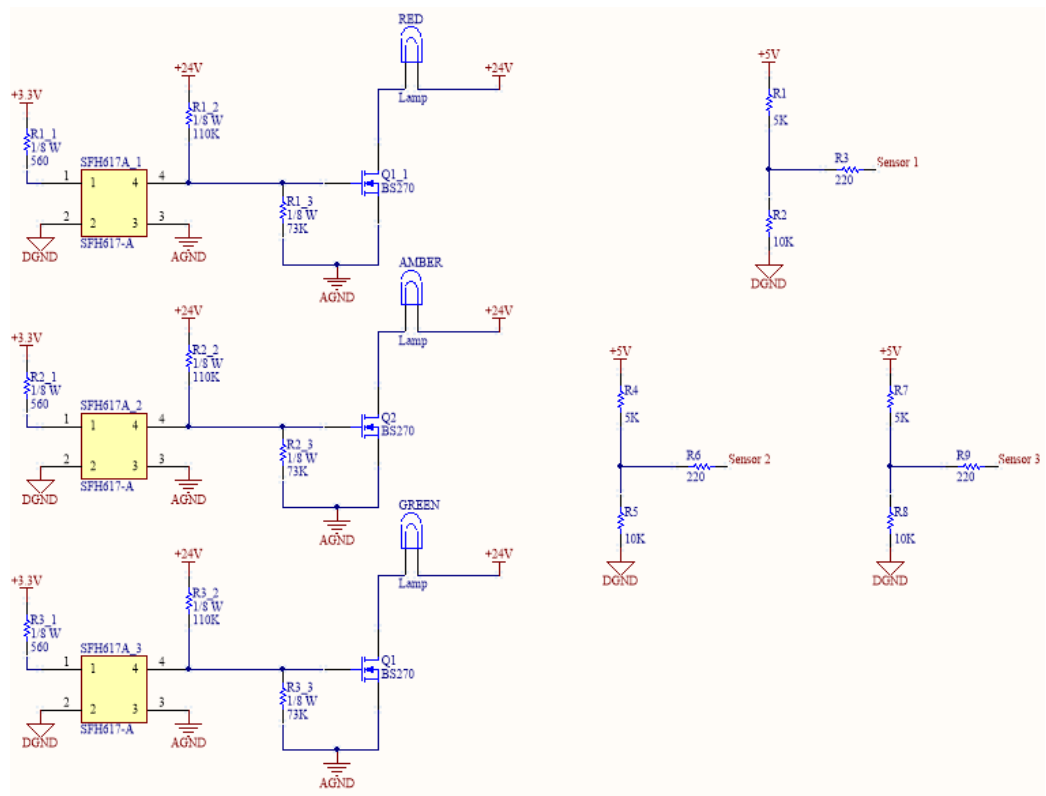


Figure 5-18 Circuit Schematic

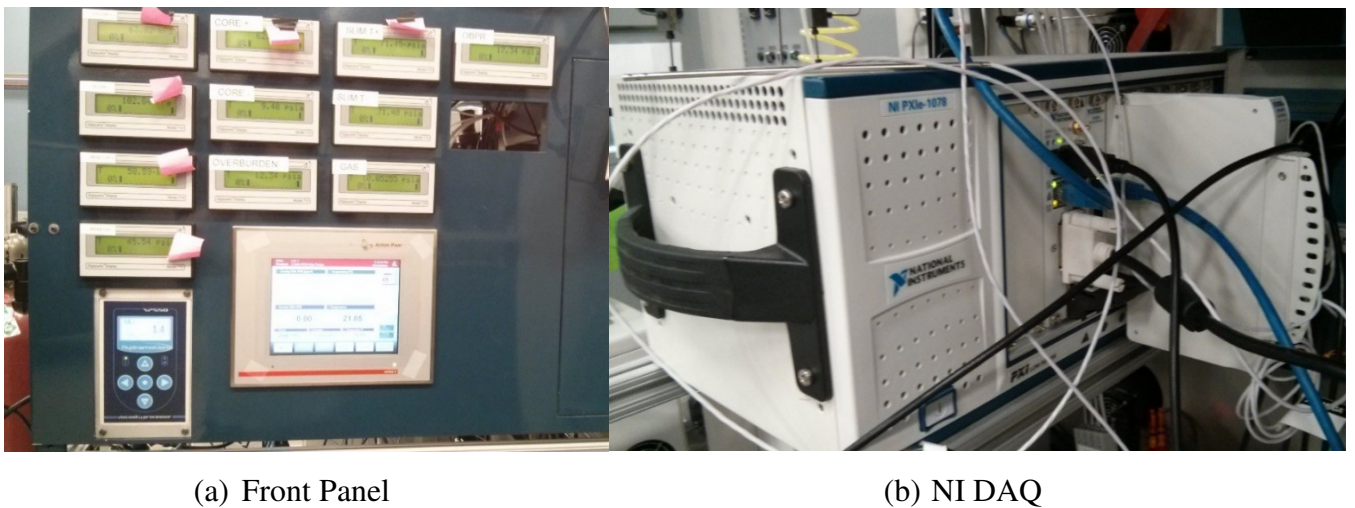
Chapter 6

6. Control System

In this chapter, the control system design of the Five-Bar robot will be introduced. It includes the control structure design, the instruments introduction and selection, the operating process design, the control units selection, and the detailed control strategies introduction.

6.1. Control System Overview

The entire lab environment is controlled by an NI DAQ (Data Acquisition) system PXIe-1078 32-bit, shown in Figure 6-1. It connects all other lab instruments as a system, such as pressure sensors, valves, and viscosity sensors. This system is controlled by Labview GUI and Linux embedded platform.



(a) Front Panel

(b) NI DAQ

Figure 6-1 Lab Control Center

The whole control system structure is shown in Figure 6-2. The supervisory PC is connected to the NI DAQ via an Ethernet cable. The NI DAQ sends experiment requirements to the robot supervisory PC through Labview, and the supervisory PC converts the user command into a communicating signal sending to the robot controller.

The Auto-Sampler robot is controlled by a Beaglebone controller. It receives a command from the supervisory PC and decodes it. The LCD screen and the light tower shows the machine status. Two proximity sensors give the absolute zero-degree position to initialize the relative encoder, and the door limit switch sends the door status signal to the controller. The Beaglebone gives the motor angle command to one slave controller through an I2C communication bus, then the slave controller outputs two PWM (Pulse Width Modulation) signals to the two amplifiers. The amplifiers drive the rotary motor, while the encoders give angle feedback to the controller. Another slave controller separately drives the linear actuator.

The control system is constituted by two control layers; the upper layer controlling the task which translates into managing trajectories, and the second layer constituted by two PID feedback loops that manage each joint position. They are introduced in following sections.

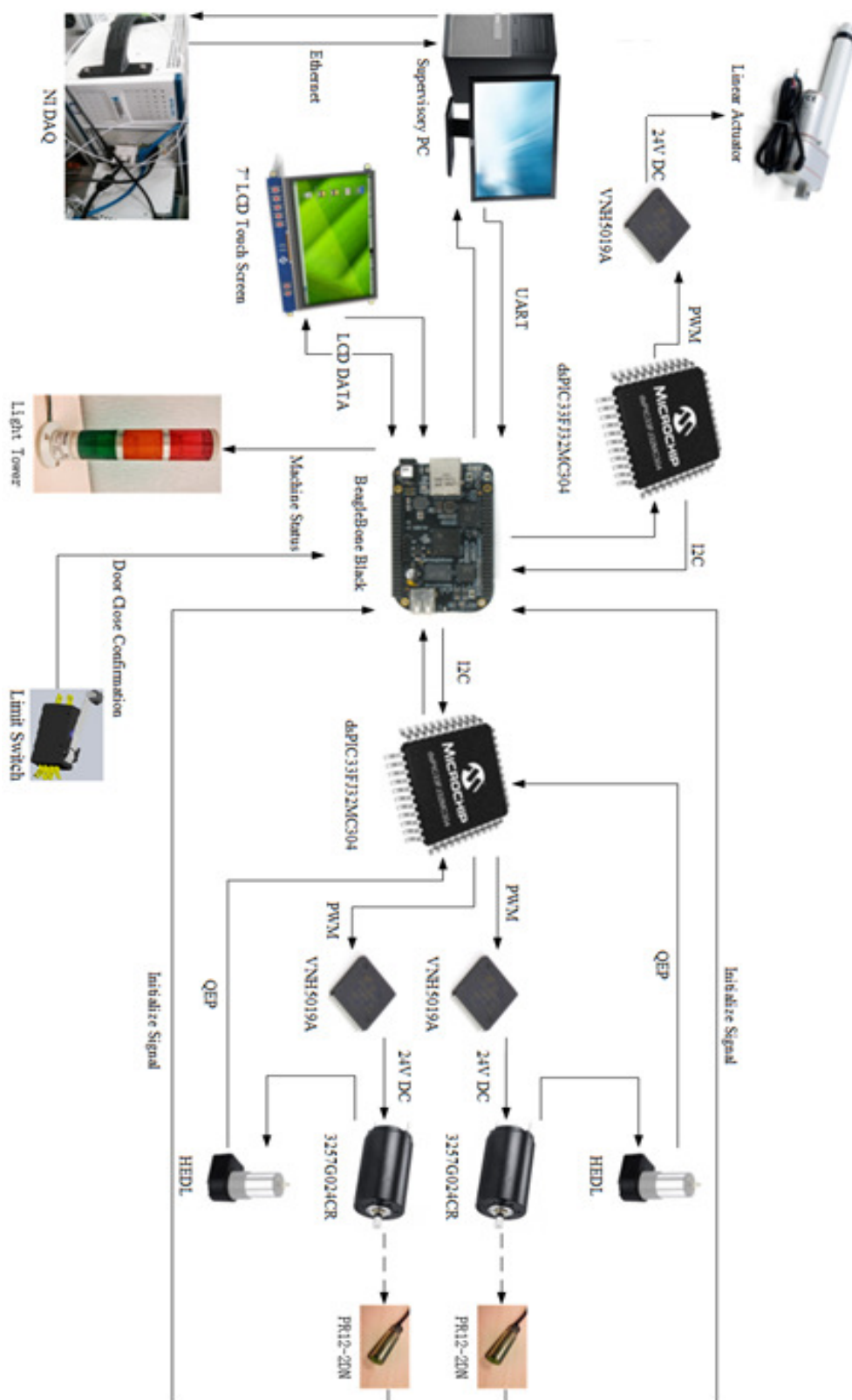


Figure 6-2 Control System Structure

6.2. Instrumentation

In this section, detailed characteristics for each component in this integrated system is presented. These devices are controlled by the robot to sense the environment or to change some environmental attributes.

6.2.1. Robot Controller

The purpose of the controller is to control the work cell, which happens to be the robot. The upstream is the injection valve, while the downstream is the extraction valve. They are both controlled by the NI DAQ. The flow rate of injection and extraction is changed to fit different experiment objectives.

The robot controller should meet the following requirements:

- The controlling of two rotary actuators and one linear actuator needs three separate PWM (Pulse-Width Modulation) signals.
- The signal reading of two rotary motor encoders feedback calls for two QEIs (Quadrature Encoder Interfaces).
- The signal reading of three proximity sensor outputs requires three AI (Analog Input) ports or three GPIO ports
- The controlling of three separate lamps requests three AO (Analog Output) ports or three GPIO ports.

- The communication with supervisory PC via a serial port needs one UART (Universal Asynchronous Receiver/Transmitter) module.

Mature industrial robot controllers designed by FANUC or ABB are usually designed for a certain type or series of robots manufactured by the same company. They can only be operated with specific control software, which is usually a closed-source program ensuring reliability.

Open-source hardware (OSH) is a very promising concept. OSH consists of physical artifacts of technology designed and offered by the open design movement. The term usually means that information about the hardware is easily discerned so that others can make it – coupling it closely to the maker movement [57].

The three devices which were considered potential micro-controller candidates for the robot controller are BeagleBone Black (BBB), Raspberry Pi, and Arduino. Each has been successfully applied in many fields such as electronics, environmental science, robotics, network, and 3D printing.

Table 6-1 Robot Controllers Comparison

	BBB	Raspberry Pi B+	Arduino Due	Winner
Size	Same	Same	Same	Same
Frequency	1GHz	700MHz	84MHz	BBB
Memory	512MB DDR3	512MB SDRAM	92KB SDRAM	BBB
Flash	4GB flash	SD expansion available	512KB	BBB
USB ports	Single slot	4 regular slots	2 micro slots	Pi
UART	6 Modules	1 Module	4 Modules	BBB
Digital I/O	69	27	54	BBB
Operating Voltage	5V	5V	3.3V	Arduino
Price	\$55	\$40	\$46	Pi
Operating System	Yes	Yes	No	BBB/Pi
ADC	8ch 12-bit	0	12ch 12-bit	Arduino
DAC	0	0	2	Arduino
Expansion Headers	92	40	66	BBB
PWM	6	7	12	Arduino
Encoder Connectors	3	0	0	BBB
Score (Max=15)	9	5	5	BBB

A technical comparison was completed in order to choose the best from these candidates.

Required specifications (listed in Table 6-1) were evenly weighted and the device receiving the highest score is deemed as the optimal device for this application.

According to the evaluation result and the design objectives, the Beaglebone Black is considered the best choice. The kernel of the BBB is an AM3358, which is an ARM

Cortex-A8 structure with up to 1GHz frequency.

The BBB is capable of a lot of accessories. It has the potential to use HDMI for friendly interface development. It can support Linux and Android as the main on-board operating systems, which are both supported by a strong developer community. The BBB also contains many subsystems to expand its function, shown in Figure 6-3.

Another impressive feature of the BBB is that its functionality can be extended with daughter boards, called CAPEs, which connect to the P8 and P9 headers. They are called CAPEs due to the shape of the boards as they wrap around the RJ-45 Ethernet connector, as much as four capes can be connected at one time [58]. Developers can design their own CAPEs and attach them securely to the BeagleBone using extension headers [58]. This function produces more possibilities than other microcontrollers, which boosts BeagleBone hardware and software ecosystems.

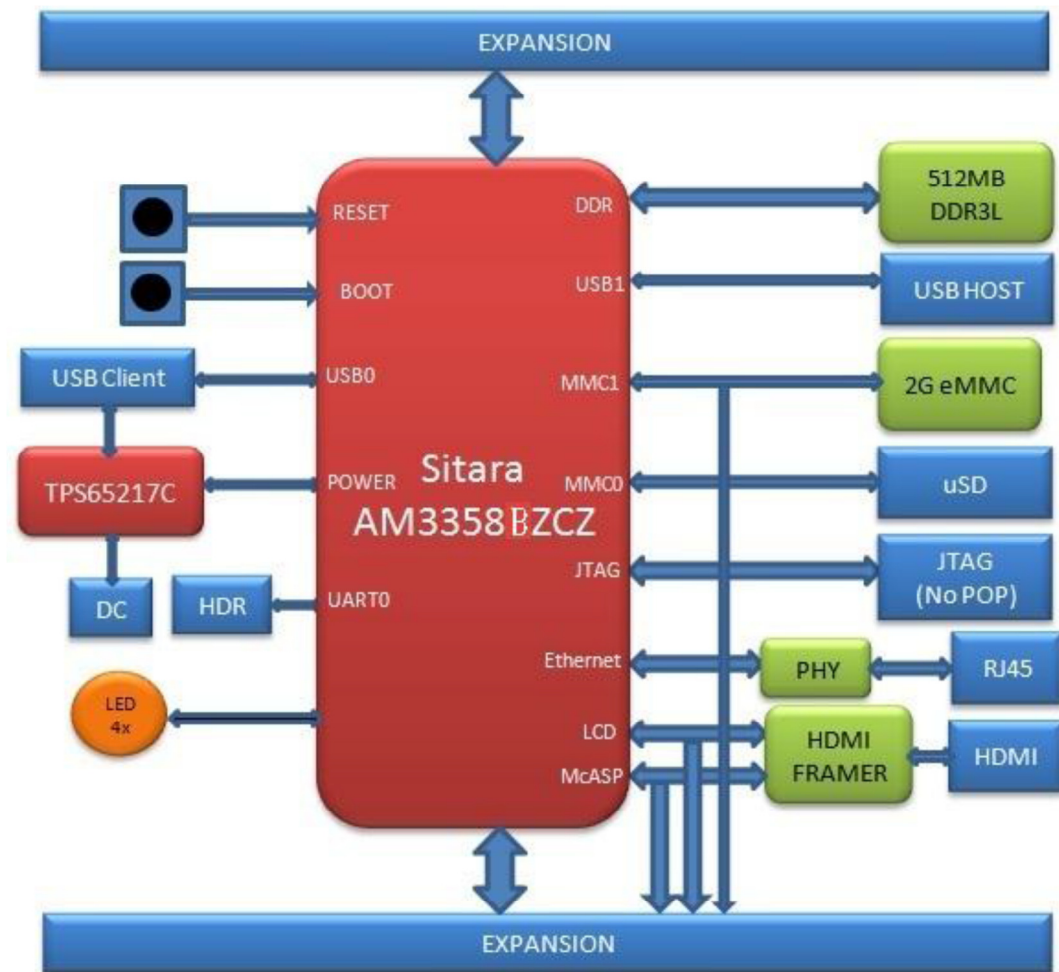


Figure 6-3 BeagleBone Black Structure Block Diagram [59]

6.2.2. DC Motor Driver

The driver circuit is located between the motor and control circuit. It is used to convert the control signal from the robot controller to switch the signal applied to the electrical device and power source. For a semi-control device, the driver circuit only needs to provide an ON signal. For a full-control device, the driver circuit has to provide ON and OFF signals.

The Linux OS (Operating System) was not designed for real-time or predictable processing. Its kernel is not preemptive, which means that once the processor begins executing kernel code it cannot be interrupted [58]. Therefore, if the BeagleBone has to decode an algorithm, the motor control, and interact with GUI simultaneously, it may not be able to process so many tasks in real-time.

There are two ways to solve this problem. First, within the BeagleBone's kernel AM335x, there are two on board sub-microcontrollers called PRUs (Programmable Real-time Units), which can be programmed for real-time interfacing applications [58]. Another solution is to use a slave controller as a CAPE and let the slave controller perform the real-time control task.

The DMCC (Dual Motor Control CAPE) was chosen as the driver circuit, shown in Figure 6-4. The slave controller is a 16-bit DSC (Digital Signal Controller) dsPIC33FJ32MC304. It has two QEI (Quadrature Encoder Interface) modules with a 16-bit up/down position counter, four PWM (Pulse Width Modulation) generators with a 16-bit glitchless PWM mode, one I2C (Inter-Integrated Circuit) module and one RTCC (Real-Time Clock and Calendar) module [61].

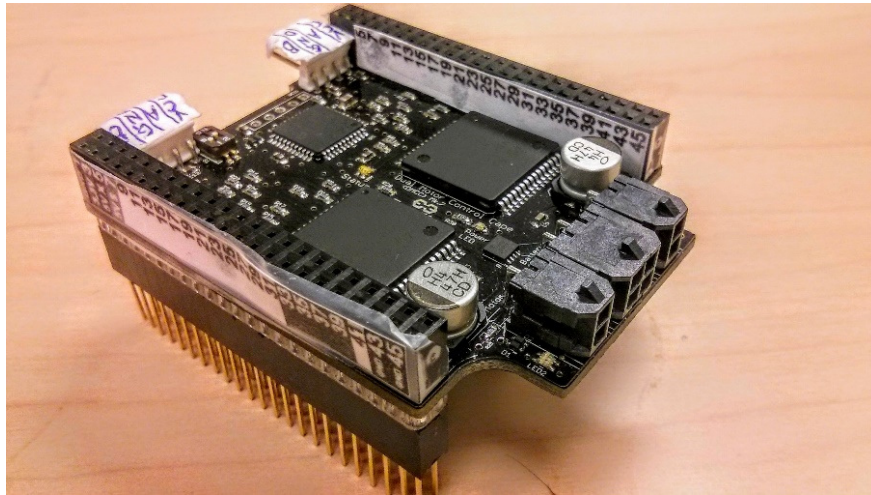


Figure 6-4 Dual Motor Control CAPE

Two QEIs can accept feedback signals from two encoders, and four PWM modules can control up to four motors independently. The I2C can communicate with the master controller.

The VNH5019A full bridge motor driver was chosen as the amplifier. Every chip is able to drive a single motor with up to 41 V DC nominal voltage and 30 A maximum current.

DMCC is produced by Exadler Technologies, which has the PID control embedded in the firmware [62]. BeagleBone, as the master controller, sends the command based on a communication protocol through I2C to DMCC. DMCC, as the slave controller, will accomplish the motor control and send a status report back to the BeagleBone.

The DMCC is designed by Exadler Technologies and the schematic is shown in the

appendix.

6.2.3. Proximity Sensor

A sensor is a transducer used to detect and transfer a certain physical signal to an electrical signal for further analysis. In this project, optical encoders and inductive proximity sensors are introduced.

The inductive proximity sensor has an oscillating circuit inside. With a voltage applied to the oscillating circuit, it can create a magnetic field. When a metal object gets close to this magnetic field, an eddy will be produced inside of the metal object. As a result, the oscillating effect will be decreased or even stopped. The change of the oscillating effect in the oscillating circuit is transduced into an electrical signal and amplified afterward. By testing the sensor output voltage of the inductive proximity sensor, we can detect the approach of a metal object.

In this project, Autonics PR12-2DN with 2 mm sensing distance proximity sensors were chosen as Figure 6-5. Two of them are used for robot initialization.



Figure 6-5 Autonics PR12-2DN

6.2.4. Door Switch

A limit switch is installed in the system in order to sense whether the door is opened during the experiment process, This switch is composed of a coil spring, snap action mechanism and long lever with a roller. It can be applied in household appliances, automobiles, and door sensing systems, shown in Figure 6-6.

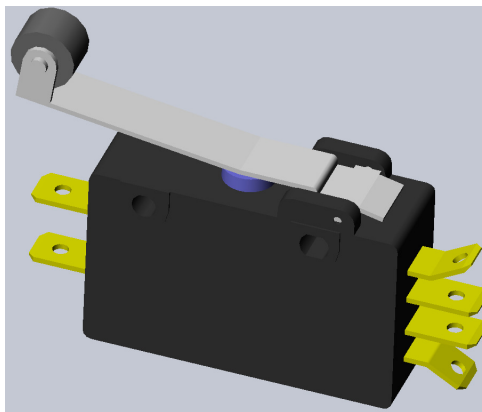


Figure 6-6 Hinge Lever DPDT Limit Switch

This limit switch is a DPDT (Double Pole Double Throw) switch and it is normally open.

Under normal circumstance, the limit switch is pressed by the door and it is in close status.

Once the door is opened, the limit switch will be opened as well.

The DPDT switch has six terminals. It can control two separate circuits but they are always switched together by a single actuator. Based on this, the first pole is connected to 3.3V and the first throw is connected to the controller. The second pole is connected to a 24V DC and the second throw is connected to motors power line. Once the switch is opened, motor power will be cut for safety and a signal will be sent to the controller simultaneously.

Choosing this switch is fully considered based its electrical specification. The power rating is 1 HP for 125 VAC and 2 HP for 250 VAC, which reflects the amount of current the switch contacts can handle at the moment the device is turned on. The amp rating is 20 A at 125/250VAC. The switching mode power source has an inrush current up to 20 A so this switch is suitable.

6.2.5. Light Tower

A light tower is another safety feature. The light tower can warn people that the robot is working in a distance.

EDWARDS SIGNALING 113SS-RGA-AQ was used, shown in Figure 6-7. It uses a 24V DC steady light bulb and the working current is 0.24A each. The lamp life is over 500 hours.

The lamp tower is a surface mounting type with three M4 mounting holes. The lens diameter is 52mm.



Figure 6-7 Light Tower

6.2.6. Encoder

A two channel optical incremental encoder is another type of sensor used in this project.

The encoder can give controller the angle value that the motor shaft has turned. It provides the essential feedback signal for motor control. The accuracy of the incremental encoder is decided by how many lines per revolution. The encoder is more accurate with a higher the number of lines per revolution.

The optical incremental encoder consists of one shaft disk with many small grooves, a LED transmitter, and a light receiver. The output is two channels of pulse signals with a 90-degree phase angle difference. The encoder shaft is connected with the motor shaft. The

motor rotating angles can be calculated by counting how many pulse peaks are created.

Furthermore, the motor direction can be decoded by detecting the signals of the channel A and channel B.

HEDM 5500 was chosen for this purpose. It is a 5V DC optical incremental encoder. Two outputs, channel A, and channel B, are not only helpful for increasing the accuracy, but it's also helpful for recognizing the motor shaft rotating direction. Its accuracy is up to 1024 lines per revolution. The output signal is shown in Figure 6-8. Every high peak signal in CH.A or CH.B is counted as plus or minus one depending on the motor rotating direction, which will decide the CH.A and CH.B peak arriving sequence. The 1024 lines per revolution means one full turn 360 degrees is divided by 1024 and every count equals

$\frac{360^\circ}{1024} = 0.35^\circ$. Each full rotation is performed, and CH.I will output a high peak signal.

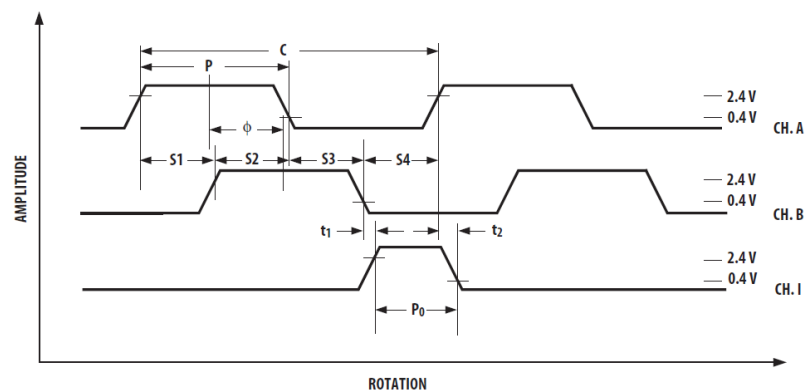


Figure 6-8 HEDM 5500 Output Waveform [54]

6.2.7. Solenoid Valve

Solenoid valve is a kind of electromechanical valve. Instead of manual control. The solenoid valve is controlled by an inner built solenoid. With the current going through the solenoid, the 2-way valve can be switched on or off. In the case of the 3-way valve, the outflow will be switched between the two out ports.

In this project, the Parker Two-Way Normally Open Solenoid Valve is chosen, shown in Figure 6-9.



Figure 6-9 Parker 2-Way Normally Open Solenoid Valve

This product has been widely applied in different scenarios requiring general fluid and gas control, such as hospital sterilization equipment, lubrication equipment, and air horns. It is an 1/8 inch NPT (National Pipe Thread) 303 stainless steel valve. The operating pressure differential is from 80 PSI up to 375 PSI. Actuating voltage is 24 V DC and maximum current is 0.41 A.

6.3. Operating Process and Control Units

In this section, the detailed operation process is introduced, and then control units for the work cell are selected and presented.

6.3.1. Operating Process

The entire operating process diagram is shown in Figure 6-10. Before using the robot sampler, the supervisory PC with control GUI should be opened and the robot controller should be powered. The status light should be checked and all necessary cables should be firmly connected. The test tubes are inserted in the test tube rack and brought to the sampling work cell.

The user opens the door and inserts all the test tubes inside. Before turning on the power source, the user should close the safety cage tightly and launch the control software on the supervisory PC. The green light showing the start status will be powered on once the power source is switched on.

The working plane is fixed. The first step is to calibrate the auto-sampler manipulator and make it find the home position. This is performed only once when the controller is switched on and if the safety cage door is closed. The robot arms will move towards the calibration proximity sensors, which are physically installed at the 0 degree and 180 degree position. Once they send feedback signals to the robot controller, the robot controller will set the

encoder values to zero for joint position initialization and the amber and green lights showing the home status will be powered on.

After the user specifies the number of desired test tubes, the desired experiment time and clicks the 'GO' button, the auto-sampler will start the palletization process and the yellow light showing working status will be turned on. The sampling end-effector is positioned over the desired test tube position. The injection needle is brought down into the test tube. After the specified experiment time is over, the needle will be pulled up.

Next, the end-effector will be moved over the next test tube. The auto-sampler will repeat the same operation motion until it reaches the final test tube. When all test tubes are palletized, the auto-sampler will turn back to the home position.

Three lamps are lit to indicate to the user that the work is complete and to notify the operator to change the test tube rack or click the terminate button to close the experiment.

If the user doesn't click the termination button and decides to conduct another experiment, the user should open the safety cage door and refill the test tube rack. After the test tubes are in the safety cage and the door is closed tightly, the user can click the initializing button and re-specify all experiment details.

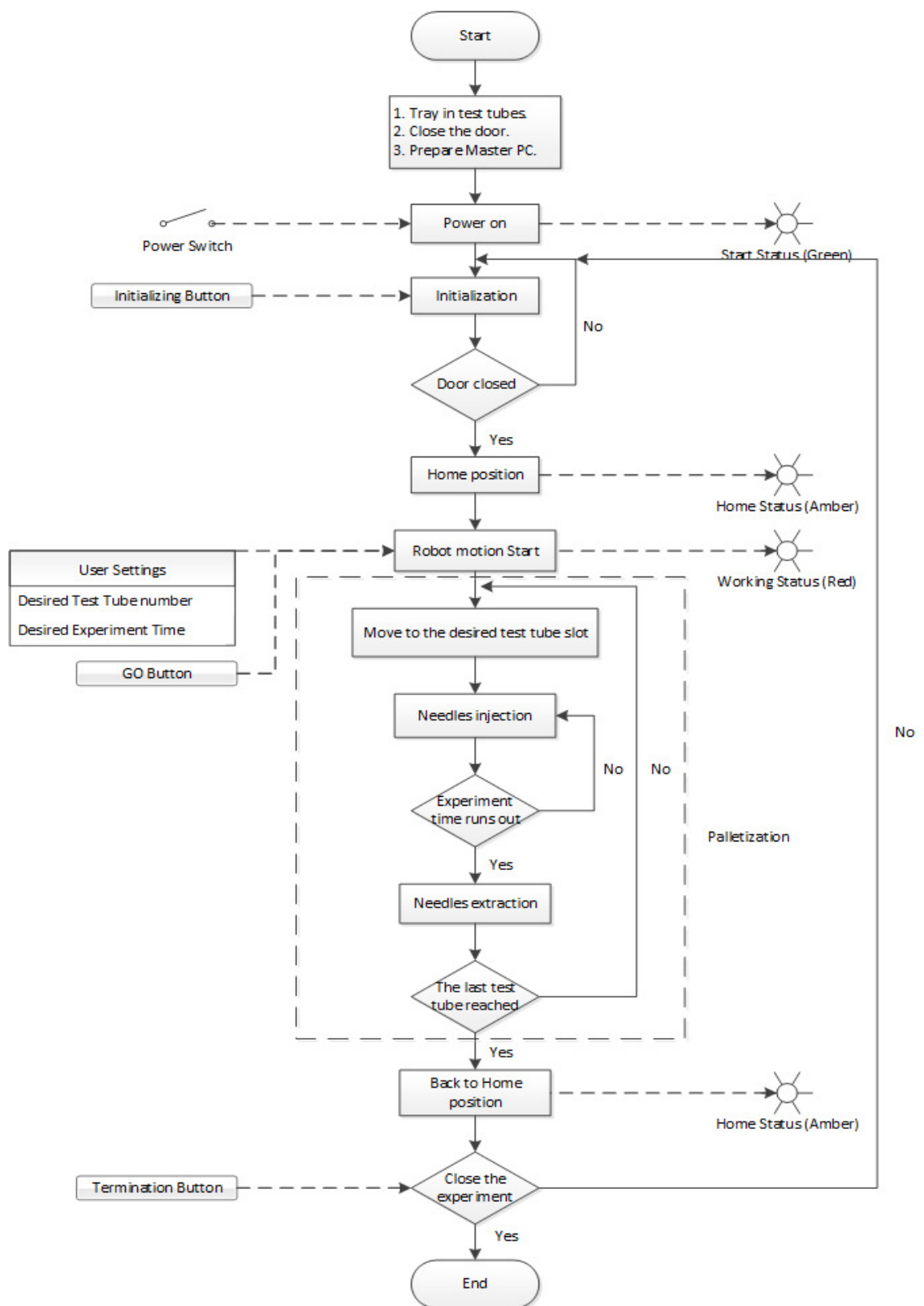


Figure 6-10 Operating Process Diagram

6.3.2. Labview Control GUI

For the supervisory PC, it should have Labview installed. It is a programming environment. Comparing other traditional text-based programming language, Labview uses modularized graphical language to program. Since Labview is designed by National Instruments, which has a solid hardware research ability and a huge hardware family, this language is highly merged with the hardware. The supervisory PC and robot controller communicate via the serial port. The NI-Serial Driver should be installed separately for full function. The Labview control GUI is designed and shown in Figure 6-11. Furthermore, the Labview GUI control logic diagram is shown in Figure 6-12.

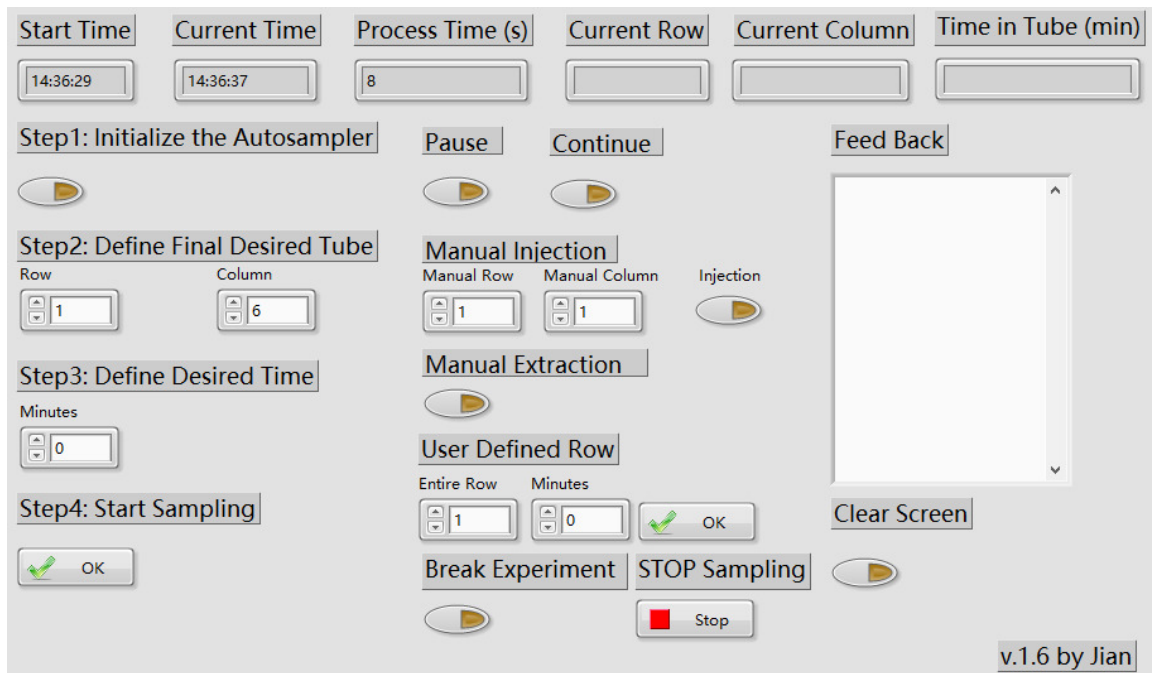


Figure 6-11 Labview Control GUI

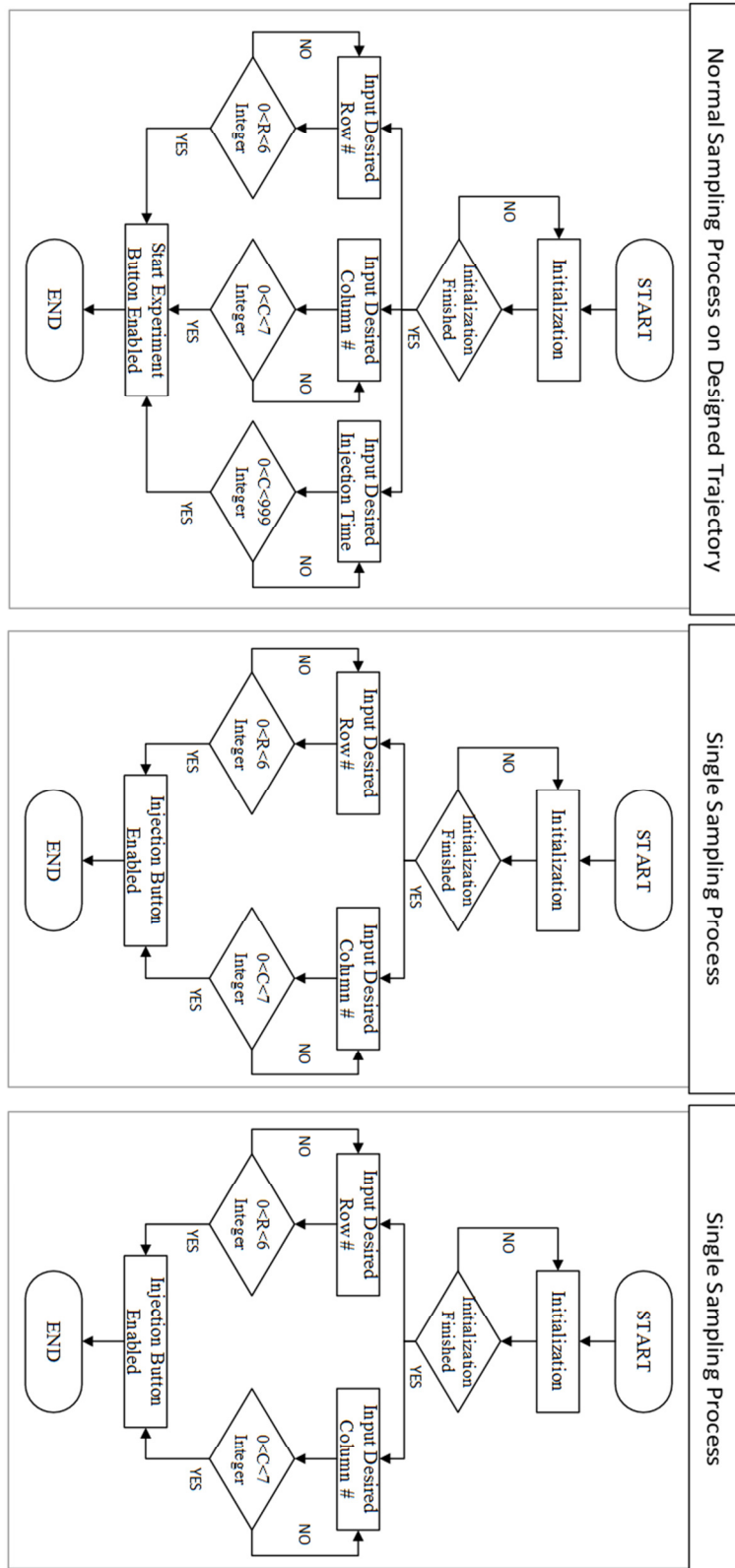


Figure 6-12 Labview Control GUI Logic Diagram

The PC USB port can be used as a serial port but it needs to be converted to 3.3V UART to suit the BeagleBone Black signaling voltage level. As a result, the FTDI TTL-232R-3V3 is chosen as the serial communication cable, shown in Figure 6-13. The TTL-232R cables are a family of USB to TTL serial UART converter cables incorporating FTDI's FT232RQ USB to Serial UART interface IC device which handles all the USB signaling and protocols [60]. It converts USB to 3.3V UART.



Figure 6-13 FTDI TTL-232R-3V3 Serial Cable [60]

The developed system is composed of a master PC, a controller, and a Five-Bar manipulator. The system is shown in Figure 6-14.

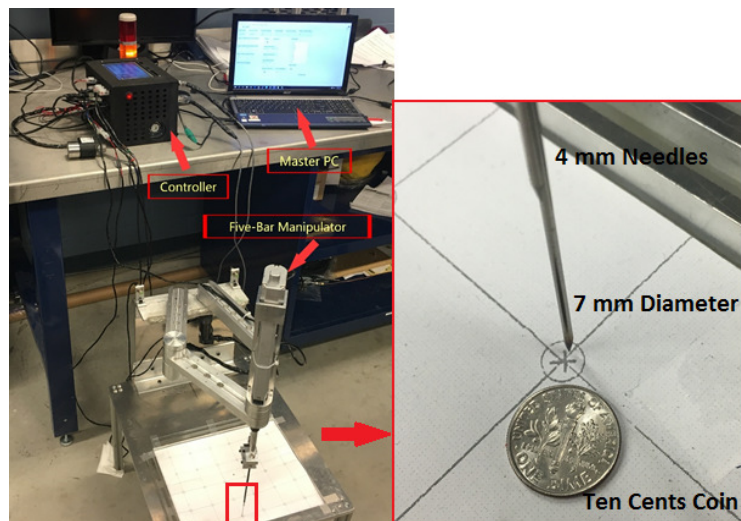


Figure 6-14 Five-Bar Auto-Sampler System

6.4. Control Strategies

The multi-level control structure is proposed. The robot control constitutes of two levels: the servo level on three axes that are two rotary axes and one linear axis, and the task level, shown in Figure 6-15.

Details about lower servo level and upper task level will be introduced in the following sections.

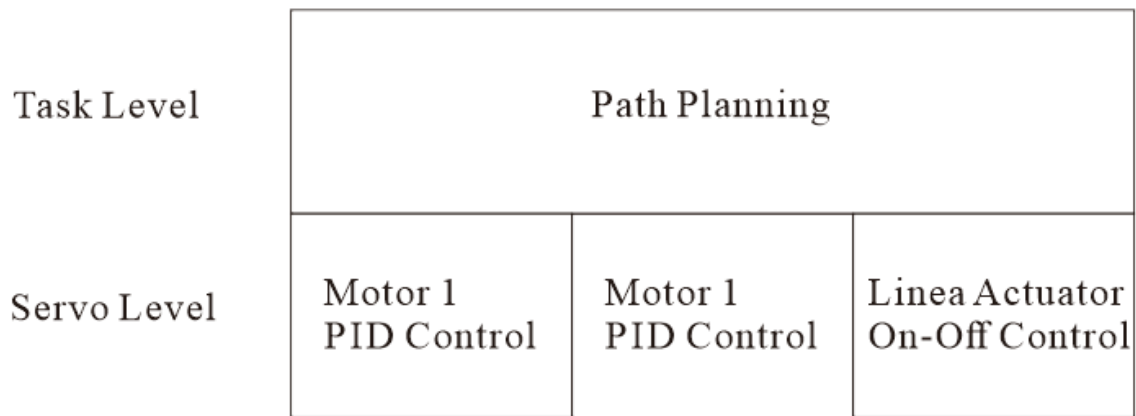


Figure 6-15 Multi-Level Control Structure

The Servo control accepted the classical PID controller. PID control is a conventional model-free feedback control approach and has been extensively applied in industrial applications because of its simplicity.

The Ziegler-Nichols rule gives researchers a systematic way to tune the PID controller and

improve the control performance [56].

6.4.1. Servo Level Control Strategy

The servo level control includes the controlling of three axes of the robot. The classic PID (Proportional-Integral-Derivative) controller in parallel form is used for two rotary motor control. The on-off controller, so called ‘bang-bang’ controller, is applied to linear actuator.

Ziegler-Nichols Rule

The Ziegler-Nichols Rule is used to tune the PID controller. Based on Zeigler and Nichols [55], formulas are provided which enable the controller settings to be determined from experimental or calculated values of the lag and unit reaction rate of the process to be controlled. The step by step process of tuning as follows:

1. Apply the single P-controller with integral and derivative parameters, both equaling zero.
2. Adjust the proportional gain K_p , and use the trial and error method to let the system get into the borderline state, where the system output is in low-frequency oscillation state with the lowest K_p experimental value as K_p .
3. Observe and measure the period of the oscillation frequency. Invert the frequency experimental value to obtain the borderline period as T_p .

4. Use the following equations to calculate classic ZN parameters.

$$K_p = 0.6Kp \quad (6-1)$$

$$T_i = 0.5Tp \quad (6-2)$$

$$K_I = \frac{K_p}{T_i} \quad (6-3)$$

$$T_D = 0.125Tp \quad (6-4)$$

$$K_D = Kp \cdot T_D \quad (6-5)$$

The Zeigler Nichols method is implemented to gain robust control performance. After tuning, the PID parameters are tabulated in Table 6-2.

Table 6-2 PID ZN Parameters (Same on Two Controllers)

Parameters	Amount
K_p	25.15
K_I	5.45
K_D	19.50

On-Off Controller

The on-off controller, also known as ‘bang-bang’ controller, is a controller switching

between two statuses back and forth. Only completely on and completely off states are considered in the controller.

The linear actuator has two limit switches built inside. One is located at the back end while another one is located at the front end. By reading the limit switch on or off, the motor status is decided only between full power or no power. The voltage is positive. Once the extracting motion is required, the controller value is reversed leading to the voltage reversed to negative.

6.4.2. Task-Level Control

In this project, the targets are fixed test tubes in Cartesian coordinates, which means each target has a fixed two-dimensional coordinate value. Based on the kinematic algorithm introduced in the previous section, the two-dimensional coordinate values $\begin{bmatrix} x \\ y \end{bmatrix}$ can be transferred into two motor angles $\begin{bmatrix} \theta_1 \\ \theta_2 \end{bmatrix}$.

Any two points within the workspace, A and B, are chosen in the robot workspace, a single line trajectory from A to B can be created. This is the most direct trajectory. In order to let the end-effector move along this trajectory, this single line can be divided into many line segments, equaling many sub-points. The PID controller is used several times to keep the control results away from overshooting.

Based on the kinematic algorithm, each sub-point relates to a pair of angles, θ_1 and θ_2 . Equally, this single line trajectory can be transferred into a curve of motor one's angle and a curve of motor two's angle.

6.4.3. Path Planning:

If the desired trajectory is a complex geometrical path, to ensure all test tubes are ergodic, the path should be divided and angles should be calculated. The desired sampling task is actually defined by a pick-and-place procedure with palletization. It only requires reaching several points which are deployed on a network of rectangles. Hence, these tasks only call for approximate lines between the points but not necessarily keeping straight lines.

In order to sample all thirty test tubes, the desired trajectory is planned and is shown in Figure 6-16. In the simulation, the designed auto-sampler configuration is used, as proximal arm 230 mm, distal arm 250 mm, and motor offset 80 mm.

The outer and inner red curve edge is the edge of the workspace. The black square represents the test tube tray and the 30 colored solid circles represent 30 large test tubes with the 30 mm diameter. The initial robot configuration is shown in the blue dash line. The initial configuration is located where θ_1 and θ_2 both equals ninety degrees.

The Robot starts from the initial configuration and then samples test tubes row by row.

After all of the test tubes are finished, the robot will return to the initial configuration.

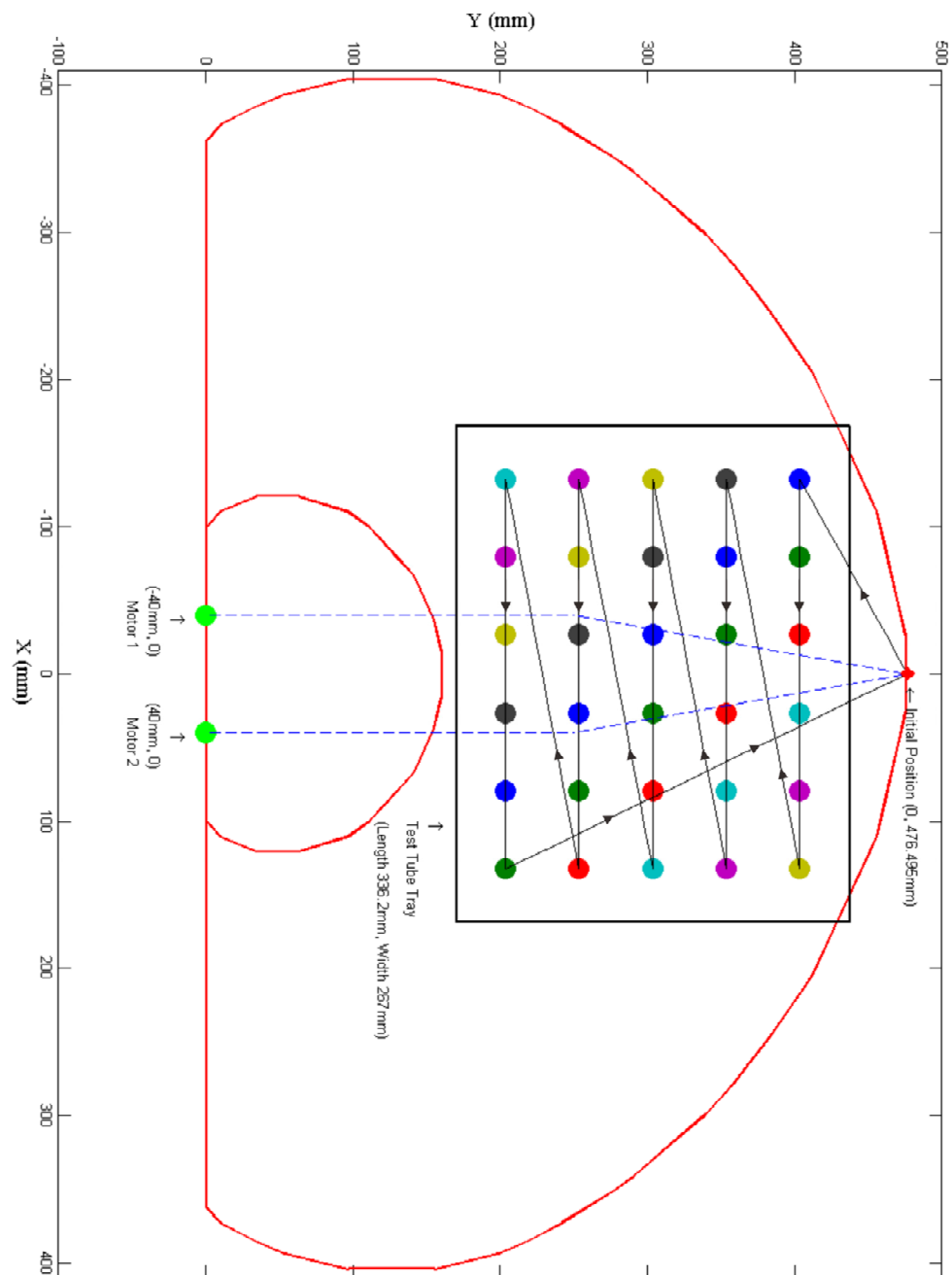


Figure 6-16 Trajectory Plan for All Test Tubes

Chapter 7

7. Autosampler Commissioning

7.1. Methodology

Before delivery of the Five-Bar autosampler to the client, the commissioning was performed based on the several test scripts. The test scripts are sets of specific instructions that will be performed on the system to be tested in order to ensure that the system functions as expected. In order to test the Five-Bar autosampler, three test scripts have been proposed, which are operational test, failure test, and fluid test. The operational test, referred as the positive test, is to test the normal functions of the auto sampler under standard operations. The failure test, referred as the negative test, is to check the protection logic of the autosampler's controller dealing with the failure situations. The fluid test, referred as the supplementary test, is introducing the fluid into the auto sampler to test the fluid control of the autosampler.

Every test section was raised and approved by the Hibernia EOR laboratory. Meanwhile, the whole testing process was proceeded strictly following the test scripts under the Hibernia EOR laboratory's monitoring.

7.2. Operational Tests

In the operational test, it is assumed that the auto-sampler is used as correctly as it is designed. The operational tests comprise a collection of the important tasks which describe the auto-sampling process and which are handled by the robot and its controller. It will be powered and then properly connected with the supervisory PC. Afterward, the auto-sampler will be initialized, and then different modes can be chosen, including a full rack of 30 test tubes injected and extracted one by one with a defined experiment time, defined single row (five rows in total) with defined experiment time, and single test tube experiment. Finally, the experiment can be terminated by the user command. Two needles have 4 mm total width and the inner diameter of the small test tube is 7 mm. Therefore, the error has to be controlled within ± 1.5 mm, as shown in Figure 7-1.

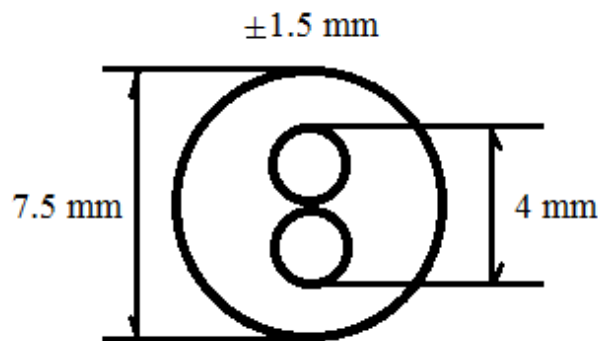


Figure 7-1 Sketch of Piercing Holes on Septum

All of the required operations are performed as how it should be. The robot operational tests showed that it could proceed with test tube sampling at the required performance. It is

notable that the robot can proceed with the sampling of all the test tubes or small portion of those. The process has reached the required accuracy for needle injection in the test tubes. The detailed operational test script with related test results are shown in Appendix 10.9.

7.3. Failure Tests

The failure tests comprise a collection of the situations which have been identified as potentially problematic to the auto-sampling process, the robot and people security. These failure tests are divided into two types of problems: hardware failures and position errors. In the second case, the auto-sampler is placed in many problematic positions which normally lead to task or system failures.

The autosampler was powered and connected properly as the normal starting in operational test. However, many failure scenarios were tested before or during the normal experiment process. For example, it includes: random initial configurations to check unwanted starting positions; unexpected input for control GUI; opening the door during the experiment to check if the robot will be neutralized and continue the experiment after the door is closed; reposition the end-effector close to the singularity to see if it can cross the singularities; disconnect the power cord during the experiment. In the end, the robot effectively handled all unwanted situations and passed all of the failure tests.

The robot failure tests showed that it could proceed with failure or error recoveries in all

instances. Moreover, it could proceed with calibration from any position in its workspace.

The robotic system should be able to reduce downtime and ensure proper operations automatically for long periods of time. The failure test script with related test results are shown in Appendix 10.10.

7.4. Fluid Tests

The fluid tests are a repetition of some selected Operational Tests with the difference that a fluid is used during the process.

The fluid test also checks the function of the solenoid valve and controller's algorithm handling fluid. In this research, the fluid is chosen as the water because safety concern as well as the oil equipment was not commissioned at the testing time. The autosampler was started normally and perform all of the test tubes sampling task. In the test, the water was pressured by a pump. The autosampler finished all required injection and extraction. The fluid test was successfully passed. There was no fluid leakage or spill during the whole test. The fluid test script and related test results are shown in Appendix 10.11.

Chapter 8

8. Conclusion and Future Work

8.1. Conclusion

The auto-sampler is one of the essential units in the experiment. This research contributes a new type of auto-sampler other than traditional planar or rotating auto-sampler for specialized core analysis laboratory studies. We researched a 2-DOF parallel robot. Specifically, we analyzed, built, and tested a Five-Bar robot. Five-Bar robots are commonly used but this is the first known Five-Bar robot for laboratory oil and gas auto-sampling, of which we aware.

First of all, in the kinematic analysis, the inverse kinematic problem, and the forward kinematic problem explicit solutions are obtained through the vector method. The workspace and the singularities are calculated and plotted. The kinematic optimization is performed for reaching the largest workspace area on different combinations of arm dimensions. Based on the optimization results, the most reasonable combination of the arm dimensions reaching the research objective is acquired, and it gives support to the following dynamics analysis and the mechanism design.

We compared the dynamic performance results using the traditional Lagrangian analysis

and the bond graph method. Comparing the results obtained from these two methods, we found that the errors between them are small, justifying bond graph as a valid dynamic analysis approach. As a result, bond graph method was used for Five-Bar robot dynamics analysis. PID control was applied to the bond graph model. Control results of the bond graph model are obtained and analyzed, showing that the motion of the Five-Bar manipulator can be simulated properly. The bond graph is validated as a proper dynamic method and the results were used to support the following engineering design for motor selection and manipulator design.

The engineering design consists of the mechanical design and the electrical design. The strength of the structural arm design is validated by static analysis. The mechanical structure is designed and manufactured. The required piercing force of the injection needle is experimentally tested and validated. The electrical system is designed and assembled. The analog ground and the signal ground are separated by specifically designed power separation, which keeps the signal processing away from the disturbance noise of the DC power source.

The instrumentation and controller are selected based on the research objectives and overall design requirements. All components are connected making an integrated system. The control strategies are designed and applied to the control algorithm. They are tuned based

on Ziegler-Nichols Rule. In the end, the path is planned for Auto-Sampling task specifically.

8.2. Future Work

The Five-Bar robot for auto-sampler is a promising design. The following aspects can be improved and further researched.

- (1) Different five-bar working modes can be switched between each other in the shared workspace. Experiments can be conducted to research the influence of multiple working modes on dynamic performance.
- (2) The error tolerance of the Five-Bar robot can be calculated.
- (3) More advanced control strategies and methods can be researched and tested. The limit of the control accuracy can still be improved, if required.

9. BIBLIOGRAPHY

- [1] Standard, I. S. O. 8373: 2012. (2012). Robots and robotic devices–Vocabulary.
- [2] J. E. Gwinnett. Amusement device. 1931. US Patent No. 1,789,680, 1931. Available: <http://www.google.com/patents/US1789680>.
- [3] P. J. Willard. Lacey. Georg. Spray painting machine. US Patent No. 2,213,108, 1940. Available: <http://www.google.com/patents/US2213108>.
- [4] P. J. Willard. Lacey. Georg. Position-controlling apparatus. US Patent No. 2,286,571, 1942. Available: <http://www.google.com/patents/US2286571>.
- [5] I. A. Bonev. The True Origins of Parallel Robots. 2003. Available: <http://www.parallemic.org/Reviews/Review007p.html>
- [6] D. Stewart. A platform with six degrees of freedom. Proceedings of the Institution of Mechanical Engineers 180(1), pp. 371-386. 1965. DOI: 10.1243/PIME_PROC_1965_180_029_02.
- [7] R. Clavel. Device for the movement and positioning of an element in space. US Patent No. 4,976,582, 1990. Available: <http://www.google.ca/patents/US4976582>.
- [8] S. Vorndran. Low-Inertia Parallel-Kinematics Systems for Submicron Alignment and Handling. Available: <http://www.parallemic.org/Reviews/Review012.html>
- [9] C. M. Gosselin and J. -. Hamel. The agile eye: A high-performance three-degree-of-freedom camera-orienting device. Presented at Robotics and Automation, 1994. Proceedings. 1994 IEEE International Conference on. 1994, DOI: 10.1109/ROBOT.1994.351393.
- [10] C. K. L. Motion simulator. 1967. Available: <http://www.google.com/patents/US3295224>.
- [11] C. M. Gosselin and F. Caron. Two degree-of-freedom spherical orienting device. 1999. Available: <https://www.google.ca/patents/US5966991>.
- [12] L. Campos, F. Bourbonnais, I. A. Bonev and P. Bigras. Development of a Five-Bar parallel robot with large workspace. Presented at ASME 2010 International Design Engineering Technical Conferences and Computers and Information in E

- ngineering Conference, IDETC/CIE2010, August 15, 2010 - August 18. 2010, Available: <http://dx.doi.org/10.1115/DETC2010-28962>. DOI: 10.1115/DETC2010-28962.
- [13] S. L. T. Automatic analyzing apparatus. 1959. Available: <http://www.google.ca/patents/US2879141>.
- [14] F. P. Lees. Loss Prevention in the Process Industries: Hazard Identification, Assessment, and Control 1996 Available: <https://books.google.ca/books?id=Af7ajgEACAAJ>.
- [15] S. Cinquemani, H. Giberti and M. Bassetti. Optimal design, simulation and experimental tests of a 5R PKM manipulator. Presented at Mechatronics (ICM), 2013 IEEE International Conference on. 2013, DOI: 10.1109/ICMECH.2013.6518575.
- [16] Critchlow, A. J. (1985). Introduction to robotics (pp. 78-87). New York: Macmillan.
- [17] F. G. Chesley and D. G. Jelatis. Remote control crane system. 1967. Available: <https://www.google.com/patents/US3344933>.
- [18] EPSON Robots company. Available: <http://robots.epson.com/product-detail/16>
- [19] Niku, S. B. (2011). Introduction to Robotics. RIA Safety & Compliance. (n.d.). Retrieved 12 14, 2012, from Robotics Online: <http://www.robotics.org/robotic-content.cfm?id=23>
- [20] KUKA Robots Company. Available: http://www.kuka-robotics.com/res/sps/f776ebab-f613-4818-9feb-527612db8dc4_pf0057_kr_10_scara_en.pdf
- [21] Toshiba Machine. Available: <http://www.toshiba-machine.co.jp/en/product/robot/case/case01.html>
- [22] Deutsches Museum. Available: https://en.wikipedia.org/wiki/Programmable_Universal_Machine_for_Assembly
- [23] PUMA 500. Available: <http://rutherford-robotics.com/PUMA/>
- [24] T. Hamada, K. Sugimoto, H. Kusakawa, T. Jinriki and K. Koizumi. Industrial robot. 1986. Available: <https://www.google.com/patents/US4610598>.
- [25] H. Makino. Assembly robot. 1982. Available: <http://www.google.com/patents/US4341502>.

- [26] L. Campos, F. Bourbonnais, I. A. Bonev and P. Bigras. Development of a Five-Bar parallel robot with large workspace. Presented at ASME 2010 International Design Engineering Technical Conferences and Computers and Information in Engineering Conference, IDETC/CIE2010, August 15, 2010 - August 18, 2010, Available: <http://dx.doi.org/10.1115/DETC2010-28962>. DOI: 10.1115/DETC2010-28962.
- [27] A. Joubair, M. Slamani and I. A. Bonev. Kinematic calibration of a Five-Bar planar parallel robot using all working modes. *Robot. Comput. Integrated Manuf.* 29(4), pp. 15-25. 2013. Available: <http://dx.doi.org/10.1016/j.rcim.2012.10.002>. DOI: 10.1016/j.rcim.2012.10.002.
- [28] B. Dasgupta and P. Choudhury. General strategy based on the newton-euler approach for the dynamic formulation of parallel manipulators. *Mechanism and Machine Theory* 34(6), pp. 801-824. 1999. Available: [http://dx.doi.org/10.1016/S0094-114X\(98\)00081-0](http://dx.doi.org/10.1016/S0094-114X(98)00081-0). DOI:10.1016/S0094-114X(98)00081-0.
- [29] P. Ouyang, Q. Li and W. Zhang. Integrated design of robotic mechanisms for force balancing and trajectory tracking. *Mechatronics* 13(8), pp. 887-905. 2003.
- [30] H. Yu. Modeling and control of hybrid machine systems—a Five-Bar mechanism case. *International Journal of Automation and Computing* 3(3), pp. 235-243. 2006.
- [31] F. Ghorbel, O. Chetelat and R. Longchamp. A reduced model for constrained rigid bodies with application to parallel robots. Presented at IFAC Symposium on Robot Control, September 1994.
- [32] P. C. Fishburn. Additive utilities with incomplete product sets: Application to priorities and assignments. *Oper. Res.* 15(3), pp. 537-542. 1967. Available: <http://www.jstor.org/stable/168461>.
- [33] L. Cheng, Y. Z. Lin, Z. G. Hou, M. Tan, J. Huang and W. J. Zhang. Adaptive tracking control of hybrid machines: A closed-chain Five-Bar mechanism case. *Mechatronics, IEEE/ASME Transactions on* 16(6), pp. 1155-1163. 2011. DOI: 10.1109/TMECH.2010.2083680.
- [34] L. W. Tsai. *Robot Analysis: The Mechanics of Serial and Parallel Manipulators* 1999 Available: https://books.google.ca/books?id=PK_N9aFZ3ccC.

- [35] Z. Huang, Q. Li and H. Ding. Theory of Parallel Mechanisms 2012 Available: https://books.google.ca/books?id=zsRAS6S5_vQC.
- [36] X. Liu, J. Wang and G. Pritschow. Kinematics, singularity and workspace of planar 5R symmetrical parallel mechanisms. Mechanism and Machine Theory 41(2), pp. 145-169. 2006. . DOI: <http://dx.doi.org/10.1016/j.mechmachtheory.2005.05.004>.
- [37] J. Jesus Cervantes-Sanchez, J. Cesar Hernandez-Rodriguez and J. Angeles. On the kinematic design of the 5R planar, symmetric manipulator. Mechanism and Machine Theory 36(11-12), pp. 1301-1313. 2001. Available: [http://dx.doi.org/10.1016/S0094-114X\(01\)00053-2](http://dx.doi.org/10.1016/S0094-114X(01)00053-2). DOI: 10.1016/S0094-114X(01)00053-2.
- [38] C. Gosselin and J. Angeles. Singularity analysis of closed-loop kinematic chains. Robotics and Automation, IEEE Transactions on 6(3), pp. 281-290. 1990. DOI: 10.1109/70.56660.
- [39] J. P. Merlet. Parallel Robots 2012 Available: <https://books.google.ca/books?id=GydrCQAAQBAJ>.
- [40] H. M. Paynter, Analysis and design of engineering systems, The M.I.T. Press, Boston, 1961 ISBN 0-262-16004-8.
- [41] D. Karnopp, D. L. Margolis and R. C. Rosenberg. System Dynamics: A Unified Approach. 1990. Available: <http://books.google.ca/books?id=EHZRAAAAMAAJ>.
- [42] D. Karnopp, D. L. Margolis. Analysis and simulation of planar mechanism systems using bond graphs. J Mech Des, Trans ASME. 1979;101(2):187-191.
- [43] A. Zeid. Bond graph modeling of planar mechanisms with realistic joint effects. Journal of Dynamic Systems, Measurement and Control, Transactions of the ASME. 1989;111(1):15-23.
- [44] D. Karnopp and R. C. Rosenberg, Analysis and Simulation of Multiport Systems - The Bond Graph Approach to Physical System Dynamics. MIT Press, Cambridge, MA, 1968.
- [45] S. Jian, C. Yin, L. Rolland and L. James. Five-Bar planar manipulator simulation and analysis by bond graph. Presented at ASME 2014 International Mechanical Engineering Congress and Exposition, IMECE 2014, November 14, 2014 - November 20. 2014, Available: <http://dx.doi.org/10.1115/IMECE2014-37602>.

DOI: 10.1115/IMECE2014-37602.

- [46] D. Karnopp, Energetically consistent bond graph models in electromechanical energy conversion. Journal of the Franklin Institute. 1990;327(5):677-686. [http://dx.doi.org/10.1016/0016-0032\(90\)90076-U](http://dx.doi.org/10.1016/0016-0032(90)90076-U). doi: 10.1016/0016-0032(90)90076-U.
- [47] D. Karnopp, Approach to derivative causality in bond graph models of mechanical systems. Journal of the Franklin Institute. 1992;329(1):65-75. [http://dx.doi.org/10.1016/0016-0032\(92\)90096-Y](http://dx.doi.org/10.1016/0016-0032(92)90096-Y). doi: 10.1016/0016-0032(92)90096-Y.
- [48] T. Ersal, J. L. Stein and L. S. Louca. A bond graph based modular modeling approach towards an automated modeling environment for reconfigurable machine tools. Proceedings of IMAACA 42004.
- [49] PID Controller Types. Available: http://www.20sim.com/webhelp/library_signal_control_pid_control_pidcontrollertypes.php
- [50] SINIOKOKO LM-P5H Datasheet. Available: http://www.phidgets.com/documentation/Phidgets/3545_0_Datasheet.pdf
- [51] SKF Rating Life. Available: <http://www.skf.com/group/products/bearings-units-housings/roller-bearings/principles/selecting-bearing-size/using-life-equations/skf-rating-life/index.html>
- [52] TDK-Lambda SWS300A series datasheet. Available: http://www.tdk-lambda.com/products/sps/ps_unit/sws/pdf/sws300a_spc.pdf
- [53] 5V 2A switching power supply. Available: <https://www.adafruit.com/products/276>
- [54] Avago Technologies. HEDM-55xx560x-Quick-Assembly-Two-and-Three-Channel-Optical-Encoders Datasheet. Available: <http://www.avagotech.com/docs/AV02-1046EN>
- [55] J. G. Ziegler and N. B. Nichols. Optimum settings for automatic controllers. Trans.ASME 64(11), 1942.
- [56] Hägglund T, Åström K J. Automatic tuning of PID controllers[J]. The control handbook, 1996: 817-826.
- [57] A. Gibb (Ed.) Building Open Source Hardware: DIY Manufacturing for Hacke

- rs and Makers, Addison-Wesley: New York, pp. 253-277 (2015).
- [58] D. Molloy. Exploring BeagleBone: Tools and Techniques for Building with Embedded Linux 2014 Available: <https://books.google.ca/books?id=RoXVoAEACAAJ>.
 - [59] C. Gerald. BeagleBone Black System Reference Manual. Revision C.1. 2014 Available: http://elinux.org/Beagleboard:BeagleBoneBlack#Hardware_Files
 - [60] Future Technology Devices International Limited (FTDI) TTL-232R-3V3 Datasheet. Available: http://www.ftdichip.com/Support/Documents/DataSheets/Cables/D_S_TTL-232R_CABLES.pdf
 - [61] MICROCHIP. dsPIC33FJ32MC304 Data Sheet, 2012 Available: <http://www.microchip.com/wwwproducts/Devices.aspx?product=dsPIC33FJ32MC304>
 - [62] P. Tan. Dual Motor Controller CAPE (DMCC) Mk. 7. Available: <http://exadler.myshopify.com/products/dual-motor-controller-cape-dmcc-mk-6>
 - [63] Wikipedia. PID Controller. Available: https://en.wikipedia.org/wiki/PID_controller#Alternative_nomenclature_and_PID_forms

10. APPENDIX

10.1. Jacobian Matrix Solutions

$$\begin{aligned}
 J_{F11} &= \frac{\partial f_1(q_1, q_2)}{\partial q_1} = \\
 &-L_1 \sin(q_1) + \frac{1}{2} \left((2 (L_5 + L_2 \cos(q_2) - L_1 \cos(q_1)) L_1 \sin(q_1) - 2 (L_2 \sin(q_2) \right. \\
 &- L_1 \sin(q_1)) L_1 \cos(q_1)) (L_5 + L_2 \cos(q_2) - L_1 \cos(q_1)) \Big) / \left((L_5 + L_2 \cos(q_2) \right. \\
 &- L_1 \cos(q_1))^2 + (L_2 \sin(q_2) - L_1 \sin(q_1))^2 \Big) - \frac{1}{2} \left((L_3^2 - L_4^2 + (L_5 + L_2 \cos(q_2) \right. \\
 &- L_1 \cos(q_1))^2 + (L_2 \sin(q_2) - L_1 \sin(q_1))^2 \Big) (L_5 + L_2 \cos(q_2) - L_1 \cos(q_1)) (2 (L_5 \\
 &+ L_2 \cos(q_2) - L_1 \cos(q_1)) L_1 \sin(q_1) - 2 (L_2 \sin(q_2) - L_1 \sin(q_1)) L_1 \cos(q_1)) \Big) \\
 &/ \left((L_5 + L_2 \cos(q_2) - L_1 \cos(q_1))^2 + (L_2 \sin(q_2) - L_1 \sin(q_1))^2 \right)^2 \\
 &+ \frac{1}{2} \left((L_3^2 - L_4^2 + (L_5 + L_2 \cos(q_2) - L_1 \cos(q_1))^2 + (L_2 \sin(q_2) \right. \\
 &- L_1 \sin(q_1))^2 \Big) L_1 \sin(q_1) \Big) / \left((L_5 + L_2 \cos(q_2) - L_1 \cos(q_1))^2 + (L_2 \sin(q_2) \right.
 \end{aligned}$$

$$\begin{aligned}
& -L_1 \sin(q_1))^2) - \frac{1}{4} \left((L_2 \sin(q_2) - L_1 \sin(q_1)) \left(-2 (L_3^2 - L_4^2 + (L_5 \right. \right. \\
& + L_2 \cos(q_2) - L_1 \cos(q_1))^2 + (L_2 \sin(q_2) - L_1 \sin(q_1))^2) (2 (L_5 + L_2 \cos(q_2) \\
& - L_1 \cos(q_1)) L_1 \sin(q_1) - 2 (L_2 \sin(q_2) - L_1 \sin(q_1)) L_1 \cos(q_1)) \Big) / \Big((L_5 \\
& + L_2 \cos(q_2) - L_1 \cos(q_1))^2 + (L_2 \sin(q_2) - L_1 \sin(q_1))^2 \Big) + \Big((L_3^2 - L_4^2 + (L_5 + L_2 \cos(q_2) \\
& - L_1 \sin(q_1)) L_1 \cos(q_1)) \Big) / \Big((L_5 + L_2 \cos(q_2) - L_1 \cos(q_1))^2 + (L_2 \sin(q_2) \\
& - L_1 \sin(q_1))^2)^2 \Big) \Big) / \\
& \left(\sqrt{4 L_3^2 - \frac{(L_3^2 - L_4^2 + (L_5 + L_2 \cos(q_2) - L_1 \cos(q_1))^2 + (L_2 \sin(q_2) - L_1 \sin(q_1))^2)^2}{(L_5 + L_2 \cos(q_2) - L_1 \cos(q_1))^2 + (L_2 \sin(q_2) - L_1 \sin(q_1))^2}} \right. \\
& \left. \sqrt{(L_5 + L_2 \cos(q_2) - L_1 \cos(q_1))^2 + (L_2 \sin(q_2) - L_1 \sin(q_1))^2} \right)
\end{aligned}$$

$$\begin{aligned}
& \sqrt{4 L_3^2 - \frac{(L_3^2 - L_4^2 + (L_5 + L_2 \cos(q_2) - L_1 \cos(q_1))^2 + (L_2 \sin(q_2) - L_1 \sin(q_1))^2)^2}{(L_5 + L_2 \cos(q_2) - L_1 \cos(q_1))^2 + (L_2 \sin(q_2) - L_1 \sin(q_1))^2}} \\
& (L_2 \sin(q_2) - L_1 \sin(q_1)) (2 (L_5 + L_2 \cos(q_2) - L_1 \cos(q_1)) L_1 \sin(q_1) \\
& - 2 (L_2 \sin(q_2) - L_1 \sin(q_1)) L_1 \cos(q_1)) \Bigg) \Bigg/ 4 ((L_5 + L_2 \cos(q_2) - L_1 \cos(q_1))^2 \\
& + (L_2 \sin(q_2) - L_1 \sin(q_1))^2)^{3/2} + \\
& \sqrt{4 L_3^2 - \frac{(L_3^2 - L_4^2 + (L_5 + L_2 \cos(q_2) - L_1 \cos(q_1))^2 + (L_2 \sin(q_2) - L_1 \sin(q_1))^2)^2}{(L_5 + L_2 \cos(q_2) - L_1 \cos(q_1))^2 + (L_2 \sin(q_2) - L_1 \sin(q_1))^2}} \\
& L_1 \cos(q_1) \Bigg) \Bigg/ 2 \sqrt{(L_5 + L_2 \cos(q_2) - L_1 \cos(q_1))^2 + (L_2 \sin(q_2) - L_1 \sin(q_1))^2}
\end{aligned}$$

$$\begin{aligned}
J_{F12} &= \frac{\partial f_1(q_1, q_2)}{\partial q_2} = \\
&\frac{1}{2} \left((-2 (L_5 + L_2 \cos(q_2) - L_1 \cos(q_1)) L_2 \sin(q_2) + 2 (L_2 \sin(q_2) \right. \\
&\quad \left. - L_1 \sin(q_1)) L_2 \cos(q_2)) (L_5 + L_2 \cos(q_2) - L_1 \cos(q_1)) \right) / \left((L_5 + L_2 \cos(q_2) \right. \\
&\quad \left. - L_1 \cos(q_1))^2 + (L_2 \sin(q_2) - L_1 \sin(q_1))^2 \right) - \frac{1}{2} \left((L_3^2 - L_4^2 + (L_5 + L_2 \cos(q_2) \right. \\
&\quad \left. - L_1 \cos(q_1))^2 + (L_2 \sin(q_2) - L_1 \sin(q_1))^2 \right) (L_5 + L_2 \cos(q_2) - L_1 \cos(q_1)) (\\
&\quad \left. - 2 (L_5 + L_2 \cos(q_2) - L_1 \cos(q_1)) L_2 \sin(q_2) + 2 (L_2 \sin(q_2) \right. \\
&\quad \left. - L_1 \sin(q_1)) L_2 \cos(q_2)) \right) / \left((L_5 + L_2 \cos(q_2) - L_1 \cos(q_1))^2 + (L_2 \sin(q_2) \right. \\
&\quad \left. - L_1 \sin(q_1))^2 \right)^2 - \frac{1}{2} \left((L_3^2 - L_4^2 + (L_5 + L_2 \cos(q_2) - L_1 \cos(q_1))^2 + (L_2 \sin(q_2) \right. \\
&\quad \left. - L_1 \sin(q_1))^2 \right) L_2 \sin(q_2) \right) / \left((L_5 + L_2 \cos(q_2) - L_1 \cos(q_1))^2 + (L_2 \sin(q_2) \right. \\
&\quad \left. - L_1 \sin(q_1))^2 \right) - \frac{1}{4} \left((L_2 \sin(q_2) - L_1 \sin(q_1)) \left[- (2 (L_3^2 - L_4^2 + (L_5 \right. \right.
\end{aligned}$$

$$\begin{aligned}
& + L_2 \cos(q_2) - L_1 \cos(q_1))^2 + (L_2 \sin(q_2) - L_1 \sin(q_1))^2) \left(-2 (L_5 + L_2 \cos(q_2) \right. \\
& \left. - L_1 \cos(q_1)) L_2 \sin(q_2) + 2 (L_2 \sin(q_2) - L_1 \sin(q_1)) L_2 \cos(q_2)) \right) / \left((L_5 \right. \\
& \left. + L_2 \cos(q_2) - L_1 \cos(q_1))^2 + (L_2 \sin(q_2) - L_1 \sin(q_1))^2 \right) + \left((L_3^2 - L_4^2 + (L_5 + L_2 \cos(q_2) \right. \\
& \left. - L_1 \sin(q_1)) L_2 \cos(q_2)) \right) / \left((L_5 + L_2 \cos(q_2) - L_1 \cos(q_1))^2 + (L_2 \sin(q_2) \right. \\
& \left. - L_1 \sin(q_1))^2)^2 \right) \Bigg) / \\
& \left(\sqrt{4 L_3^2 - \frac{(L_3^2 - L_4^2 + (L_5 + L_2 \cos(q_2) - L_1 \cos(q_1))^2 + (L_2 \sin(q_2) - L_1 \sin(q_1))^2)^2}{(L_5 + L_2 \cos(q_2) - L_1 \cos(q_1))^2 + (L_2 \sin(q_2) - L_1 \sin(q_1))^2}} \right. \\
& \left. \sqrt{(L_5 + L_2 \cos(q_2) - L_1 \cos(q_1))^2 + (L_2 \sin(q_2) - L_1 \sin(q_1))^2} \right) \\
& + \frac{1}{4} \left(\sqrt{4 L_3^2 - \frac{(L_3^2 - L_4^2 + (L_5 + L_2 \cos(q_2) - L_1 \cos(q_1))^2 + (L_2 \sin(q_2) - L_1 \sin(q_1))^2)^2}{(L_5 + L_2 \cos(q_2) - L_1 \cos(q_1))^2 + (L_2 \sin(q_2) - L_1 \sin(q_1))^2}} \right.
\end{aligned}$$

$$\begin{aligned}
& (L_2 \sin(q_2) - L_1 \sin(q_1)) (-2 (L_5 + L_2 \cos(q_2) - L_1 \cos(q_1)) L_2 \sin(q_2) \\
& + 2 (L_2 \sin(q_2) - L_1 \sin(q_1)) L_2 \cos(q_2)) \Bigg) \Bigg/ \left((L_5 + L_2 \cos(q_2) - L_1 \cos(q_1))^2 \right. \\
& \left. + (L_2 \sin(q_2) - L_1 \sin(q_1))^2 \right)^{3/2} \\
& - \frac{1}{2} \left(\sqrt{4 L_3^2 - \frac{(L_3^2 - L_4^2 + (L_5 + L_2 \cos(q_2) - L_1 \cos(q_1))^2 + (L_2 \sin(q_2) - L_1 \sin(q_1))^2)^2}{(L_5 + L_2 \cos(q_2) - L_1 \cos(q_1))^2 + (L_2 \sin(q_2) - L_1 \sin(q_1))^2}} \right. \\
& \left. L_2 \cos(q_2) \right) \Bigg/ \sqrt{(L_5 + L_2 \cos(q_2) - L_1 \cos(q_1))^2 + (L_2 \sin(q_2) - L_1 \sin(q_1))^2}
\end{aligned}$$

$$\begin{aligned}
J_{F21} &= \frac{\partial f_2(q_1, q_2)}{\partial q_1} = \\
& L_1 \cos(q_1) + \frac{1}{2} \left((2 (L_5 + L_2 \cos(q_2) - L_1 \cos(q_1)) L_1 \sin(q_1) - 2 (L_2 \sin(q_2) \right. \\
& \left. - L_1 \sin(q_1)) L_1 \cos(q_1)) (L_2 \sin(q_2) - L_1 \sin(q_1)) \right) / \left((L_5 + L_2 \cos(q_2) \right. \\
& \left. - L_1 \cos(q_1))^2 + (L_2 \sin(q_2) - L_1 \sin(q_1))^2 \right) - \frac{1}{2} \left((L_3^2 - L_4^2 + (L_5 + L_2 \cos(q_2) \right. \\
& \left. - L_1 \cos(q_1))^2 + (L_2 \sin(q_2) - L_1 \sin(q_1))^2 \right) (L_2 \sin(q_2) - L_1 \sin(q_1)) (2 (L_5 \\
& \left. + L_2 \cos(q_2) - L_1 \cos(q_1)) L_1 \sin(q_1) - 2 (L_2 \sin(q_2) - L_1 \sin(q_1)) L_1 \cos(q_1)) \right) \\
& / \left((L_5 + L_2 \cos(q_2) - L_1 \cos(q_1))^2 + (L_2 \sin(q_2) - L_1 \sin(q_1))^2 \right)^2 \\
& - \frac{1}{2} \left((L_3^2 - L_4^2 + (L_5 + L_2 \cos(q_2) - L_1 \cos(q_1))^2 + (L_2 \sin(q_2) \right. \\
& \left. - L_1 \sin(q_1))^2 \right) L_1 \cos(q_1) \right) / \left((L_5 + L_2 \cos(q_2) - L_1 \cos(q_1))^2 + (L_2 \sin(q_2) \right. \\
& \left. - L_1 \sin(q_1))^2 \right) + \frac{1}{4} \left((L_5 + L_2 \cos(q_2) - L_1 \cos(q_1)) \left(- (2 (L_3^2 - L_4^2 + (L_5 \right. \right. \\
& \left. \left. + L_2 \cos(q_2) - L_1 \cos(q_1))^2 + (L_2 \sin(q_2) - L_1 \sin(q_1))^2 \right) (2 (L_5 + L_2 \cos(q_2) \right.
\end{aligned}$$

$$\begin{aligned}
& -L_1 \cos(q_1)) L_1 \sin(q_1) - 2 (L_2 \sin(q_2) - L_1 \sin(q_1)) L_1 \cos(q_1)) \Big) / \Big((L_5 \\
& + L_2 \cos(q_2) - L_1 \cos(q_1))^2 + (L_2 \sin(q_2) - L_1 \sin(q_1))^2 \Big) + \Big((L_3^2 - L_4^2 + (L_5 + L_2 \cos(q_2) \\
& - L_1 \sin(q_1)) L_1 \cos(q_1)) \Big) / \Big((L_5 + L_2 \cos(q_2) - L_1 \cos(q_1))^2 + (L_2 \sin(q_2) \\
& - L_1 \sin(q_1))^2 \Big) \Big) / \\
& \Big(\sqrt{4 L_3^2 - \frac{(L_3^2 - L_4^2 + (L_5 + L_2 \cos(q_2) - L_1 \cos(q_1))^2 + (L_2 \sin(q_2) - L_1 \sin(q_1))^2)^2}{(L_5 + L_2 \cos(q_2) - L_1 \cos(q_1))^2 + (L_2 \sin(q_2) - L_1 \sin(q_1))^2}} \\
& \sqrt{(L_5 + L_2 \cos(q_2) - L_1 \cos(q_1))^2 + (L_2 \sin(q_2) - L_1 \sin(q_1))^2}} \Big) \\
& - \frac{1}{4} \Big(\sqrt{4 L_3^2 - \frac{(L_3^2 - L_4^2 + (L_5 + L_2 \cos(q_2) - L_1 \cos(q_1))^2 + (L_2 \sin(q_2) - L_1 \sin(q_1))^2)^2}{(L_5 + L_2 \cos(q_2) - L_1 \cos(q_1))^2 + (L_2 \sin(q_2) - L_1 \sin(q_1))^2}} \\
& (L_5 + L_2 \cos(q_2) - L_1 \cos(q_1)) (2 (L_5 + L_2 \cos(q_2) - L_1 \cos(q_1)) L_1 \sin(q_1)
\end{aligned}$$

$$\begin{aligned}
& -2 \left(L_2 \sin(q_2) - L_1 \sin(q_1) \right) L_1 \cos(q_1) \Big) \Big/ \left(\left(L_5 + L_2 \cos(q_2) - L_1 \cos(q_1) \right)^2 \right. \\
& \left. + \left(L_2 \sin(q_2) - L_1 \sin(q_1) \right)^2 \right)^{3/2} \\
& + \frac{1}{2} \left(\sqrt{4 L_3^2 - \frac{\left(L_3^2 - L_4^2 + \left(L_5 + L_2 \cos(q_2) - L_1 \cos(q_1) \right)^2 + \left(L_2 \sin(q_2) - L_1 \sin(q_1) \right)^2 \right)^2}{\left(L_5 + L_2 \cos(q_2) - L_1 \cos(q_1) \right)^2 + \left(L_2 \sin(q_2) - L_1 \sin(q_1) \right)^2}} \right. \right. \\
& \left. \left. L_1 \sin(q_1) \right) \Big/ \sqrt{\left(L_5 + L_2 \cos(q_2) - L_1 \cos(q_1) \right)^2 + \left(L_2 \sin(q_2) - L_1 \sin(q_1) \right)^2}
\end{aligned}$$

$$\begin{aligned}
J_{F22} &= \frac{\partial f_2(q_1, q_2)}{\partial q_2} = \\
&\frac{1}{2} \left((-2 (L_5 + L_2 \cos(q_2) - L_1 \cos(q_1)) L_2 \sin(q_2) + 2 (L_2 \sin(q_2) \right. \\
&\quad \left. - L_1 \sin(q_1)) L_2 \cos(q_2)) (L_2 \sin(q_2) - L_1 \sin(q_1)) \right) / \left((L_5 + L_2 \cos(q_2) \right. \\
&\quad \left. - L_1 \cos(q_1))^2 + (L_2 \sin(q_2) - L_1 \sin(q_1))^2 \right) - \frac{1}{2} \left((L_3^2 - L_4^2 + (L_5 + L_2 \cos(q_2) \right. \\
&\quad \left. - L_1 \cos(q_1))^2 + (L_2 \sin(q_2) - L_1 \sin(q_1))^2 \right) (L_2 \sin(q_2) - L_1 \sin(q_1)) (-2 (L_5 \\
&\quad + L_2 \cos(q_2) - L_1 \cos(q_1)) L_2 \sin(q_2) + 2 (L_2 \sin(q_2) - L_1 \sin(q_1)) L_2 \cos(q_2)) \right) \\
&\quad / \left((L_5 + L_2 \cos(q_2) - L_1 \cos(q_1))^2 + (L_2 \sin(q_2) - L_1 \sin(q_1))^2 \right)^2 \\
&\quad + \frac{1}{2} \left((L_3^2 - L_4^2 + (L_5 + L_2 \cos(q_2) - L_1 \cos(q_1))^2 + (L_2 \sin(q_2) \right. \\
&\quad \left. - L_1 \sin(q_1))^2 \right) L_2 \cos(q_2) \right) / \left((L_5 + L_2 \cos(q_2) - L_1 \cos(q_1))^2 + (L_2 \sin(q_2) \right. \\
&\quad \left. - L_1 \sin(q_1))^2 \right) + \frac{1}{4} \left((L_5 + L_2 \cos(q_2) - L_1 \cos(q_1)) \left(-2 (L_3^2 - L_4^2 + (L_5 \right. \right. \\
&\quad \left. \left. + L_2 \cos(q_2) - L_1 \cos(q_1))^2 + (L_2 \sin(q_2) - L_1 \sin(q_1))^2 \right) (-2 (L_5 + L_2 \cos(q_2) \right.
\end{aligned}$$

$$\begin{aligned}
& -L_1 \cos(q_1)) L_2 \sin(q_2) + 2 (L_2 \sin(q_2) - L_1 \sin(q_1)) L_2 \cos(q_2)) \Big) \Big/ \Big((L_5 \\
& + L_2 \cos(q_2) - L_1 \cos(q_1))^2 + (L_2 \sin(q_2) - L_1 \sin(q_1))^2 \Big) + \Big((L_3^2 - L_4^2 + (L_5 + L_2 \cos(q_2) \\
& - L_1 \sin(q_1)) L_2 \cos(q_2)) \Big) \Big/ \Big((L_5 + L_2 \cos(q_2) - L_1 \cos(q_1))^2 + (L_2 \sin(q_2) \\
& - L_1 \sin(q_1))^2 \Big) \Big) \Big/ \\
& \Big(\sqrt{4 L_3^2 - \frac{(L_3^2 - L_4^2 + (L_5 + L_2 \cos(q_2) - L_1 \cos(q_1))^2 + (L_2 \sin(q_2) - L_1 \sin(q_1))^2)^2}{(L_5 + L_2 \cos(q_2) - L_1 \cos(q_1))^2 + (L_2 \sin(q_2) - L_1 \sin(q_1))^2}} \\
& \sqrt{(L_5 + L_2 \cos(q_2) - L_1 \cos(q_1))^2 + (L_2 \sin(q_2) - L_1 \sin(q_1))^2}} \Big) \\
& - \frac{1}{4} \Big(\sqrt{4 L_3^2 - \frac{(L_3^2 - L_4^2 + (L_5 + L_2 \cos(q_2) - L_1 \cos(q_1))^2 + (L_2 \sin(q_2) - L_1 \sin(q_1))^2)^2}{(L_5 + L_2 \cos(q_2) - L_1 \cos(q_1))^2 + (L_2 \sin(q_2) - L_1 \sin(q_1))^2}} \\
& (L_5 + L_2 \cos(q_2) - L_1 \cos(q_1)) (-2 (L_5 + L_2 \cos(q_2) - L_1 \cos(q_1)) L_2 \sin(q_2)
\end{aligned}$$

$$\begin{aligned}
& + 2 \left(L_2 \sin(q_2) - L_1 \sin(q_1) \right) L_2 \cos(q_2) \Big) \Big/ \left(\left(L_5 + L_2 \cos(q_2) - L_1 \cos(q_1) \right)^2 \right. \\
& + \left. \left(L_2 \sin(q_2) - L_1 \sin(q_1) \right)^2 \right)^{3/2} \\
& - \frac{1}{2} \left(\sqrt{4 L_3^2 - \frac{\left(L_3^2 - L_4^2 + \left(L_5 + L_2 \cos(q_2) - L_1 \cos(q_1) \right)^2 + \left(L_2 \sin(q_2) - L_1 \sin(q_1) \right)^2 \right)^2}{\left(L_5 + L_2 \cos(q_2) - L_1 \cos(q_1) \right)^2 + \left(L_2 \sin(q_2) - L_1 \sin(q_1) \right)^2}} \right. \\
& \left. \left. L_2 \sin(q_2) \right) \right) \Big/ \sqrt{\left(L_5 + L_2 \cos(q_2) - L_1 \cos(q_1) \right)^2 + \left(L_2 \sin(q_2) - L_1 \sin(q_1) \right)^2}
\end{aligned}$$

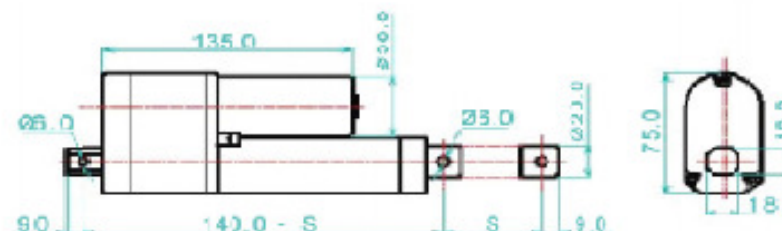
10.2. Linear Actuator LM-P5H Specifications

Main Spec:

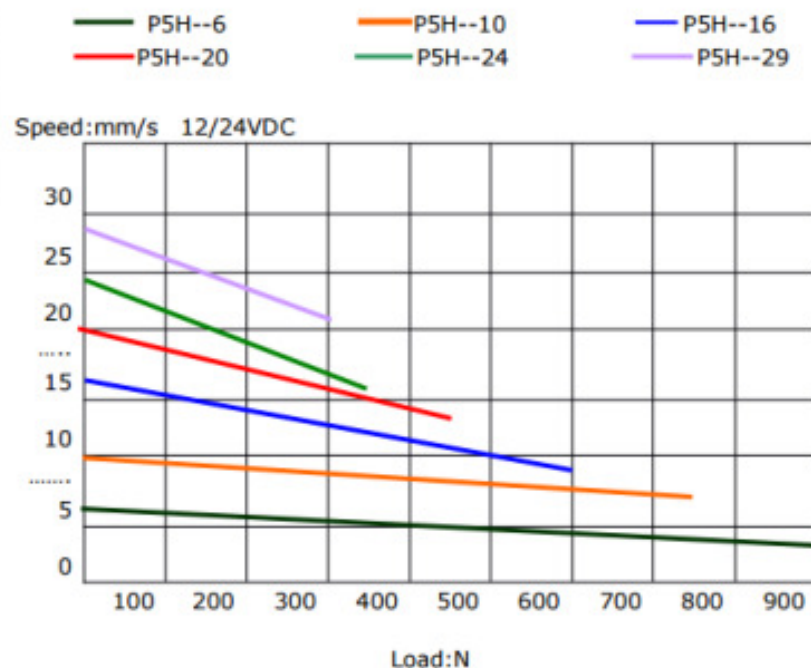
Type	LM-P5H
Input	12/24VDC
load	300~900N 30~90KG 66~198 LBS
Speed	5~29mm/s 0.24~1.16inch
Potentiometer (customize)	1KΩ,5KΩ,10KΩ
Limited switch	Built-in (not adjustable)
Duty cycle	10~15%
House	Aluminum Alloy
Inner tube	Aluminum Alloy
Stroke length(customize)	50,100,150,200,250,300mm,etc
Color	Grey/black
Operation temperature	-26℃ ~ +65℃
Safety certificate	CE

Spec:

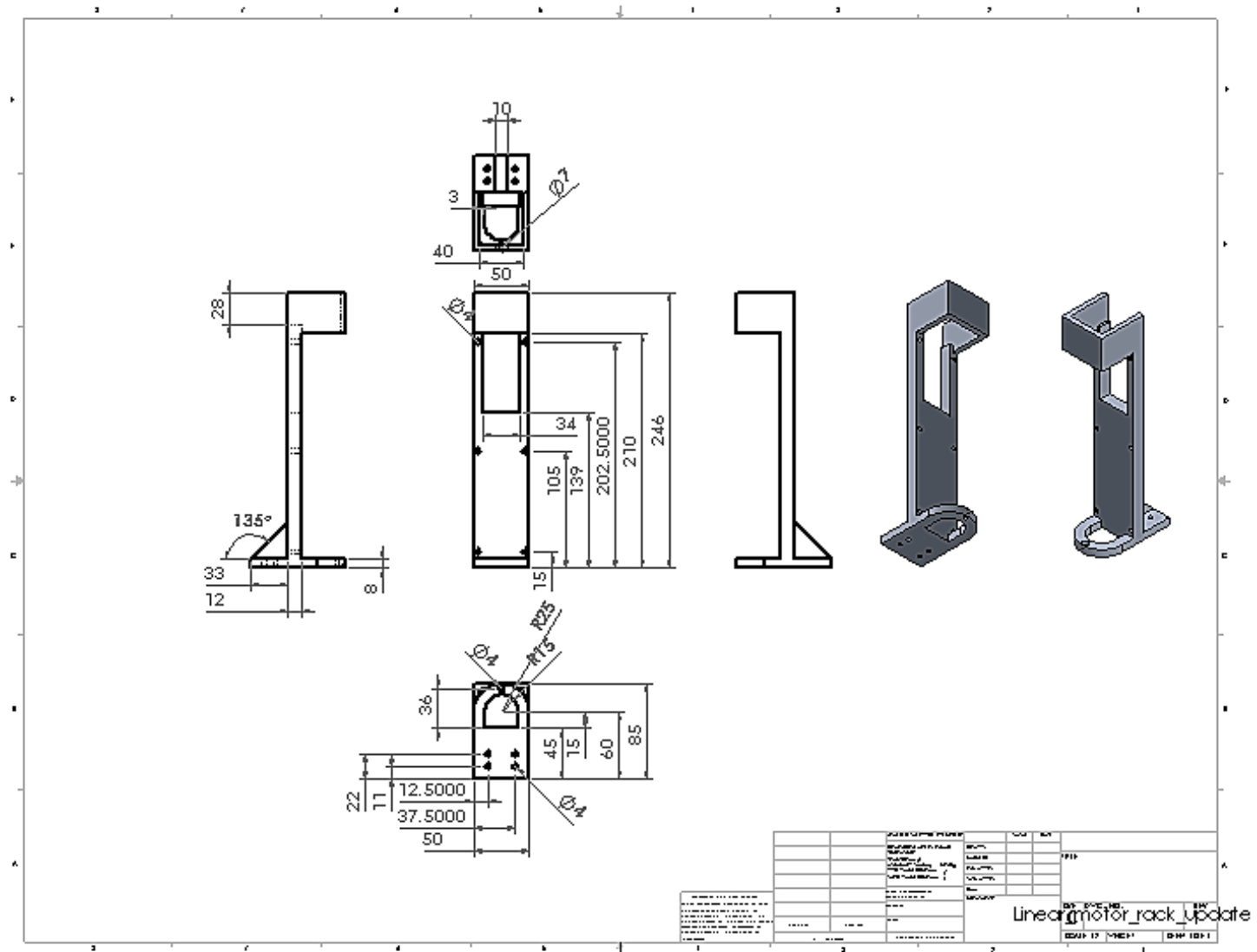
Type	Load: N	Pull: N	Static load: N	Unload/load speed:MM/S	Duty cycle:%	Max current	
						12V	24V
P5H-6	900	750	950	6/4	15	5	2.5
P5H -10	750	600	750	10/7	15	4.8	2.4
P5H -16	600	500	500	16/9	15	4.4	2.2
P5H -20	450	400	400	20/14	15	4	2
P5H -24	350	300	300	24/16	10	4	2
P5H -29	300	200	250	29/21	10	4	2



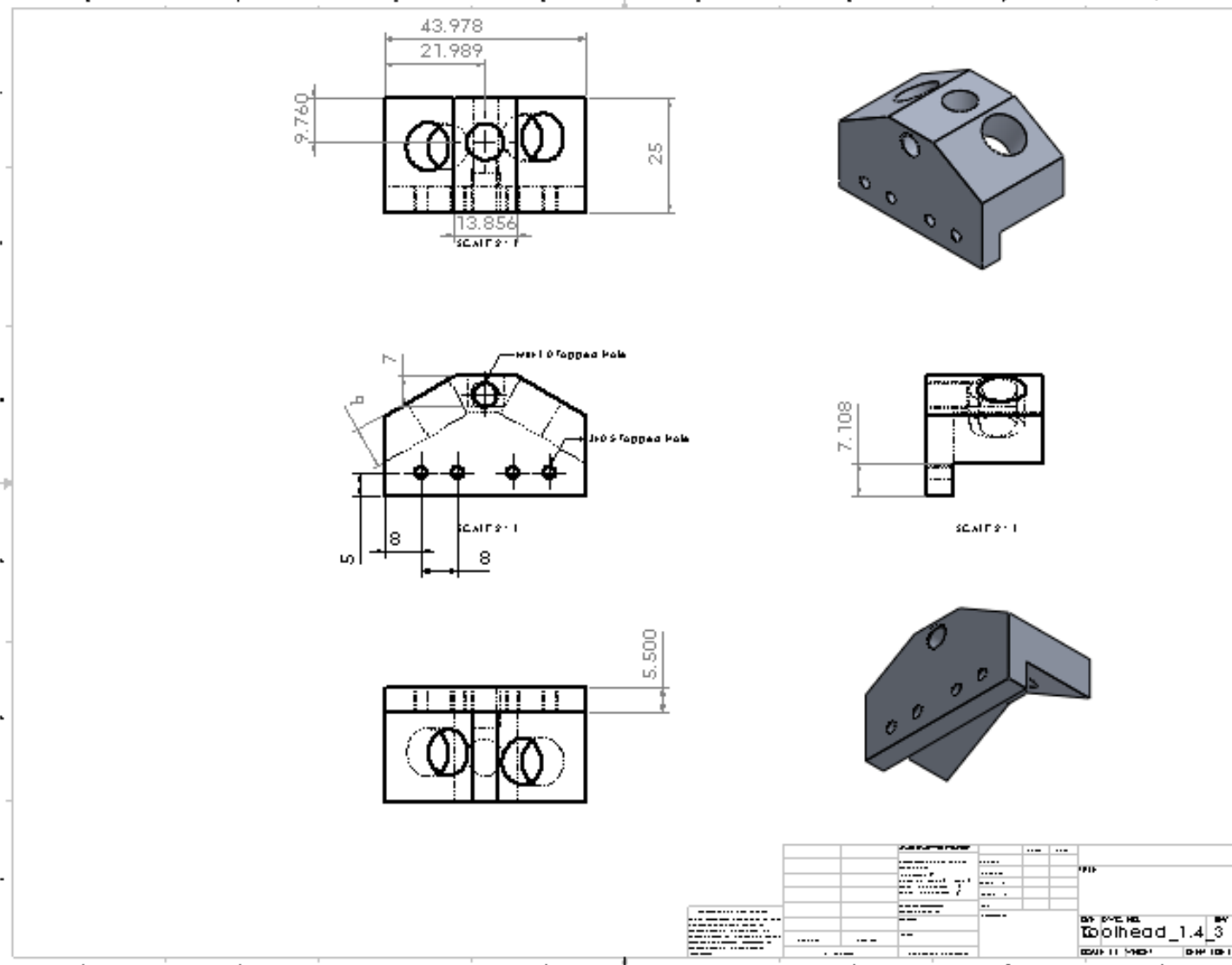
Speed vs. Load



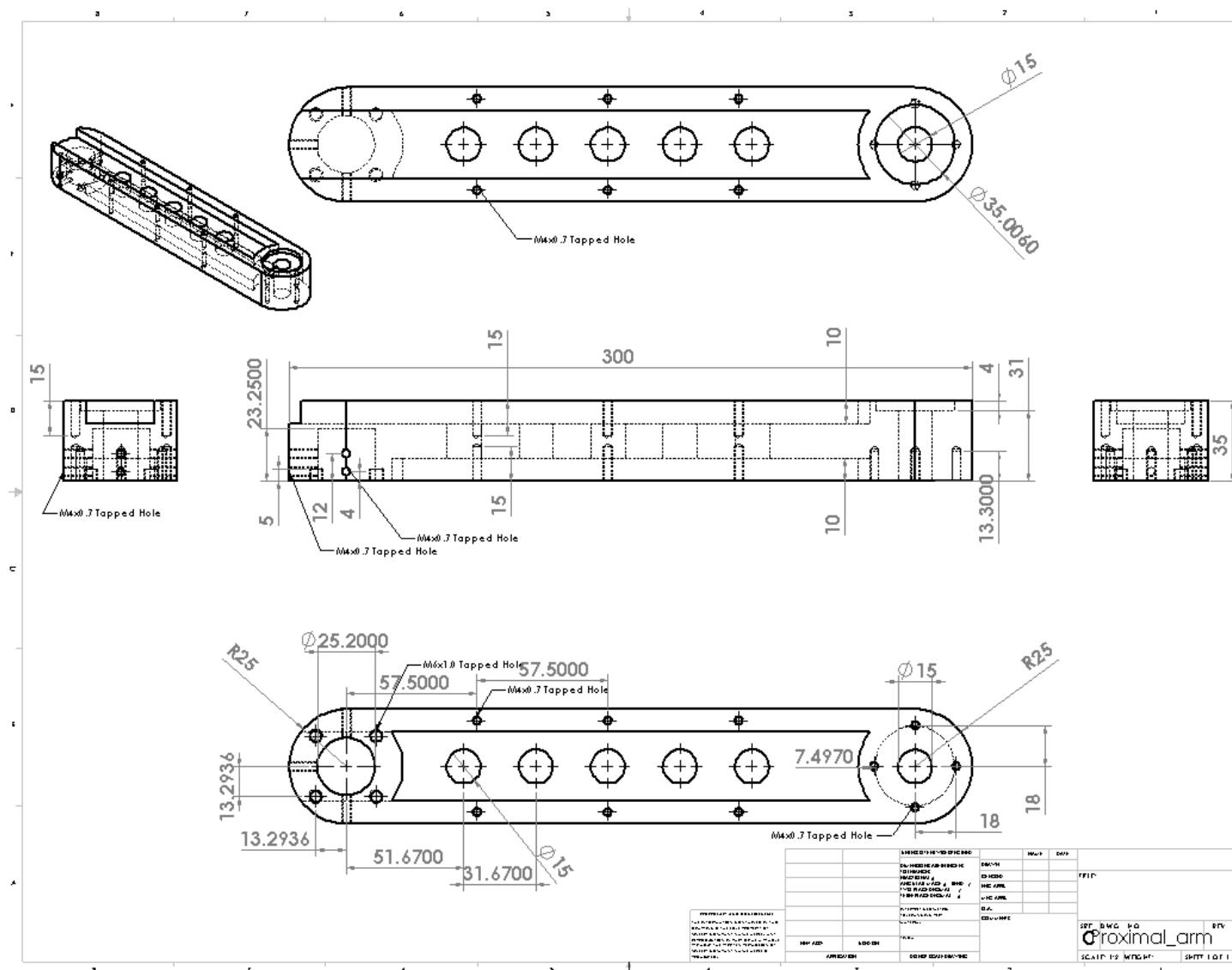
10.3. Drawing of Linear Apparatus



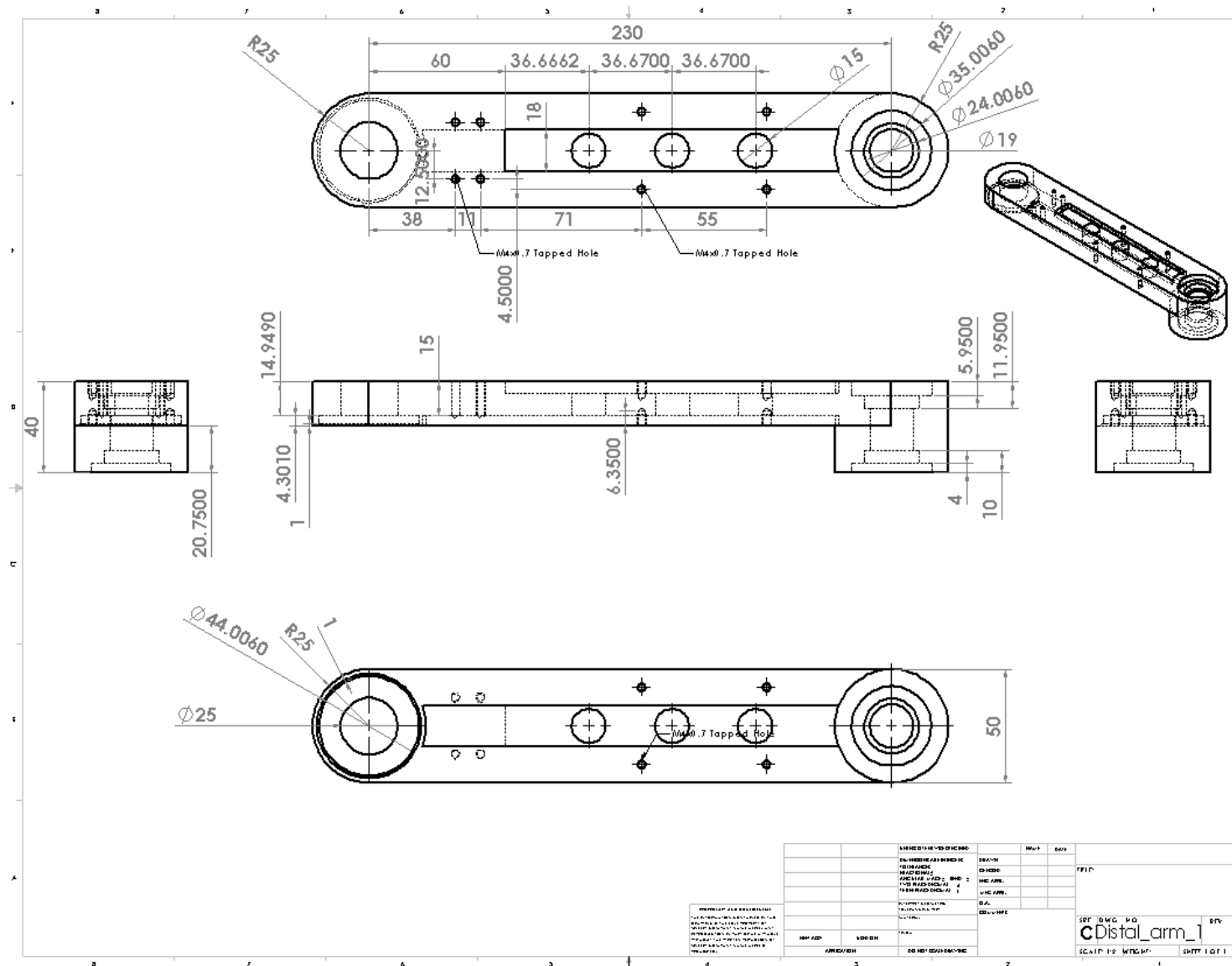
10.4. Drawing of Linear Apparatus



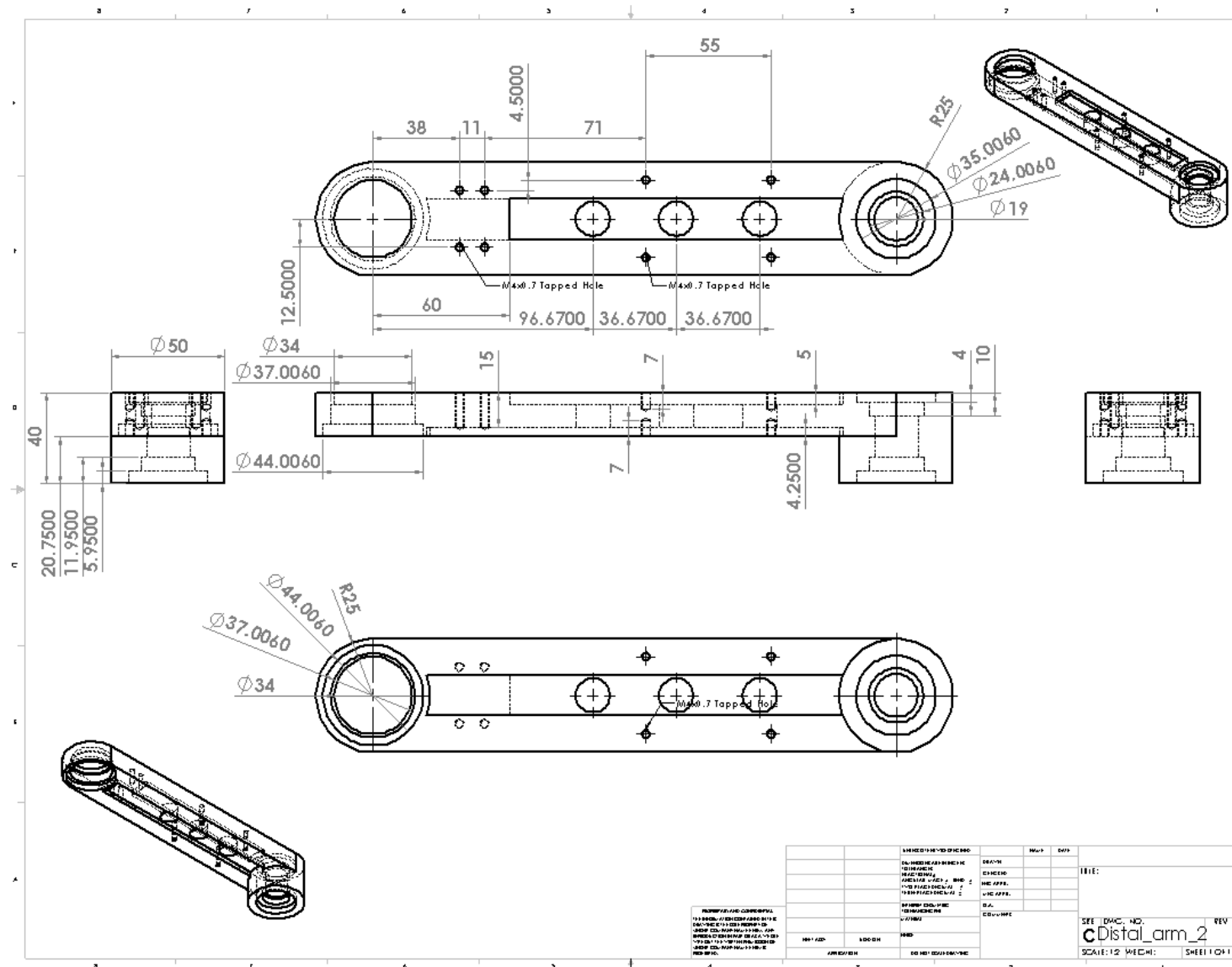
10.5. Drawing of Proximal Arm



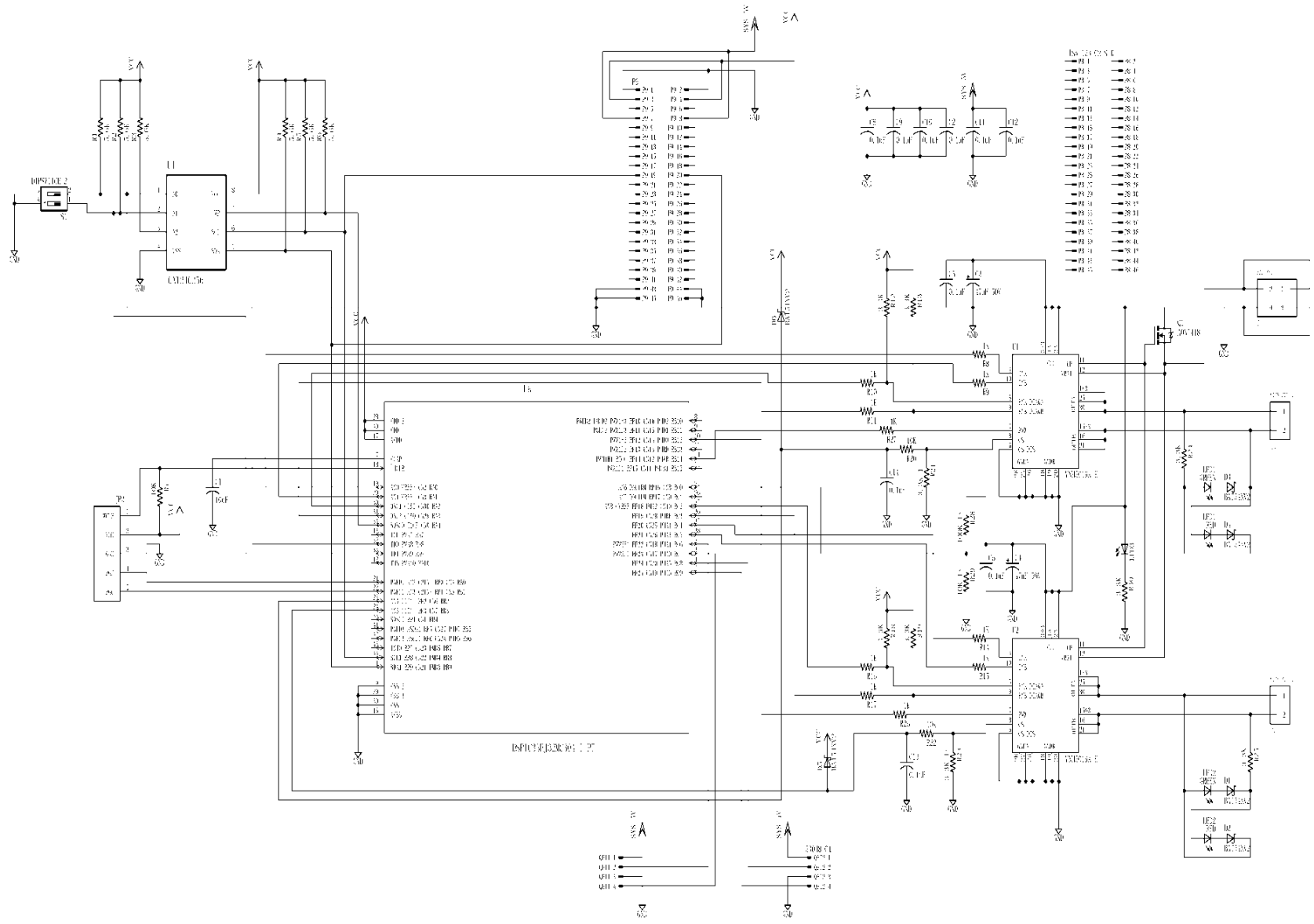
10.6. Drawing of Distal Arm One




10.7. Drawing of Distal Arm One



10.8. DMCC Schematic



10.9. Positive Test Script and Test Results

Positive Test Case for Custom Autosampler						
		Project Name/#				
		Project Manager				
		Testing Start Date				
		Testing End Date				
		Name of Tester(s)				
Test ID	Test Objective	Precondition/Data	Steps to Execute	Expected Results	Pass/Fail	Comments
ST_1.0	Turn on LED Screen	Power cord must be plugged in	Click the Power button below LED	Screen should power on	P	
ST_1.1	Open Lab GUI	Screen and controller must be connected to main computer	Double click Lab GUI program on LED screen and click execute	Lab GUI should open on main computer	P	
ST_1.2	Verify connection of controller	All connections should be made and power must be supplied	View Lab GUI display screen	Lab GUI screen should display 'CONNECT' meaning autosampler is fully connected	P	
ST_2.0	Initialize system	GUI and firmware must be open There should be no moving parts ongoing Red, yellow, and green light illuminated to show waiting for command	Click initialize button	System should begin initialization progress GUI will show 'GO TO HOME'	P	
ST_2.1	Verify system enters initialization mode	Initialize button must be pressed	View light indicating systems current mode	Light should turn yellow and green indicating system is currently undergoing initialization process	P	
ST_2.2	Verify system has successfully completed initialization		View light indicating systems current mode	Red, yellow, and green light should be on indicating the system is ready for user's command Needle should be in 'HOME' position	P	
ST_3.0	Program start time		View screen displaying program start	Correct time should be displayed once GUI is opened	P	
ST_3.1	Verify process time	Process time in seconds	View screens displaying current time and program start time	Process time should be equivalent to the difference in current time and program start time	P	
ST_4.0	Accuracy of needle	Tube rack should be fixed under the autosampler	Enter Row # and Column # (Ex. Row 5, Column 6, Time 0)	Needle should proceed to correct coordinates for each tube and be directly over the middle of each tube Green light should be illuminated to show needle has reached correct position and injection of needle should begin	P	
ST_4.1	Verify correct path of needle	Row and column number	Input the row and column number for the last tube desired to fill	Needle should start at tube in first row of first column and work its way across the row Steady yellow light illuminated while needle is in motion between each tube	P	
ST_4.2	Verify correct location of needle		View screen displaying current row and column number View light indicating systems current mode	Screen should display 'On the Way' while moving from one tube to next Green light should be illuminated once needle is in correct position over test tube Screen should display correct row and column number of the tube the needle is in	P	
ST_4.3	Set time for each tube	Time in minutes	Input an allotted time for the needle at each tube in order to achieve desired volume (Ex. Row 1, Column 1, Time 1)	Needle should stay at each tube for the amount of time the user has inputted	P	

ST_4.4	Verify time in each tube	Desired time in minutes	With a stopwatch start timing once needle is fully injected and stop once needle starts to extract	Time recorded should match inputted time	P	
ST_5.1	Manual lowering of needle	Autosampler should be in neutral status and nothing is moving	Click button to lower needle (Ex. Row 1, Column 1)	Needle should lower at end to be inside test tube	P	
ST_5.2	Manual extracting of needle	Red, yellow, and green light should be illuminated to show waiting for command	Click button to extract needle	Needle should extract from inside test tube and raise back to original position	P	
ST_6.0	Break the experiment	Program must be ongoing	Click the 'Pause' then 'Break' button	Experiment should stop and bring the needle up if it is in the test tube Red light on to show manual break experiment and motors lose power simultaneously	P	
ST_6.1	Initializing after breaking of experiment	'Break' button must have been pressed	Click initialize button	System should complete initialize process and needle should return to 'HOME' position Red, yellow, and green lights should illuminate showing waiting for user's next command	P	
ST_7.0	Termination	Experiment must have completed filling of final desired tube	View light indicating systems current mode	Red, yellow, and green light should be on indicating the system is ready for user's next command GUI shows 'STOPSAMP'	P	

Supervisor: Lesley James

Signature:

Co-Supervisor: Luc Rolland

Signature:



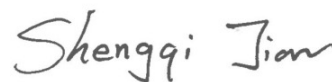
Manager: Shervin Ayazi

Signature:




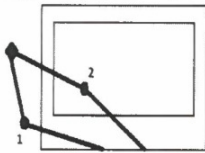
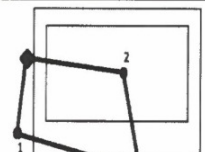
Student: Shengqi Jian

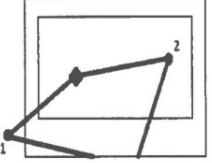
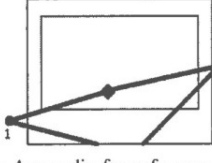
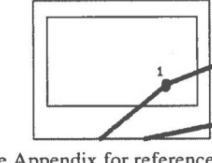
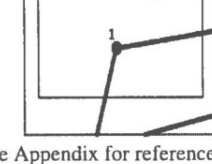
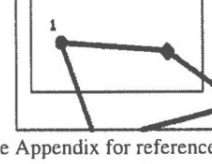
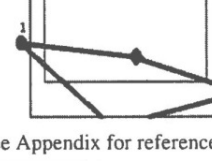
Signature:

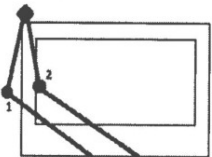
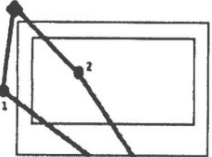
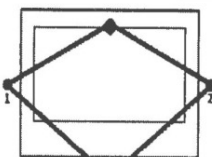
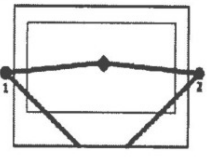
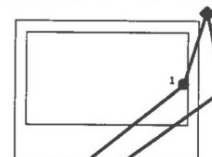
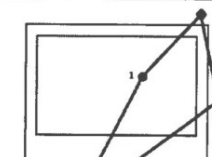


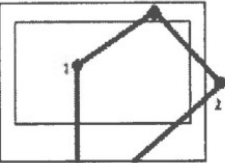
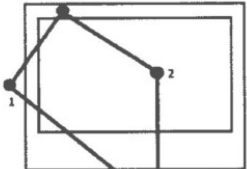
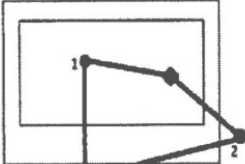
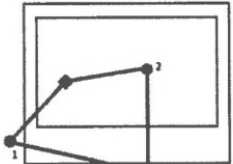
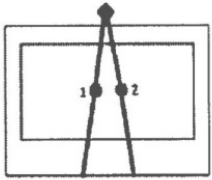
2016/May/4th

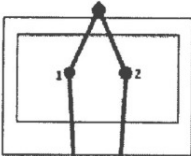
10.10. Negative Test Script and Test Results

		Negative Test Case for Custom Autosampler				
		Project Name/#				
		Project Manager				
		Testing Start Date				
		Testing End Date				
		Name of Tester(s)				
Test ID	Test Objective	Precondition/Data	Steps to Execute	Expected Results	Pass/Fail	Comments
NTC_1.0	Turn on LED Screen	Power cord must be plugged in	Click the Power button below LED screen	Screen should power on	P	
NTC_1.1	Open Lab GUI	Screen and controller must be connected to main computer	Double click Firmware program on LED screen and click execute in terminal	Lab GUI should open on main computer	P	
NTC_1.2	Verify connection of controller	All connections should be made and power must be supplied	View Lab GUI display screen	Lab GUI screen should display 'CONNECT' meaning autosampler is fully connected	P	
NTC_2.0	Initialize system from random positioning of needle inside workspace	GUI and firmware must be open There should be no moving parts ongoing	Manually position arm in any arbitrary position of choice in working space of autosampler Click initialize button on GUI screen	System should begin initialization progress GUI feedback screen will show 'GO TO HOME'	P	
NTC_2.1	Initialize system from random positioning of needle outside workspace	Red, yellow, and green light illuminated to show waiting for command	Manually position arms in any arbitrary position of choice outside working space of autosampler Click initialize button on GUI display screen	Needle should be located in 'HOME' position.	P	
NTC_2.2 (a)	Initializing with respect to position of arms in indicated picture		Manually position Arms in position shown to the left Click initialize button on GUI screen	System should begin initialization progress GUI feedback screen will show 'GO TO HOME'	P	
NTC_2.2 (b)			Manually position Arm in position shown to the left Click initialize button on GUI screen	Needle should be located in 'HOME' position.	P	

NTC_2.2 (c)	Initializing with respect to position of arms in indicated picture		Manually position Arms in position shown to the left Click initialize button on GUI screen	System should begin initialization progress GUI feedback screen will show 'GO TO HOME' Needle should be located in 'HOME' position	P	
NTC_2.2 (d)			Manually position Arms in position shown to the left Click initialize button on GUI screen		P	
NTC_2.2 (e)			Manually position Arms in position shown to the left Click initialize button on GUI screen		P	
NTC_2.2 (f)			Manually position Arms in position shown to the left Click initialize button on GUI screen		P	
NTC_2.2 (g)			Manually position Arms in position shown to the left Click initialize button on GUI screen		P	
NTC_2.2 (h)			Manually position Arms in position shown to the left Click initialize button on GUI screen		P	

NTC_2.2 (i)	Initializing with respect to position of arms in indicated picture	 See Appendix for reference	Manually position Arms in position shown to the left Click initialize button on GUI screen	System should begin initialization progress GUI feedback screen will show 'GO TO HOME' Needle should be located in 'HOME' position	P	
NTC_2.2 (j)		 See Appendix for reference	Manually position Arms in position shown to the left Click initialize button on GUI screen		P	
NTC_2.2 (k)		 See Appendix for reference	Manually position Arms in position shown to the left Click initialize button on GUI screen		P	
NTC_2.2 (l)		 See Appendix for reference	Manually position Arms in position shown to the left Click initialize button on GUI screen		P	
NTC_2.2 (m)	Initializing with respect to position of arms in indicated picture	 See Appendix for reference	Manually position Arms in position shown to the left Click initialize button on GUI screen	System should begin initialization progress GUI feedback screen will show 'GO TO HOME' Needle should be located in 'HOME' position	P	
NTC_2.2 (n)		 See Appendix for reference	Manually position Arms in position shown to the left Click initialize button on GUI screen		P	

NTC_2.2 (o)	Initializing with respect to position of arms in indicated picture		Manually position Arms in position shown to the left Click initialize button on GUI screen	System should begin initialization progress GUI feedback screen will show 'GO TO HOME'	P	
NTC_2.2 (p)			Manually position Arms in position shown to the left Click initialize button on GUI screen			
NTC_2.2 (q)	Initializing with respect to position of arms in indicated picture		Manually position Arms in position shown to the left Click initialize button on GUI screen	System should begin initialization progress GUI feedback screen will show 'GO TO HOME' Needle should be located in 'HOME' position	P	
NTC_2.2 (r)			Manually position Arms in position shown to the left Click initialize button on GUI screen			
NTC_2.2 (s)			Manually position Arms in position shown to the left Click initialize button on GUI screen			

NTC_2.2 (t)	Initializing with respect to position of arms in indicated picture	 <p>See Appendix for reference</p>	<p>Manually position Arms in position shown to the left</p> <p>Click initialize button on GUI screen</p>	<p>System should begin initialization progress</p> <p>GUI feedback screen will show 'GO TO HOME'</p> <p>Needle should be located in 'HOME' position</p>	P	
NTC_3.0	Maximum amount of tubes		Input a row or column number greater than maximum amount of tube rack (Example: ' 7 ')	User will not be able to hit the 'OK' button	P	
NTC_3.1	Minimum amount of tubes		Input a row or column number less than zero (Example: ' -1 ')	User will not be able to hit the 'OK' button	P	
NTC_3.2a	Unexpected input for defining final desired tube		Input any character besides a number for row and column number (Example: ' a ')	User will not be able to hit the 'OK' button	P	
NTC_3.2b	Unexpected input for defining final desired tube		Input a decimal number for row and column number (Example: '1.5')	User will not be able to hit the 'OK' button	P	
NTC_3.2c			Input a negative number for row and column number (Example: ' -1 ')	User will not be able to hit the 'OK' button	P	
NTC_4.0	Maximum time for each tube	Time in minutes	Enter a time greater than set maximum time (0-999 minutes)	User will not be able to hit the 'OK' button	P	
NTC_4.1	Minimum time for each tube	Time in minutes	Enter a time less than set maximum time (0-999 minutes)	User will not be able to hit the 'OK' button	P	
NTC_4.2a	Unexpected input for defining desired time		Input any character besides a number for desired time in each tube (Example: ' a ')	User will not be able to hit the 'OK' button	P	
NTC_4.2b			Input a decimal number for desired time in each tube (Example: '1.5 ')		P	
NTC_4.2c	Unexpected input for defining desired time		Input a negative number for desired time in each tube (Example: ' -1 ')	User will not be able to hit the 'OK' button	P	
NTC_5.0	Double clicking of Start Sampling button		<p>Click Start Sampling button on GUI screen</p> <p>Once system begins experiment, click Start Sampling button again</p>	The user is not able to double click the button since it will be grey and disabled after first click	P	

NTC_6.0	Maximum amount of tubes for Manual Injection		Input a row or column number greater than maximum amount of tube rack in Manual Row or Manual Column section (Example: ' 7 ')	User will not be able to hit the 'OK' button	P	
NTC_6.1	Minimum amount of tubes for Manual Injection		Input a row or column number less than zero in Manual Row or Manual Column section (Example: ' -1 ')	User will not be able to hit the 'OK' button	P	
NTC_6.2a	Unexpected input for Manual Injection		Input any character besides a number for Manual Row and Manual Column number (Example: ' a ')	User will not be able to hit the 'OK' button	P	
NTC_6.2b			Input a decimal number for Manual Row and Manual Column number (Example: ' 1.5 ')	User will not be able to hit the 'OK' button	P	
NTC_6.2c			Input a negative number for Manual Row and Manual Column number (Example: ' -1 ')	User will not be able to hit the 'OK' button	P	
NTC_6.3	Double clicking of Manual Injection	Manual Row and Manual Column number must be inputted	Once the Injection button has been clicked and the needle has lowered for injection, click the Injection button again	The user is not able to double click the button since it will be grey and disabled after first click	P	
NTC_6.4	Double clicking of Manual Extraction	Manual Row and Manual Column number must be inputted and Injection button must have been clicked	Once extraction button has been clicked and the needle has raised to upright position, click extraction button again	The user is not able to double click the button since it will be grey and disabled after first click	P	
NTC_7.0	Maximum amount of rows for User Defined Row		Input a row number greater than maximum amount of rows (Example: ' 7 ')	User will not be able to hit the 'OK' button	P	
NTC_7.1	Maximum time for User Defined Row	Time in minutes	Enter a time greater than set maximum time (0-999 minutes) in User Defined Row section	User will not be able to hit the 'OK' button	P	
NTC_7.2	Minimum time for User Defined Row	Time in minutes	Enter a time less than set maximum time (0-999 minutes) in User Defined Row section	User will not be able to hit the 'OK' button	P	
NTC_7.3a	Unexpected input for User Defined Row		Input any character besides a number for User Defined Entire Row (Example: ' a ')	User will not be able to hit the 'OK' button	P	

NTC_7.3b	Unexpected input for User Defined Row		Input a decimal number for User Defined Row Entire Row (Example: ' 1.5 ')	User will not be able to hit the 'OK' button	P	
NTC_7.3c	Unexpected input for User Defined Row		Input a negative number for User Defined Row Entire Row (Example: ' -1 ')	User will not be able to hit the 'OK' button	P	
NTC_7.3d		Time in minutes	Input any character besides a number for User Defined Row time (Example: ' a ')	User will not be able to hit the 'OK' button	P	
NTC_7.3e		Time in minutes	Input a decimal number for User Defined Row time (Example: ' 1.5 ')	User will not be able to hit the 'OK' button	P	
NTC_7.3f		Time in minutes	Input a negative number for User Defined Row time (Example: ' -1 ')	User will not be able to hit the 'OK' button	P	
NTC_8.0	Door open	Experiment must be ongoing	Door switch is opened	Switch becomes open and power is shut down temporarily Red and yellow light should be illuminated showing experiment has been interrupted	P	
NTC_8.1	Door close	Experiment must be ongoing	Close door to test tube rack	Recent experiment that had been interrupted should continue and complete remaining experiment	P	
NTC_8.2	Pausing of experiment	Experiment must be ongoing	Click 'PAUSE' button on GUI display screen	Red and yellow lights should be illuminating showing experiment has been paused	P	
NTC_8.3	Continue experiment	Experiment must be paused	Click 'Continue' button on GUI display screen	Previous experiment should be continued and complete remaining experiment	P	
NTC_8.4	Loss of power from loose connection/unplugging of power cable		Unplug power cable from power supply	The experiment will be interrupted until power is back	P	
NTC_8.5	Loss of power from switch on control box		Flip switch on control box to 'OFF' position	The experiment will be interrupted until power is back	P	
NTC_9.0	Termination	Experiment must have completed filling of final desired tube	View light indicating systems current mode	Red, yellow, and green light should be on indicating the system is ready for user's next command GUI shows 'STOPSAMP'	P	

Requested:

- Fluid Positive Test
- Initialization time out test

4/may/2016

Supervisor: Lesley James

Signature:

Co-Supervisor: Luc Rolland

Signature:



Manager: Shervin Ayazi

Signature:




Student: Shengqi Jian

Signature:



10.11. Supplementary Test Script and Test Results

		Supplementary Test for Customized Autosampler				
		Project Name/#				
		Project Manager				
		Testing Start Date				
		Testing End Date				
		Name of Tester(s)				
Test ID	Test Objective	Precondition/Data	Steps to Execute	Expected Results	Pass/Fail	Comments
ST_1.0	Turn on LED Screen	Power cord must be plugged in	Click the Power button below LED screen	Screen should power on	P	
ST_1.1	Open Labview GUI	Screen and controller must be connected to main computer	Double click Labview GUI program on LED screen and click execute	Labview GUI should open on main computer	P	
ST_1.2	Verify connection of controller	All connections should be made and power must be supplied	View Labview GUI display screen	Labview GUI screen should display 'CONNECT' meaning autosampler is fully connected	P	
ST_2.0	Fluid injected for desired time	Experiment for single row	Experiment set for single row (Ex. Row 1 Time 2).	In each test tube, the valve will only open for Tmax when the needles are fully injected. The rest of the time, valve will be closed. The fluid will stop flowing after the valve is closed.	P	
ST_2.1	Extraction	One test tube is finished. The end-effector is going to next.	ST_2.0 is ongoing.	Valve is closed. End-effector is extracted and no fluid leaks from point A to point B.	P	
ST_2.2	Valve open and close	Experiment is paused	ST_2.0 is ongoing. The pause button is pressed.	No matter what the valve status is, it should close when pause button is pressed. After valve closed, the fluid should stop flowing.	P	
ST_2.3	Valve open and close	Door is opened	ST_2.0 is ongoing. Door switch is opened.	No matter what the valve status is, it should close if door is opened. After valve closed, the fluid should stop flowing.	P	
ST_3.0	Fluid injected for manual mode	Experiment for an arbitrary test tube	Experiment set for an arbitrary test tube (Ex. Row 1 Column 3)	In the test tube, the valve will only open and fluid will only be injected for the Tmax. The rest of the time, valve will be closed and fluid stops flowing until manual extraction button is pressed.	P	
ST_3.1	Valve open and close	Experiment on going	ST_3.0 is ongoing.	Valve will only be opened when the needles are fully injected into test tube for Tmax. After that, it will be closed and fluid will stop flowing.	P	

Notice: 1. Tmax = 20 seconds to fill the 10mL test tube
 2. In this testing, the fluid will be pure water

ST_3.2	Valve open and close	Experiment is paused	ST_3.0 is ongoing. The pause button is pressed.	No matter what the valve status is, it should close when pause button is pressed. After valve closed, the fluid should stop flowing.	P	
ST_3.3	Valve open and close	Door is opened	ST_3.0 is ongoing. Door switch is opened.	No matter what the valve status is, it should close if door is opened. After valve closed, the fluid should stop flowing.	P	
ST_4.0	Initialization Block	Initialization on going.	inject a rigid block between proximity sensor and closing arm	Auto sampler will detect the abnormal blocking and break the experiment. Red light on to notice technician come and remove the block.	P	
ST_5.0	Termination	Experiment must have completed filling of final desired tube	View light indicating systems current mode	Red, yellow, and green light should be on. GUI shows 'STOPSAMP'	P	

Supervisor:

Lesley James

Signature:

Lesley James 18-May-2016

Co-Supervisor:

Luc Rolland

Signature:

Luc Rolland 24 May 2016

Manager:

Shervin Ayazi

Signature:

Shervin Ayazi 24 May 2016

Student:

Shengqi Jian

Signature:

Shengqi Jian 24-May-2016

Notice: 1. Tmax = 20 seconds to fill the 10mL test tube
2. In this testing, the fluid will be pure water

2 of 2